Научном већу Института за физику у Београду
Београд, 15. октобар 2018.

Предмет: Молба за покретање поступка за реизбор у звање виши научни сарадник

Молим Научно веће Института за физику да у складу са Правилником о поступку и начину вредновања и квантитавном исказивању научно-истраживачких резултата истраживача покрене поступак за мој реизбор у звање виши научни сарадник.

У прилогу достављам:

- Мишљење руководиоца пројекта са предлогом чланова комисије
- Биографске податке
- Преглед научне активности
- Елементе за квалитативну оцену научног доприноса
- Елементе за квантитативну оцену научног доприноса
- Списак објављених радова и њихове копије
- Податке о цитираности
- Фотокопију решења о претходном избору у звање
- Додатке - доказе о квалитативним елементима

С поштовањем

др Димитрије Степаненко
виши научни сарадник

Научном већу Института за физику у Београду

Београд, 15. октобар 2018. године

Предмет: Мишљење руководиоца пројекта за реизбор др Димитрија Степаненка у звање виши научни сарадник

Др Димитрије Степаненко је запослен на Институту за физику Београд и ангажован је на пројекту основних истраживања ОИ171032 "Физика наноструктурних материјала и јако корелисаних система" чији сам руководилац.

Пошто колега задовољава услове прописане Правилником о поступку и начину вредновања и квантитавном исказивању научно-истраживачких резултата истраживача, предлажем Научном већу Института за физику у Београду да покрене поступак за реизбор др Димитрија Степаненка у звање виши научни сарадник.

За састав комисије за реизбор др Димитрија Степаненка у звање виши научни срадник предлажем:

(1) др Зорана Дохчевић-Митровић, научни саветник, Институт за физику у Београду,
(2) др Антун Балаж, научни саветник, Институт за физику у Београду,
(3) др Жељко Шљиванчанин, научни саветник, Институт за нукларне науке Винча.

Београд, 15. октобар 2018.

др Зорана Дохчевић-Митровић
научни саветник

Биографски подаци кандидата

Димитрије Степаненко је рођен 13. 7. 1974. у Врању, где је завршио основну школу и Гимназију. Током школовања у основној и средњој школи учествовао је на такмичењима из физике и освојио бројне награде. Освојио је похвалу на међународном такмичењу “First step to Nobel Prize in Physics” који је организовала Академија наука Пољске. Освојио је прву награду на државном такмичењу из физике и био је изабран у тим за међународну физичку олимпијаду 1993. на коју национални тим није отишао.

Студирао је на Физичком факултету Универзитета у Београду, где је 1998. године дипломирао на смеру Теоријска и експериментална физика, са просечном оценом током студија 9.68. Током студија радио је у Истраживачкој станици Петница.

По дипломирању одлази на постдипломске студије на Универзитет у Бостону (Boston University) где је провео две године као стипендиста универзитета (Presidential University Graduate Fellowship). Од 2001. наставља постдипломске студије на Државном Универзитету Флориде (Florida State University). Докторат из теоријске физике кондензованог стања одбранио је 2005. године. Докторат је нострификован на Универзитету у Београду, решењем бр. 06-613-7554/4-11, 30. јануара 2012. Током постдипломских студија добио је Дирак-Хелманову награду за теоријску физику 2004. године. Током студија радио је као асистент у настави и извођењу рачунских и експерименталних вежби на додипломским студијама. Радио је и као асистент на постдипломском курсу квантне механике. Сарађивао је на истраживању у Националној лабораторији за јака магнетна поља (National High Magnetic Field Laboratory). Боравио је у истраживачким групама у ИБМ истраживачком центру (IBM T. J. Watson research Center) и на Универзитету Охаја (Ohio University).

После доктората ради на Универзитету у Базелу (Universitaet Basel), Швајцарска, у групама Гвида Буркарда и Даниела Лоса. Држао је одабрана предавања и рачунске вежбе на напредним курсевима физике кондензованог стања и физике многочестичних система и учествовао је у настави на уводним курсевима физике и примењене математике. Учествовао је у истраживањима на пројектима Швајцарске националне фондације (СНФ), Европске комисије на Марија Кири пројекту MagMaNet и ФП7 пројектима MolSpinQIP и ELFOS, као и у истраживањима у области квантне информације под покровитељством агенција DOE и IARPA Сједињених Америчких Држава. Поред истраживања, на пројектима MagMaNet, MolSpinQIP и ELFOS радио је и као организатор локалне групе конзорцијума на Универзитету у Базелу. Боравио је на Институту за нанонауке Универзитета Модена и Реџио Емилија у Модени као гостујући истраживач.

Од 2013. ради на Институту за физику у групи за нове материјале и нанонауке. Водио је пројекте билатералне сарадње са Немачком и Француском и SCOPES програм сарадње Швајцарске националне фондације. Национални је представник у европској мрежи за молекуларни магнетизам у оквиру COST акције MolSpin.

Тема научног рада кандидата је контрола спинова и наелектрисања у наноструктурама. Развио је принципе коришћења спин-орбитне интеракције за контролу спинова користећи електрична поља као класичне контролне величине у квантним тачкама и молекуларним магнетима. Ради на процесирању квантне информације у молекуларним магнетима, оптичким методама контроле нуклеарних спинова у полупроводничким наноструктурама, квантном транспорту шупљина и транспорту наелектрисања у зрнастим филмовима.

Преглед научне активности

Истраживања др Димитрија Степаненка се баве квантним својствима спинова у материјалима са наноструктуром и њиховом контролом помоћу класичних поља у сврху обраде квантне информације. Међу системима који могу послужити као основа за изградњу квантних рачунара, спинови су специфични по томе што су све њихове особине инхерентно квантне и описане коначним, обично малим, бројем степени слободе.

Слободни спинови електрона су, нажалост, лош избор за носиоце квантне инфирмације пошто је њима тешко манипулисати. Зато је квантна динамика јасно видљива и управљива само код електронских спинова урођених у веће структуре. Временска скала квантне контроле мора бити довољно кратка како декохеренција не би уништила квантне особине спинова. Просторна скала контроле мора бити довољно мала да би се манипулисали појединачни спинови. Ови захтеви говоре да су најбољи носиоци квантне информације системи димензија између једног и сто нанометара. На просторним и временским скалама карактеристичним за наносистеме, брзо променљива, јака и локална електрична поља је знатно лакше произвести него одговарајућа магнетна поља. Док су дужа времена кохеренције су повезана са мањим системима, једноставност контроле фаворизује веће. Зато свака архитектура квантног рачунара мора наћи равнотежу између ова два захтева.

Кандидатова истраживања разматрају електронске спинове у квантним тачкама са карактеристичним димензијама реда величине десет до сто нанометра, мултифероичним филмовима са зрнима величине једног до сто нанометара и молекуларним магнетима са карактеристичним димензијама од десетог дела нанометра до неколико нанометара. Теме истраживања су:

(1) контрола спинова у квантним тачкама са спин-орбитном интеракцијом
(2) ефективна интеракција спинова
(3) спин-електрична интеракција у молекуларним магнетима
(4) електричне особине материјала са мултифероичним зрнима
(5) транспорт у наноструктурама са спинском текстуром
(6) квантна мерења и контрола декохеренције

(1) Контрола спинова у квантним тачкама са спин-орбитном интеракцијом

Спин-орбитна интеракција изазива декохеренцију и тиме ствара озбиљан проблем у дизајну квантних рачунара базираних на спину електрона у једноелектронским квантним тачкама. Како су спински степени слободе знатно кохерентнији од орбиталних, спрезање смањује време кохеренције спина. Кандидат је показао да, и поред смањења времена кохеренције, спин-орбитна интеракција може бити ресурс за контролу спинова. Показао је да комбиновани ефекат временски зависне контроле и спин-орбитне интеракције производи корисна квантна логичка кола.

У периоду после претходног избора у звање виши научни сарадник, кандидат је развио процедуру за контролу спинова у квантним тачкама која користи временски зависну енергију стања у празној квантној тачки која интерагује тунеловањем са суседном квантном тачком у којој лежи спински кубит. Анализа временске зависности стања система открива неинтуитиван режим описан Ландау-Зенер прелазом. У овом режиму промена орбиталног стања везаног електрона је виртуелна, и сва промена је концентрисана на спинско стање. На основу овог прелаза конструисао је процедуру којом се спин контролише електричним пољем, без локалног мењања магнетног поља и без манипулације спин-орбитном

интеракцијом. Специфичност описаног поступка је могућност обављања прецизно дефинисане квантне операције без познавања јачине магнетног поља у квантним тачкама.

Тема контроле спинова коришћењем спин-орбитне интеракције је покренута у радовима кандидата који су урађени пре претходног избора у звање. У њима је показао да квантно логичко коло на спиновима у квантним тачкама под утицајем спин-орбитне интеракције зависи од облика временске зависности примењеног импулса. Кандидат је развио метод за смањење грешке у колу коришћењем временски симетричних импулса. Показао је да оваква контрола може произвести различита квантна логичка кола варирањем временске зависности симетричних импулса. Касније је показао да се овим импулсима могу применити сва кола из скупа универзалног за квантно рачунање над кубитима кодираним у парове спинова. Развио је поступак контроле за системе спинова у константном и хомогеном магнетном пољу и за системе спинова у временски константном али просторно јако нехомогеном магнетном пољу.

- *Coherent manipulation of single electron spins with Landau-Zener sweeps*
  M. Rančić and **D. Stepanenko**
  Phys. Rev. B **94**, 241301(R) (2016), M21
- *Exchange-based CNOT gates for singlet-triplet qubits with spin-orbit interaction*
  J. Klinovaja, **D. Stepanenko**, B. I. Halperin, and D. Loss
  Phys. Rev. B **86**, 085423 (2012), M21
- *Universal quantum computation through control of spin-orbit coupling*
  D. Stepanenko and N. E. Bonesteel, Physical Review Letters **93**, 140501 (2004)
- *Spin-orbit coupling and time-reversal symmetry in pulsed quantum gates*
  D. Stepanenko, N. E. Bonesteel, D. P. DiVincenzo, G. Burkard, and D. Loss
  Phys. Rev. B **68**, 115306 (2003), M21a
- *Anisotropic spin exchange in pulsed quantum gates*
  N. E. Bonesteel, **D. Stepanenko**, and D. P. DiVincenzo
  Phys. Rev. Lett. **87**, 207901 (2001), M21a

(2) Ефективна интеракција спинова

Квантни рачунари су засновани на системима са малим бројем дискретних квантних бројева. Природа коришћених квантних бројева зависи од имплементације и они не описују цео систем. Са друге стране, примена квантних логичких кола захтева хамилтонијан који је функција искључиво кубитних степени слободе. Поједностављење описа система преласком са стварних степени слободе на ефективни систем логичких кубита је користан први корак у дизајну квантних рачунара. Кандидат је развио ефективне описе за неколико типова кубита.

У периоду после претходног избора у звање виши научни сарадник, кандидат је развио ефективни хамилтонијан за троструку квантну тачку. Трострука квантна тачка је значајна као најмањи логички кубит који омогућавају универзални скуп квантних логичких кола контролисаних само изотропном интеракцијом спинова. Зато је битно пронаћи ефективну интеракцију која приказује ефекте спин-орбитног спрезања. Кандидат је израчунао и испитао особине ефективне спинске интеракције у трострукој квантној тачки произвољне геометрије. Показао је да интеракција спинова у пару тачака зависи и од особина треће. У ефективном моделу, пронашао је опсег у коме се параметри ефективне интеракцине могу контролисати.

Пре претходног избора у звање, кандидат је израчунао ефективни спински хамилтонијан двоструке квантне тачке са спин-орбитном интеракцијом у присуству нуклеарне хиперфине интеракције са језгрима и четвороструке квантне тачке која кодира два двоспинска кубита. Ефективни хамилтонијан двоструке тачке је искористио за предвиђање доприноса спин-орбитне и нуклеарне хиперфине интеракције у тунеловању између спинских стања.

Предвиђена зависност је недавно потврђена и искоришћена у експериментима у којима су измерене јачине ових интеракција. Користећи ефективни хамилтонијан четвороструке квантне тачке, кандидат је издвојио параметар који одређује моћ ефективне интеракције у примени двокубитних квантних логичких кола. Показао је да пронађени параметар зависи од особина материјала у коме су кодиране квантне тачке и од геометрије система.

- *Effective spin Hamiltonian of a gated triple quantum dot in the presence of spin-orbit* interaction
  M. Milivojević and **D. Stepanenko**
  J. Phys. Cond. Matter **29**, 405302 (2017), M22
- *Singlet-triplet splitting in double quantum dots due to spin-orbit and hyperfine interactions*
  D. Stepanenko, M. Rudner, B. I. Halperin, and D. Loss
  Physical Review B **85**, 075416 (2012), M21
- *Quantum gates between capacitively coupled double quantum dot two-spin qubits*
  D. Stepanenko and Guido Burkard
  Phys. Rev. B **75**, 085324 (2007), M21

(3) Спин-електрична интеракција у молекуларним магнетима

На малим просторним и временским скалама, карактеристичним за квантну контролу спинова, лакше је контролисати електрична него магнетна поља. Међутим спинови не интерагују директно са електричним пољима. Кандидат је истраживао могућности индиректне контроле спинова електричним пољима.

У периоду после претходног избора у звање, кандидат је предвидео суперрадијантни квантни фазни прелаз у систему молекуларних магнета са спин-електричном интеракцијом који интерагују са електромагнетним пољем микроталасног резонатора. Предвидео је фазни прелаз између нормалне фазе карактерисане празном шупљином и суперрадијантне фазе карактерисане шупљином са ненултим бројем фотона. Пронашао је да у суперрадијантној фази компоненте електричних диполних момената молекула које леже у равни магнетних центара показују јаке флуктуације. Прелаз је специфичан зато што се критична јачина интеракције електричног поља и спинова може променити применом спољног хомогеног магнетног поља. Зато би у принципу било могуће мењати фазу система спољним константним магнетним пољем.

Спин-електрична интеракција у молекуларним магнетима је откриће кандидата из периода пре претходног избора у звање. Интеракција је недавно измерена у електронској спинској резонанци молекуларних магнета. Кандидат је предвидео да ефекат може постојати у свим антиферомагнетним молекулима без симетрије на инверзију. Претходни резултати кандидата су класификација ових интеракција у молекуларним прстеновима и предвиђање последица интеракције по електромагнетни и топлотни одзив материјала. Кандидат је идентификовао композитне спинске степене слободе молекула који интерагују са електричним пољима. Показао је да су времена кохеренције узроковане интеракцијом са језгрима код ових степени слободе два до пет редова величине дужа од одговарајућих времена кохеренције појединачних спинова и пројекције укупног спина молекула.

- *Field-dependent superradiant quantum phase transition of molecular magnets in microwave* cavities
  D. Stepanenko, M. Trif, O. Tsyaplyatyev, and D. Loss
  Semicond. Sci. Technol. **31**, 094003 (2016), M22
- *Hyperfine-induced decoherence in triangular spin-cluster qubits*
  F. Troiani, **D. Stepanenko**, and D. Loss

Phys. Rev. B **86**, 161409(R) (2012), M21
- *Spin-electric effects in molecular antiferromagnets*
  M. Trif, F. Troiani, **D. Stepanenko**, and D. Loss
  Phys. Rev. B **82**, 045429 (2010), M21
- *Quantum computing with molecular magnets*
  D. Stepanenko, M. Trif, and D. Loss, M22
  Inorg. Chim. Acta **361**, 3740 (2008)
- *Spin-electric coupling in molecular magnets*
  M. Trif, F. Troiani, **D. Stepanenko**, and D. Loss
  Phys. Rev. Lett. **101**, 217201 (2008), M21a

(4) Електричне особине зрнастих мултифероичних материјала

Спин електрична интеракција која се може користити за обраду квантне информације није једини случај преплитања електричних и магнетних својстава материје. Многи мултифероици показују истовремено електрично и магнетно уређење.

У периоду после претходног избора у звање, кандидат је проучавао електрична својства филмова који се састоје од зрна бизмут ферита. Зрнаста структура доводи делове материјала у јако електрично поље које природно постоји на границама зрна и у околини дефеката. Кандидат је проучавао промене у електричним особинама филмова бизмут ферита на путу од унутрашњости зрна, која по структури личи на унутрашњост великих кристала, до границе зрна које на њу не личи. Пронађено је да површина између два суседна зрна и њена околина у дубини до неколико нанометра проводи наелектрисање знатно боље од унутршњости зрна. Механизам проводности у овој области не одговара ниједном од стандардних модела који описују полупроводнике или метале. Пронађено је и да се ова необична област близу границе шири у јаким електричним пољима. Хистерезисни одзив проводности у функцији напона мења природу између две области.

Поред напона на границама зрна, контрола кристалографске фазе може утицати на појаву јаких унутарњих електричних поља у материјалу и промене елктричних својстава. Кандидат је посматрао промене диелектричних особина допираних мултифероика са додавањем примеса холмијума. Пронађено је да допирање мења састав матријала по кристалографским фазама и њихов диелектрични и фероелектрични одзив. У јако допираним узорцима, фероелектрични одговор опстаје до јако високих поља и доводи до значајне електричне поларизације.

- *Dielectric and ferroelectric properties of Ho-doped BiFeO3 films across the structural phase transition*
  B. Stojadinović, Z. Dohčević-Mitrović, **D. Stepanenko**, M. Rosić, I. Petronijević, N. Tasić, N. Ilić, B. Matović, B. Stojanović
  Ceram. Int. **43**, 16531 (2017) , M21a
- *Variation of electric properties across the grain boundaries in BiFeO3 films*
  B. Stojadinović, B. Vasić, **D. Stepanenko**, N. Tadić, R. Gajić, and Z. Dohčević-Mitrović
  J. Phys. D **49**, 045309 (2016), M21

(5) Транспорт у наноструктурама са спинском текстуром

Електрични транспорт у наноструктурама на ниским температурама је одређен квантном интерференцијом путева кроз структуру. У случају носилаца наелектрисања са спиновима, детељи интерференције зависе и од спинских степени слободе. Контрола кретања

наелектрисања је основа електронике. Зависност транспорта наелектрисања од спина и спински транспорт су основе електронике засноване на спину - спинтронике.

У периоду пре претходног избора у звање, кандидат је проучавао интерференцију спинова у квантном транспорту. У III-V полупровидничким структурама, шупљине показују специфичан облик спин-орбитне интеракције, које је доминантно кубна по компонентама импулса, за разлику од стандардне линеарне интеракције електрона. Кандидат је показао како ова необична интеракција утиче на квантни транспорт. Резултате је генерализовао на општу дискусију Ахаронов-Бом ефекта у системима са спинским интеракцијама, уз ограничење спински независног расејања.

- *Current-conserving Aharonov-Bohm interferometry with arbitrary spin interactions*
  M. Lee and **D. Stepanenko**
  Phys. Rev. B **85**, 075316 (2012), M21
- *Interference of heavy holes in an Aharonov-Bohm ring*
  D. Stepanenko, M. Lee, G. Burkard, and D. Loss
  Phys. Rev. B **79**, 235301 (2009), M21

(6) Квантна мерења и контрола кохеренције

Квантна кохеренција је неопходан услов за функционисање квантног рачунара. Њена мера је време кохеренције, дефинисано као карактеристично време у коме стање кубита прећи из добро дефинисаног квантног стања у статистичку мешавину која не носи квантну информацију. Код кубита заснованих на спиновима у квантним тачкама кохеренција је ограничена спин-орбитном интеракцијом и хиперфином интеракцијом електронских и нуклеарних спинова.

У периоду пре претходног избора у звање, кандидат је развио поступак припреме неполарисаних стања језгара која су по утицају на губитак кохеренције спина еквивалентна поларизацијама реда 0.99. Припрема је заснована на ефекту електромагнетски индуковане транспарентности, мерењу емисије фотона и прилагођавању параметара експеримента у зависности од измерених времена емисије. У нумеричким симулацијама је показао да тако припремљена језгра изазивају спори губитак кохеренције.

- *Optical preparation of nuclear spins coupled to a localized electron spin*
  D. Stepanenko and G. Burkard
  Proc. 4th Symposium on Mesoscopic Superconductivity and Spintronics, 371 (2008), M33
- *Enhancement of electron spin coherence by optical preparation of nuclear spins*
  D. Stepanenko, G. Burkard, G. Giedke, and A. Imamoglu
  Phys. Rev. Lett. **96**, 136401 (2006), M21a

Елементи за квалитативну оцену научног доприноса

1 Квалитет научних резултата

1.1 Научни ниво и значај резлтата, утицај научних радова

Др Димитрије Степаненко је у свом досадашњем раду покренуо теме контроле спинова у квантним тачкама прилагођавањем временске зависности котролних параметара и спин-електричне интеракције у молекуларним магентима. Објавио је 18 радова у међународним часописима са ISI листе. Од тога 5 радова у часописима категорије М21а, 10 у часописима категорије М21 и 3 у часописима категорије М22. Поред радова у часописима, објавио је и једно саопштење са конференције штампано у целини које спада у категорију М33, 15 саопштења са скупова штампаних у изводу која спадају у категорију М34 и једно поглавље у монографији које спада у категорију М13.

У периоду после претходног избора у звање виши научни сарадник, кандидат је објавио један рад у часопису категорије М21а, два рада у часописима категорије М21, два рада у часописима категорије М22 и један прегледни рад у категорији М13.

Одржао је три предавања по позиву на научним скуповима.

Најзначајнији радови кандидата су:

1:
Coherent manipulation of single electron spins with Landau-Zener sweeps
Marko J. Rančić and Dimitrije Stepanenko
Phys. Rev. B **94**, 241301(R) (2016)
M21, цитиран 2 пута по Web of Science и по Google Scholar

2:
Singlet-triplet splitting in double quantum dots due to spin-orbit and hyperfine interactions
Dimitrije Stepanenko, Mark Rudner, Bertrand I. Halperin, and Daniel Loss
Phys. Rev. B **85**, 075416 (2012),
M21, цитиран 44 пута по Web of Science, 68 пута по Google Scholar

3:
Spin-Electric Coupling in Molecular Magnets
Mircea Trif, Filippo Troiani, Dimitrije Stepanenko, and Daniel Loss
Phys. Rev. Lett. **101**, 217201 (2008), M21a
M21a, цитиран 113 пута по Web of Science, 158 пута по Google Scholar

4:
Enhancement of Electron Spin Coherence by Optical Preparation of Nuclear Spins
Dimitrije Stepanenko, Guido Burkard, Geza Giedke, and Atac Imamoglu
Phys. Rev. Lett. **96**, 136401 (2006)
M21a, цитиран 111 пута по Web of Science, 169 пута по Google Scholar

5:
Universal Quantum Computation through Control of Spin-Orbit Coupling
D. Stepanenko and N. E. Bonesteel

Phys. Rev. Lett. **93**, 140501 (2004)
M21a, цитиран 55 пута по Web of Science, 78 пута по Google Scholar

Први рад представља нови облик контроле спинова помоћу временски зависних електричних поља. Кандидат је аутор идеје о контроли спинова помоћу временске зависности енергије електронских нивоа квантне тачке. Допринос кандидата укључује поставку проблема, аналитички третман прелаза у пару квантних тачака и интерпретацију нумеричких резултата. Истраживање је обављено у сарадњи са студентом постдипломских студија на Универзитету Констанц, у оквиру пројекта билатералне сарадње са Немачком. За разлику од ранијих метода који се ослањају на контролу облика напонских импулса којима се контролише електрично поље, нови облик контроле се заснива на Ландау-Зенер прелазу између својственог стања квантне тачке која носи спин и својственог стања суседне празне квантне тачке. Специфичност овог метода је да не захтева прецизно познавање параметара система за прецизну примену квантног логичког кола. Показано је да релативна неосетљивост прелаза на детаље система и спољног контролног поља чини прелаз неосетљивим на декохеренцију. Овим резултатом отворена је могућност контроле спинова у случајевима када технолошка ограничења спречавају фину контролу временске зависности контролних импулса.

У другом раду, представљен је метод којим се у укупној вероватноћи промене спина при тунеловању електрона између две квантне тачке могу раздвојити доприноси спин-орбитне и нуклеарне хиперфине интеракције. Резултати недавног експеримента потврђују облик израчунате зависности и мере однос интензитета спин-орбитне и нуклеарне хиперфине интеракције у двострукој квантној тачки. Рад је урађен у сарадњи са колегама са Универзитета у Базелу, Швајцарска и Универзитета Харвард, Сједињене Америчке Државе. Кандидат је поставио и нумерички решио модел које описује доприносе прелаза изазваних разматраним интеракцијама и њихову интерференцију. Са сарадницима је анализирао применљивост модела у различитим режимима параметара двоструке квантне тачке.

У трећем раду представљено је откриће интеракције спинова у молекуларним магнетима са електричним пољем. Кандидатов допринос се састоји од основне идеје да интеракција електричног поља са вишеспинским системима може постојати, раду са сарадницима на симетријској анализи, идентификацији спинских степени слободе значајних за интеракцију и дискусији модела заснованог на локализованим орбиталама. Ефекат је недавно потврђен у електронској спинској резонанци. На основу овог резултата и каснијих истраживања спин-електричне интеракције, покренути су пројекти MagMaNet, ELFOS, и MolSpinQIP. Кандидат наставља рад на овој теми у сарадњи са групом у CNRS Saclay, Република Француска и у оквиру COST акције CA15128-Molecular Spintronics.

У четвртом раду анализиран је стандардни експеримент квантне оптике, прозрачност индукована електромагнетним пољем, у прелазима између спинских стања и ексцитона у квантној тачки. Показано је да се мерењем тренутка емисије и прилагођавањем таласне дужине ласера у зависности од времена емисије нуклеарни спинови доводе у стање у коме слабо утичу на кохеренцију електронског спина у квантној тачки. Кандидатов допринос се састоји од постављања модела који описују мерење, његовог решавања и анализе временске зависности статистичког оператора нуклеарних спинова од резултата мерења. Овај метод је касније прилагођен на експерименте у којима се мери транспорт електрона кроз квантне тачке у режиму Кулонове блокаде.

Пети рад се баве контролом спинова у квантним тачкама коришћењем временски зависних електричних поља и спин-орбитне интеракције. Конструисан је универзални скуп квантних логичких кола за кубите кодиране у стања пара спинова на блиским квантним тачкама у

полупроводнику са спин-орбитном интеракцијом. Конструисани скуп не захтева променљива магнетна поља за примену и поједностављује конструкцију квантног рачунара базираног на спину. Кандидат је у дискусији са сарадницима поставио проблем, дефинисао простор доступних операција, конструисао логичка кола и анализирао зависност грешке кола од примењених импулса. Овај резултат је један од повода за каснију сарадњу са групом на Универзитету Констанц у Савезној Републици Немачкој на развоју квантне контроле.

1.2 Позитивна цитираност научних радова кандидата

Према ISI Web of Science бази, радови кандидата су цитирани 610 пута, 586 пута без самоцитата. Кандидатов h-индекс је 11. Према бази Google Scholar, радови кандидата су цитирани 897 пута са h-индексом 12.

1.3 Параметри квалитета часописа

Кандидат је објавио пет радова у часописима категорије М21а, и то четири у Physical Review Letters, и један у Ceramics International. У часописима категорије М21 објавио је 10 радова, од тога 9 у Physical Review B, и један у Journal of Physics D: Applied Physics. У часописима категорије М22 објавио је три рада, по један у Journal of Physics: Condensed Matter, Semiconductor Science and Technology и Inorganica Chimica Acta. Кандидат је аутор поглавља Molecular Magnets for Quantum Information Processing у монографији Molecular Magnets, Physics and Applications, Springer 2014, које је класификовано у категорију М13.

После претходног избора у звање објавио је један рад категорије М21а, два рада категорије М21 и два рада категорије М22.

Додатни библиометријски показатељи за период после претходног избора у звање:

	Импакт фактор	М	Снип
Укупно	14,16	36	5,14
Усредњено по чланку	2,83	7,20	1,03
Усредњено по аутору	4,53	10,19	1,53

1.4 Степен самосталности и степен учешћа у реализацији радова у научним центрима у земљи и иностранству

Кандидат је развијао идеје, те рачунске и нумеричке методе потребне за решавање проблема у дискусијама са сарадницима. Основне идеје за разматрање проводности прстенова и спин-електричне интеракције потичу од кандидата, док су за проблеме који се баве спиновима у квантним тачкама идеје резултат дискусија са сарадницима, тако да су заједничке, са значајним доприносом кандидата. У истраживању електричних особина мултифероичних филмова, кандидат је допринео теоријским увидом у процесе који се могу одигравати у испитиваним материјалима и указивањем на интересантне детаље, док је основна идеја потекла из круга осталих сарадника.

Сви теоријски резултати имају значајан допринос кандидата, док је нумерички део посла равномерно подељен међу свим сарадницима. Око једне трећине нумеричких израчунавања су резултати кандидата, док је остатак самостални допринос осталих сарадника. У раду на проблемима спин-електричног ефекта у молекулима, поред доприноса теоријском

разматрању и нумеричким израчунавањима, кандидат је организовао поделу рада међу сарадницима.

Кандидат сарађује са групама за теоријску физику кондензованог стања Универзитета у Базелу, Швајцарска, групом за квантну физику наносистема на Институту у Орсеју, Француска, групом за квантну спинтронику на Универзитету Констанц, Немачка, групом за молекуларни магнетизам на Националном центру за нанотехнологију у Модени, Италија, групом за неорганску хемију Универзитета у Валенсији, Шпанија и групом за физику квантне информације на Универзитету Цингхуа, Пекинг. Руководиоци ових група су Данијел Лос, Паскал Симон, Гвидо Буркард, Марко Афронте, Еугенио Коронадо и Мирча Триф.

1.5 Награде

- Presidential University Graduate Fellowship, Boston University. Стипендија за постдипломске студије на Уноверзитету у Бостону. Једна до две овакве награде се додељују студентима природних наука на овом универзитету.
- Dirac-Hellman award for theoretical physics. Једна награда се додељује студентима постдипломских студија или научним сарадницима на Државном Универзитету Флориде.

2 Ангажованост у формирању научних кадрова

Кандидат је ментор на мастер студијама Зорице Ристић, студенткиње Физичког факултета Универзитета у Београду. Мастер теза је одбрањена 28. 09. 2018., и студенткиња ће уписати докторске студије под менторством кандидата. Био је коментатор тезе др Симона Иерина, одбрањене на Универзитету Модене и регије Емилија у Италији. Кандидат је члан комисије која организује такмичење из физике ученика средњих школа. Сарађује са Истраживачком станицом Петница.

3 Нормирање броја коауторских радова, патената и техничких решења

Радови објављени после претходног избора у звање виши научни сарадник са темама о квантним тачкама и молекуларним магнетима су резултати до четири сарадника и садрже аналитичке и нумеричке резултате, те имају тежину 1. Радови о мултифероичним филмовима су претежно експериментални. Један од њих је приказ резултата 6 аутора, па улази са пуном тежином, 1, а други је резултат 9 аутора, па улази са тежином 0,71. Укупан ненормиран број бодова је 43,5, а нормиран 40,1, тако да је утицај нормирања мали.

4 Руковођење пројектима, потпројектима и пројектним задацима

Кандидат је руководио пројектима билатералне сарадње са Савезном Републиком Немачком (пројекат 3, 2014-15) и Републиком Француском (451-03-39/2016/09/16). Учествовао је у мрежи међународне сарадње у области молекуларне спинтронике у оквиру пројекта COST-MOLSPIN, где је заменик руководиоца радне групе за област квантне информације.

5 Активности у научним и научно-стручним друштвима

Кандидат је члан комисије за организовање такмичења из физике за ученике средњих школа. Рецензент је у часописима Nature, Nature Materials, npj Quantum Inforamtion, Nature Scientific Reports, Physical Review Letters, Physical Review B.

6 Утицајност научних резултата

Кандидатови резултати су стандардне референце за манипулацију спинова коришћењем ефекта спин-орбитне интеракције, за електричну контролу молекуларних магнета и за контролу стања нуклеарних спинова слабим квантним мерењима.

Кандидатови радови су, према бази ISI Web of Science, укупно цитирани 610 пута, од тога 586 пута не рачунајући аутоцитате, са h-индексом 11.

7 Конкретан допринос кандидата у реализацији радова у научним центрима у земљи и иностранству

Кандидат је зачетник две области у контроли спинова помоћу електричних поља. Развио је метод коришћења временске зависности електричних импулса као контролног механизма за спинове. Овај метод користи некомутирање ефективних спинских хамилтонијана узетих у различитим тренуцима током примене импулса. Метод је коришћен и за мерење интензитета интеракција које не очувавају спинове. Друга област је интеракција композитних спинских степени слободе у молекуларним магнетима са спољним електричним пољима. У овој области, резултати кандидата се користе у синтези молекуларних магнета за обраду квантне информације. Обе области развија у сарадњи са колегама у иностранству и у Србији.

8 Уводна предавања на конференцијама и друга предавања

У периоду после претходног избора у звање, кандидат је одржао два предавања по позиву на конференцијама:

- Spin-electric Coupling in Molecular Magnets, SFKM, Belgrade, Serbia, 2015. (M32)
- Квантни рачунари базирани на квантним тачкама и спин-орбит интеракцији, Дани физике кондензованог стања материје, САНУ, 10.-12. 09. 2013. (M62)

После претходног избора у звање, кандидат је одржао предавања о својим истраживањима у групама код којих је гостовао.

- Spin-electric coupling and coherence in triangular spin clusters, University of Konstanz, 24. 11. 2014.
- Spin structure and couplings in dimers of triangular molecules, University of Valencia, 11. 12. 2017.

Елементи за квантитативну оцену научног доприноса кандидата

Остварени бодови по категоријама у периоду после претходног избора у звање:

Категорија	М бодова по раду	Број радова	Укупно М бодова (нормирано)
М21а	10	1	10 (7,1)
М21	8	2	16
М22	5	2	10
М13	7	1	7
М32	1,5	1	1,5
М62	1	1	1

Поређење са минималним квантитативним условима за реизбор у звање виши научни сарадник:

Категорија	Минималан број М бодова	Остварено
Укупно	25	45,5 (42,6)
М10+М20+М31+М32+М33+М41+М42	20	44,5 (41,6)
М11+М12+М21+М22+М23+М24	15	36 (33,1)

Према ISI Web of Science бази, радови кандидата су цитирани 610 пута, 586 пута без аутоцитата. Према истој бази, h-фактор кандидата је 11.

Списак радова

Радови у међународним часописима изузетних вредности (M21a):

Рад објављен након претходног избора у звање:

- *Dielectric and ferroelectric properties of Ho-doped BiFeO3 nanopowders across the structural phase transition*
  Bojan Stojadinović, Zorana Dohčević-Mitrović, Dimitrije Stepanenko, Milena Rosić, Ivan Petronijević, Nikola Tasić, Nikola Ilić, Branko Matović, and Biljana Stojanović
  Ceram. Int. **43**, 16531 (2017)

Радови објављени пре претходног избора у звање:

- *Spin-electric coupling in molecular magnets*
  Mircea Trif, Filippo Troiani, Dimitrije Stepanenko, and Daniel Loss
  Phys. Rev. Lett. **101**, 217201 (2008)
- *Enhancement of electron spin coherence by optical preparation of nuclear spins*
  Dimitrije Stepanenko, Guido Burkard, Geza Giedke, and Atac Imamoglu
  Phys. Rev. Lett. **96**, 136401 (2006)
- *Universal quantum computation through control of spin-orbit coupling*,
  D. Stepanenko and N. E. Bonesteel
  Phys. Rev. Lett. **93**, 140501 (2004)
- *Anisotropic spin exchange in pulsed quantum gates*
  N. E. Bonesteel, D. Stepanenko, and D. P. DiVincenzo
  Phys. Rev. Lett. **87**, 207901 (2001)

Радови објављени у врхунским међународним часописима (M21):

Радови објављени после претходног избора у звање:

- *Coherent manipulation of single electron spins with Landau-Zener sweeps*
  Marko Rančić and Dimitrije Stepanenko
  Phys. Rev. B **94**, 241301(R) (2016)
- *Variation of electric properties across the grain boundaries in $BiFeO_3$ film*
  Bojan Stojadinović, Borislav Vasić, Dimitrije Stepanenko, Nenad Tadić, Radoš Gajić and Zorana Dohčević-Mitrović
  J. Phys. D Appl. Phys. **49**, 045309 (2016)

Радови објављени пре претходног избора у звање:

- *Hyperfine-induced decoherence in triangular spin-cluster qubits*
  Filippo Troiani, Dimitrije Stepanenko, and Daniel Loss
  Phys. Rev. B **86**, 161409(R) (2012)
- *Exchange-based CNOT gates for singlet-triplet qubits with spin-orbit interaction*
  Jelena Klinovaja, Dimitrije Stepanenko, Bertrand I. Halperin, and Daniel Loss:, Phys. Rev. B **86**, 085423 (2012)
- *Current-conserving Aharonov-Bohm interferometry with arbitrary spin interactions*,
  Minchul Lee and Dimitrije Stepanenko
  Phys. Rev. B **85**, 075316 (2012)
- *Singlet-triplet splitting in double quantum dots due to spin-orbit and hyperfine interactions*
  Dimitrije Stepanenko, Mark Rudner, Bertrand I. Halperin, and Daniel Loss

Phys. Rev. B **85**, 075416 (2012)

- *Spin-electric effects in molecular antiferromagnets*
  Mircea Trif, Filippo Troiani, Dimitrije Stepanenko, and Daniel Loss
  Phys. Rev. B **82**, 045429 (2010)
- *Interference of heavy holes in an Aharonov-Bohm ring*
  Dimitirje Stepanenko, Minchul Lee, Guido Burkard, and Daniel Loss
  Phys. Rev. B **79**, 235301 (2009)
- *Quantum gates between capacitively coupled double quantum dot two-spin qubits*,
  Dimitrije Stepanenko and Guido Burkard
  Phys. Rev. B **75**, 085324 (2007)
- *Spin-orbit coupling and time-reversal symmetry in pulsed quantum gates*
  D. Stepanenko, N. E. Bonesteel, D. P. DiVincenzo, G. Burkard, and Daniel Loss
  Phys. Rev. B **68**, 115306 (2003)

Радови објављени у истакнутим међународним часописима (М22):

Радови објављени након претходног избора у звање:

- *Effective spin Hamiltonian of a gated triple quantum dot in the presence of spin-orbit interaction*
  Marko Milivojević and Dimitrije Stepanenko
  J. Phys. Condens. Mat. **29**, 405302 (2017)
- *Field-dependent superradiant quantum phase transition of molecular magnets in microwave cavities*
  Dimitrije Stepanenko, Mircea Trif, Oleksandr Tsyaplyatyev, and Daniel Loss
  Semicon. Sci. Tech. **31**, 094003 (2016)

Рад објављен пре претходног избора у звање:

- *Quantum computing with molecular magnets*
  Dimitrije Stepanenko, Mircea Trif, and Daniel Loss
  Inorg. Chim. Acta **361**, 3740 (2008)

Поглавље у истакнутој монографији међународног значаја (М13):

- Molecular magnets for quantum information processing, in Molecular magnets, physics and applications, ISBN 978-3-642-40608-9, Springer, 2014.
  Kevin van Hoogdalem, Dimitrije Stepanenko, and Daniel Loss

Предавање по позиву са међународног скупа, штампано у изводу (М32):

- Spin-electric coupling in molecular magnets
  The 19th symposium on Condensed Matter Physics, Belgrade, Serbia, 2015.

Предавање по позиву са скупа националног значаја, штампано у изводу (М62):

- Квантни рачунари базирани на квантним тачкама и спин-орбит интеракцији
  Дани физике кондензованог стања материје, Српска академија наука и уметности, Београд, Србија, 2013.

Подаци о цитираности

Према ISI Web of Science, радови кандидата су цитирани 610 пута, 586 пута без аутоцитата, уз h-индекс 11.

Република Србија
**МИНИСТАРСТВО ПРОСВЕТЕ,
НАУКЕ И ТЕХНОЛОШКОГ РАЗВОЈА**
Комисија за стицање научних звања

Број:660-01-00194/254
29.01.2014. године
Б е о г р а д

На основу члана 22. става 2. члана 70. став 6. Закона о научноистраживачкој делатности ("Службени гласник Републике Србије", број 110/05 и 50/06 – исправка и 18/10), члана 2. става 1. и 2. тачке 1 – 4.(прилози) и члана 38. Правилника о поступку и начину вредновања и квантитативном исказивању научноистраживачких резултата истраживача ("Службени гласник Републике Србије", број 38/08) и захтева који је поднео

Институт за физику у Београду

Комисија за стицање научних звања на седници одржаној 29.01.2014. године, донела је

ОДЛУКУ
О СТИЦАЊУ НАУЧНОГ ЗВАЊА

Др Димитрије Степаненко
стиче научно звање
Виши научни сарадник

у области природно-математичких наука - физика

О Б Р А З Л О Ж Е Њ Е

Институт за физику у Београду

утврдио је предлог број 903/1 од 12.07.2013. године на седници научног већа Института и поднео захтев Комисији за стицање научних звања број 955/1 од 25.07.2013. године за доношење одлуке о испуњености услова за стицање научног звања ***Виши научни сарадник***.

Комисија за стицање научних звања је по претходно прибављеном позитивном мишљењу Матичног научног одбора за физику на седници одржаној 29.01.2014. године разматрала захтев и утврдила да именовани испуњава услове из члана 70. став 6. Закона о научноистраживачкој делатности ("Службени гласник Републике Србије", број 110/05 и 50/06 – исправка и 18/10), члана 2. става 1. и 2. тачке 1 – 4.(прилози) и члана 38. Правилника о поступку и начину вредновања и квантитативном исказивању научноистраживачких резултата истраживача ("Службени гласник Републике Србије", број 38/08) за стицање научног звања *Виши научни сарадник*, па је одлучила као у изреци ове одлуке.

Доношењем ове одлуке именовани стиче сва права која му на основу ње по закону припадају.

научни саветник

ПРЕДСЕДНИК
Проф. др Тривослав Јовановић

Citation report for 19 results from Web of Science Core Collection between 1996 and 2019 Go

You searched for: **From Marked List:** ...More

This report reflects citations to source items indexed within Web of Science Core Collection. Perform a Cited Reference Search to include citations to items not indexed within Web of Science Core Collection.

Export Data: Save to Excel File

Total Publications
19 Analyze

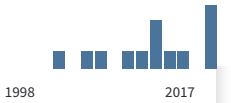

h-index
11

Average citations per item
32.11

Sum of Times Cited
610

Without self citations
586

Citing articles
494 Analyze

Without self citations
481 Analyze

Sum of Times Cited per Year

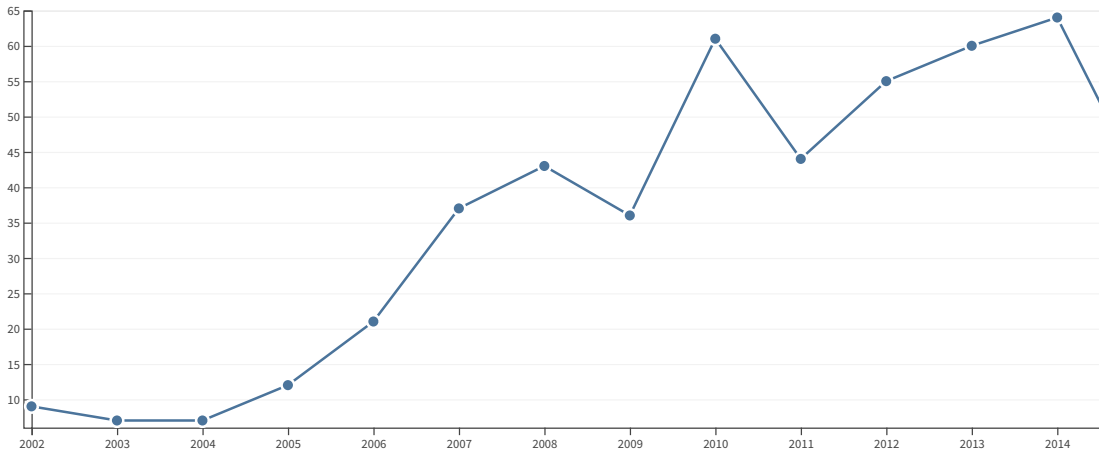

Sort by: Times Cited Date More

1 of 2

	2015	2016	2017	2018	2019	Total	Average Citations per Year
Use the checkboxes to remove individual items from this Citation Report							
	40	45	49	20	0	610	35.88

or restrict to items published between 1996 and 2019 Go

1.	**Spin-Electric Coupling in Molecular Magnets** By: Trif, Mircea; Troiani, Filippo; Stepanenko, Dimitrije; et al. PHYSICAL REVIEW LETTERS Volume: 101 Issue: 21 Article Number: 217201 Published NOV 21 2008	9	12	12	3	0	115	10.45
2.	**Enhancement of electron spin coherence by optical preparation of nuclear spins** By: Stepanenko, D; Burkard, G; Giedke, G; et al. PHYSICAL REVIEW LETTERS Volume: 96 Issue: 13 Article Number: 136401 Published APR 7 2006	5	6	6	0	0	111	8.54
3.	**Anisotropic spin exchange pulsed quantum gates** By: Bonesteel, NE; Stepanenko, D; DiVincenzo, DP PHYSICAL REVIEW LETTERS Volume: 87 Issue: 20 Article Number: 207901 Published NOV 12 2001	0	0	3	2	0	61	3.39
4.	**Universal quantum computation through control of spin-orbit coupling** By: Stepanenko, D; Bonesteel, NE PHYSICAL REVIEW LETTERS Volume: 93 Issue: 14 Article Number: 140501 Published OCT 1 2004	2	1	2	2	0	56	3.73
5.	**Spin-orbit coupling and time-reversal symmetry in quantum gates** By: Stepanenko, D; Bonesteel, NE; DiVincenzo, DP; et al. PHYSICAL REVIEW B Volume: 68 Issue: 11 Article Number: 115306 Published SEP 15 2003	0	2	3	2	0	52	3.25
6.	**Singlet-triplet splitting in double quantum dots due to spin-orbit and hyperfine interactions** By: Stepanenko, Dimitrije; Rudner, Mark; Halperin, Bertrand I.; et al. PHYSICAL REVIEW B Volume: 85 Issue: 7 Article Number: 075416 Published FEB 16 2012	6	6	10	3	0	46	6.57
7.	**Quantum gates between capacitively coupled double quantum dot two-spin qubits** By: Stepanenko, Dimitrije; Burkard, Guido PHYSICAL REVIEW B Volume: 75 Issue: 8 Article Number: 085324 Published FEB 2007	6	2	4	1	0	44	3.67
8.	**Spin-electric effects in molecular antiferromagnets** By: Trif, Mircea; Troiani, Filippo; Stepanenko, Dimitrije; et al. PHYSICAL REVIEW B Volume: 82 Issue: 4 Article Number: 045429 Published JUL 28 2010	1	6	3	2	0	39	4.33
9.	**Quantum computing with molecular magnets** By: Stepanenko, Dimitrije; Trif, Mircea; Loss, Daniel INORGANICA CHIMICA ACTA Volume: 361 Issue: 14-15 Pages: 3740-3745 Published OCT 1 2008	2	3	3	0	0	28	2.55
10.	**Exchange-based CNOT gates for singlet-triplet qubits with spin-orbit interaction** By: Klinovaja, Jelena; Stepanenko, Dimitrije; Halperin, Bertrand I.; et al. PHYSICAL REVIEW B Volume: 86 Issue: 8 Article Number: 085423 Published AUG 13 2012	6	2	2	1	0	24	3.43

Select Page | Save to Excel File

11.	**Hyperfine-induced decoherence in triangular spin-cluster qubits** By: Troiani, Filippo; Stepanenko, Dimitrije; Loss, Daniel PHYSICAL REVIEW B Volume: 86 Issue: 16 Article Number: 161409 Published OCT 17 2012	3	4	1	1	0	21	3.00
12.	**Interference of heavy holes in an Aharonov-Bohm ring** By: Stepanenko, Dimitrije; Lee, Mincheol; Burkard, Guido; et al. PHYSICAL REVIEW B Volume: 79 Issue: 23 Article Number: 235301 Published JUN 2009	0	0	0	0	0	9	0.90
13.	**Coherent manipulation of single electron spins with Landau-Zener sweeps** By: Rancic, Marko J.; Stepanenko, Dimitrije PHYSICAL REVIEW B Volume: 94 Issue: 24 Article Number: 241301 Published DEC 12 2016	0	0	0	2	0	2	0.67
14.	**Variation of electric properties across the grain boundaries in BiFeO3 film** By: Stojadinovic, Bojan; Vasic, Borislav; Stepanenko, Dimitrije; et al. JOURNAL OF PHYSICS D-APPLIED PHYSICS Volume: 49 Issue: 4 Article Number: 045309 Published FEB 3 2016	0	1	0	1	0	2	0.67
15.	**Dielectric and ferroelectric properties of Ho-doped BiFeO3 nanopowders across the structural phase transition** By: Stojadinovic, Bojan; Dobrevic-Mitrovic, Zorana; Stepanenko, Dimitrije; et al. CERAMICS INTERNATIONAL Volume: 43 Issue: 18 Pages: 16531-16538 Published DEC 15 2017	0	0	0	0	0	0	0.00
16.	**Effective spin Hamiltonian of a gated triple quantum dot in the presence of spin-orbit interaction** By: Milivojevic, Marko; Stepanenko, Dimitrije JOURNAL OF PHYSICS-CONDENSED MATTER Volume: 29 Issue: 40 Article Number: 405302 Published OCT 11 2017	0	0	0	0	0	0	0.00
17.	**Field-dependent superradiant quantum phase transition of molecular magnets in microwave cavities** By: Stepanenko, Dimitrije; Trif, Mircea; Tsyplyatyev, Oleksandr; et al. SEMICONDUCTOR SCIENCE AND TECHNOLOGY Volume: 31 Issue: 9 Article Number: 094003 Published SEP 2016	0	0	0	0	0	0	0.00
18.	**Current-conserving Aharonov-Bohm interferometry with arbitrary spin interactions** By: Lee, Mincheol; Stepanenko, Dimitrije PHYSICAL REVIEW B Volume: 85 Issue: 7 Article Number: 075316 Published FEB 21 2012	0	0	0	0	0	0	0.00
19.	**OPTICAL PREPARATION OF NUCLEAR SPINS COUPLED TO A LOCALIZED ELECTRON SPIN** By: Stepanenko, Dimitrije; Burkard, Guido Conference: 4th International Symposium on Mesoscopic Superconductivity and Spintronics Location: NTT, Atsugi, JAPAN Date: FEB 27-MAR 02, 2006 Sponsor(s): Japan Sci & Technol Agcy; NTT Basic Res Labs CONTROLLABLE QUANTUM STATES: MESOSCOPIC SUPERCONDUCTIVITY AND SPRINTRONICS Pages: 371-376 Published 2008	0	0	0	0	0	0	0.00

Select Page | Save to Excel File

PAPER

Effective spin Hamiltonian of a gated triple quantum dot in the presence of spin–orbit interaction

To cite this article: Marko Milivojevi and Dimitrije Stepanenko 2017 *J. Phys.: Condens. Matter* **29** 405302

IOP Publishing Journal of Physics: Condensed Matter
J. Phys.: Condens. Matter **29** (2017) 405302 (11pp) https://doi.org/10.1088/1361-648X/aa7f86

Effective spin Hamiltonian of a gated triple quantum dot in the presence of spin–orbit interaction

Marko Milivojević[1] **and Dimitrije Stepanenko**[2]

[1] Department of Physics, University of Belgrade, Studentski trg 12, 11158 Belgrade, Serbia
[2] Institute of Physics Belgrade, University of Belgrade, Pregrevica 118, 11080 Belgrade, Serbia

E-mail: milivojevic@rcub.bg.ac.rs

Received 7 June 2017, revised 12 July 2017
Accepted for publication 13 July 2017
Published 31 August 2017

Abstract

We derive and study the effective spin Hamiltonian of a gated triple quantum dot that includes the effects of spin–orbit interaction and an external magnetic field. In the analysis of the resulting spin interaction in linear and in general triangular geometry of the dots, we show that the pairwise spin interaction does depend on the position of the third dot. The spin–orbit induced anisotropy, in addition to changing its strength, also changes its symmetry with the motion of the third quantum dot outside the linear arrangement. Our results present a simplified model that may be used in the design of quantum computers based on three-spin qubits.

Keywords: spin–orbit coupling, quantum dots, exchange interactions

(Some figures may appear in colour only in the online journal)

1. Introduction

Spins of electrons confined to the single-electron quantum dots have been proposed as carriers of quantum information in solid-state quantum computers [1, 2]. They were the focus of intense theoretical and experimental investigation, leading to the understanding of the mechanisms of spin interactions with the surrounding semiconductor substrate through spin–orbit interaction and hyperfine coupling to the nuclei, as well as the interaction between the spins on neighboring quantum dots [3]. Spins in single-electron quantum dots coupled by the effective spin Hamiltonian are the basis for quantum computing schemes of ever simpler control and better coherence properties.

Encoding a qubit into states of few spins offers a trade-off between the number of used quantum dots and the complexity of required control mechanisms. With the original single-spin encoding [1], implementation of the quantum gates requires control of exchange interaction between the neighboring quantum dots, as well as of the rotations of individual spins about two, preferably orthogonal, axes. The requirement for two independent axes of rotation proved to be experimentally challenging. Encoding a qubit into states of a pair of spins reduces the control requirement to the exchange interaction and rotations about a single axis. A rather useful technique for electrically controlled qubit rotations is the electric-dipole-induced spin resonance [4–7]. In this implementation, spin–orbit interaction [8–11] and nuclear spins [12–15] are typical sources of anisotropy, but they are also the main sources of spin decoherence. The control requirements are reduced even further by encoding the qubits into states of three spins. With the isotropic spin exchange interaction as the only resource, quantum computation is possible in three spin qubits encoded into states of equal total spin and equal projection of this total spin to the quantization axis [16–20]. Sequences of few tens of interaction pulses that produce a set of quantum gates sufficient for quantum computation have been found both numerically [16] and analytically [17–20].

A recently developed scheme for quantum computation, based on three-spin resonant exchange qubits, uses periodic modulation of the exchange interaction between the quantum dots to implement quantum gates [21–23]. In this and other three-spin qubits the strongest interaction, isotropic exchange $J_{ij}\mathbf{S}_i \cdot \mathbf{S}_j$ between the spins within a qubit, does not mix the logical qubit states with other states of the three spins [24].

The scheme relies on the isotropic exchange form of interaction between the spins, and on the independence of the interaction between two spins on the third one. This requirements should be well satisfied when the spin–orbit interaction is weak and when the dots that are not involved in the current spin operation are well separated from the ones that are.

The quantum dots are described in terms of interaction between their spins. Therefore, developing a simple prediction of the effective spin Hamiltonian for electrons bound to quantum dots is useful for predicting the behavior of spins in experiments. In this work, we find the effective interaction between the spins in a triplet of quantum dots that can represent either a single three-spin qubit or a pair of spins involved in a quantum gate in the presence of a third spin [25]. The model that we use includes a potential of a triple dot, Coulomb repulsion between the electrons, an external magnetic field [26] and spin–orbit interaction. As opposed to earlier work [27–29], we derive the full triple dot effective Hamiltonian suitable for description of experiments on multiple spin qubits, and do not rely on the approximation of decoupled double dot, while taking the spin–orbit interaction into account. The calculations are done at the level of Hund–Mulliken approximation, including one orbital state per quantum dot, leading to the effective Hubbard model and the low-energy effective spin Hamiltonian. We quantify the deviations of these resulting interactions from the ideal case of pairwise isotropic interactions independent from the third dot outside the pair. Spin–orbit interaction, to the lowest order, is described by the pairwise Dzyaloshinsky–Moriya interaction between the spins. The presence of the third dot leads to small changes in the interaction strength and its anisotropy. With the exception of the linear arrangement of the dots, the symmetry axis of the effective spin interaction depends on the position of the third dot. The magnetic field adds a small three-body term, in agreement with the earlier results [27–29].

In section 2 we introduce the model of triple quantum dot. In section 3 we derive the effective spin Hamiltonian for various geometries. In section 4, we discuss the isotropic interaction, and find the influence of the position of the third dot on the pairwise spin interaction. In section 5, we discuss the anisotropy in spin interaction and its variations as the geometric arrangement of the dots goes from linear to triangular. We present our conclusions in section 6.

2. Model

We consider a system of three coupled quantum dots (QDs) with three conduction band electrons bound to them. The dots are modeled by a potential with the minima at the position of the dots. Electrons in the potential minima interact through Coulomb interaction, feel the influence of the substrate through spin–orbit interaction, and move in an external magnetic field. The system Hamiltonian is

$$H = H_0 + C + H_{\mathrm{SO}} + H_{\mathrm{Z}}, \tag{1}$$

$$H_0 = \sum_{i=a,b,c} h_i, \tag{2}$$

$$h_i = \frac{1}{2m}\left(\mathbf{p}_i + q\mathbf{A}(\mathbf{r}_i)\right)^2 + V(\mathbf{r}_i), \tag{3}$$

$$C = \sum_{i\neq j} \frac{1}{4\pi\epsilon_0\epsilon_r}\frac{e^2}{|\mathbf{r}_i - \mathbf{r}_j|}, \tag{4}$$

$$H_{\mathrm{SO}} = \sum_{i=a,b,c} H_{\mathrm{D},i} + H_{\mathrm{R},i}, \tag{5}$$

$$H_{\mathrm{Z}} = \sum_{i=a,b,c} g\mu_{\mathrm{B}}\mathbf{B}\cdot\mathbf{S}_i. \tag{6}$$

The single-particle noninteracting Hamiltonians h_i describe an electron in the quantum dots potential $V(\mathbf{r}_i)$, and in the magnetic field derived from the vector potential $\mathbf{A}(\mathbf{r})$. We model the potential that binds the electrons to the triple dot as

$$V(\mathbf{r}) = \sum_{i=a,b,c} \frac{m\omega_0^2}{2}\left(1 - \frac{h}{\lambda^2}\right)\left((\mathbf{r}-\mathbf{R}_i)^2 \mathrm{e}^{-\frac{m\omega_0^2}{2\lambda^2\hbar}(\mathbf{r}-\mathbf{R}_i)^2}\right) + \hbar\omega_0 h\left(1 - \mathrm{e}^{-\frac{m\omega_0^2}{2\lambda^2\hbar}(\mathbf{r}-\mathbf{R}_i)^2}\right). \tag{7}$$

This potential separates into three harmonic wells of frequency ω_0 near the minima at $\mathbf{r} = \mathbf{R}_i$, $i = a, b, c$. The effective Bohr radius of a single isolated harmonic potential at the position of a dot is $a_{\mathrm{B}} = \sqrt{\hbar/m\omega_0}$. We use $\hbar\omega_0 = 3$ meV [30], a typical value obtained in the experiments. The mass m is the conduction band electron effective mass, and for GaAs quantum dots it is $m = 0.067\ m_{\mathrm{e}}$, where m_{e} is the electron mass. The potential is parabolic in the vicinity of minima located at $\mathbf{R}_i$, and the parabolas are cut off by a Gaussian of width λa_{B}. The parameter h controls the depth of parabola. With parameter values $h = 3$ and $\lambda = 0.2$ the potential can host well localized and interacting spins.

Coulomb interaction of the electrons is described by C. We have used unscreened Coulomb potential with the effects of the host material described by the dielectric constant ϵ_r. For GaAs, $\epsilon_r = 13.1$.

Quantum dots are most often fabricated in two-dimensional electron gas (2DEG) within a III–V semiconductor. This typical host material for QDs shows both the Dresselhaus [31] and Rashba [32] SO interactions, and to a good approximation they are both linear in crystal momentum components. The form of SO coupling is constrained by the symmetry of the structure, and for GaAs 2DEG grown in $[0\,0\,1]$ crystallographic direction it can be written as

$$H_{\mathrm{SO}} = \boldsymbol{\Omega}(\mathbf{k})\cdot\mathbf{S}, \tag{8}$$

where

$$\boldsymbol{\Omega}(\mathbf{k}) = (-f_{\mathrm{D}}k_{[1\,0\,0]} + f_{\mathrm{R}}k_{[0\,1\,0]})\mathbf{e}_x + (-f_{\mathrm{R}}k_{[1\,0\,0]} + f_{\mathrm{D}}k_{[0\,1\,0]})\mathbf{e}_y, \tag{9}$$

and f_{R} and f_{D} are Rashba and Dresselhaus parameters, respectively. The values of the parameters are fixed by the substrate composition and the shape of the potential well of the 2DEG. Components of wave vectors in the crystallographic frame are expressed in our coordinate system as

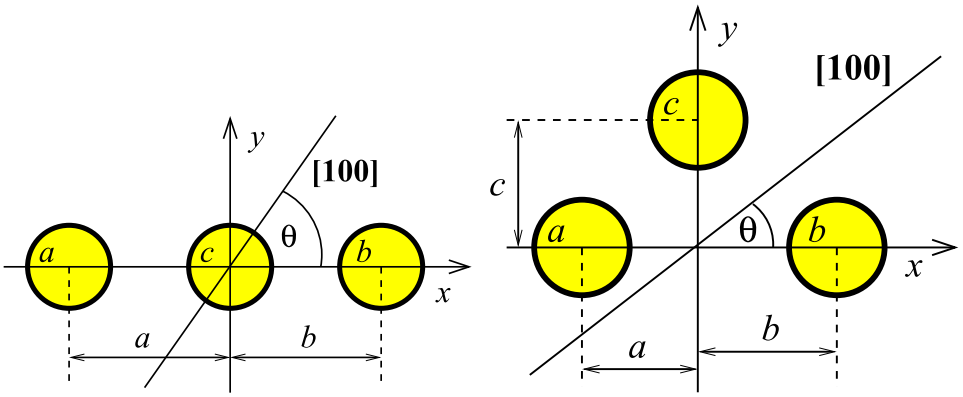

Figure 1. Geometry of the triple dot. Linear arrangement of the dots is shown in the left panel. Dots a, b and c lie on the x axis. Dot c is fixed at the origin, while the other two dots are allowed to move along the x axis. Triangular arrangement of the dots is illustrated on the right panel. Dots a and b are positioned on the x axis. The y coordinate of dot c can vary. In the magnetic field, we translate the coordinates so that the center of mass of the triple dot is at the origin. The orientation of the triple dot with respect to the crystalline axes of the substrate 2DEG in the $(0\,0\,1)$ plane of a III–V semiconductor is set by the angle θ between the x axis and the $[1\,0\,0]$ crystalline axis.

$k_{[1\,0\,0]} = \cos\theta k_x + \sin\theta k_y$ and $k_{[0\,1\,0]} = -\sin\theta k_x + \cos\theta k_y$. The geometry of the dots is described by the angle θ that the x axis makes with $[1\,0\,0]$ crystallographic direction, see figure 1.

Orbital effects of the magnetic field are due to the field component in the direction normal to the quantum dots. This field couples with electric charge through the vector potential $\mathbf{A} = \frac{B_z}{2}(-(y - Y_0), (x - X_0), 0)$, where $(X_0, Y_0, 0) = \mathbf{R}_0 = (\mathbf{R}_a + \mathbf{R}_b + \mathbf{R}_c)/3$ is the position of the center of three dots. This choice of gauge preserves the symmetry of triangular arrangements in the presence of magnetic fields. Zeeman term, H_Z, couples magnetic field and electron spins

$$H_Z = \sum_{i=a,b,c} g\mu_B \mathbf{B} \cdot \mathbf{S}_i, \tag{10}$$

where g is the g-factor ($g \approx -0.44$ for GaAs), and μ_B is the Bohr magneton. Zeeman splitting is much smaller than the relevant orbital energies $g\mu_B B_z/\hbar\omega_0 \sim 0.03$ for magnetic field of interest in this system. We can neglect the Zeeman splitting when we deal with orbital degrees of freedom and include it later in the effective Hamiltonian.

3. Effective Hamiltonian

Experiments and quantum computing schemes that involve qubits in single-electron QDs are described in terms of effective spin Hamiltonians in which each electron spin is assigned to one of the QDs in the device [15, 16, 19, 20, 33–35]. This picture is appropriate in the limit of well localized electronic orbitals with small overlaps. Orbital excitations beyond the ground state within the quantum dots are separated by an energy of the order $\hbar\omega_0$, and can be safely neglected in a typical quantum dot potential. At the second step, the doubly occupied states of the Hubbard model with a pair of electrons in total spin $S = 0$ state sharing an orbital state are also removed from the model. In this final model, the orbital state is completely defined by the dot in which the electron resides, and the only remaining degrees of freedom are spins. The effect of the virtual transitions to doubly occupied states are taken into account as an effective spin interaction. The electrons can be described by spins at the localized sites only if the Hubbard model states are localized to single dots.

An electron in the isolated QD is well described by the orbital ground state of a two-dimensional harmonic oscillator in external magnetic field. With the reduction of the dot size, the energy levels are split due to confinement. In the small dots and at low temperature, $k_B T \ll \hbar\omega_0$, the state of an electron in a quantum dot approaches the oscillator ground state in the presence of a magnetic field, i.e. the Fock–Darwin (FD) ground state [36]. Spin degrees of freedom give us two possible states which can be occupied by the electron in a FD state. That gives us 20 possible states of three electrons in three orbitals. We can divide these states in two groups according to their energies. The first group consist of eight states in which each QD is occupied by one electron, the second group is formed from 12 states where one QD is doubly occupied. We neglect the states in which all three electrons lie on a single dot, since their energy gap is larger by both the Coulomb repulsion U and an orbital excitation of the quantum dot.

Since the Coulomb repulsion between two electrons is much stronger when they occupy the same QD, the singly occupied state are low and the doubly occupied ones are high in energy. We are interested only in the eight-dimensional low-energy subspace of twenty-dimensional Hamiltonian H. These eight states encode the three-spin qubit.

The low- and high-energy space of the three-electron system are coupled by spin-independent terms of Coulomb repulsion and tunneling, as well as by the spin-dependent tunneling caused by the SO interaction. The effects of this coupling are seen as the effective interaction between the electrons in the low energy space. The states in the low-energy sector all have nominally the same orbital distribution with one spin-1/2 electron in each of the dots. Therefore, the effective low-energy Hamiltonian describes the interaction between localized spins. The Zeeman interaction does not affect the orbital states, and does not couple the low- and high-energy subspaces, so it appears in the effective Hamiltonian directly.

The Fock–Darwin ground state (FD) for harmonic confinement centered at the dot origin (x_0, y_0) is

$$\varphi(x,y) = \sqrt{\frac{m\omega}{\pi\hbar}} \mathrm{e}^{-\mathrm{i}\frac{eB_z}{2\hbar}(xy_0 - yx_0)} \mathrm{e}^{-\frac{m\omega}{2\hbar}\left((x-x_0)^2+(y-y_0)^2\right)}, \tag{11}$$

where $\omega = \sqrt{\omega_0^2 + \frac{1}{4}\omega_c^2}$, and the cyclotron frequency $\omega_c = \frac{eB_z}{m}$ measures the orbital's magnetic compression. In the case of linear arrangement, see figure 1, we set the origin at the position of dot c, while dots a and b move along the x axis. We parameterize the triangular arrangement by putting the dots a and b along the x axis, and the dot c on the y axis. The FD states in a, b and c are φ_a, φ_b and φ_c, respectively. In a zero magnetic field, these wave functions are real.

The FD states are non orthogonal. Their overlaps, $S_{ij} = \langle\varphi_i|\varphi_j\rangle$ $(i,j \in \{a,b,c\})$, behave as

$$|S_{ij}| \propto \exp\left(-\frac{|r_{ij}|^2}{(2a_B)^2}\right), \tag{12}$$

quickly decaying once the interdot distance exceeds $2a_B$, twice the effective single dot Bohr radius. The magnetic field in z-direction makes the overlaps complex. Explicit expressions for the overlaps are given in appendix.

The calculation of matrix elements of the three-electron Hamiltonian is simplified if the basis single-electron orbitals are orthogonal. If $\varphi = (\varphi_a, \varphi_b, \varphi_c)^T$ represents three FD states, then the transformation $\Phi = S^{-1/2}\varphi$ gives orthogonal Wannier states $\Phi = (\Phi_a, \Phi_b, \Phi_c)^T$. The resulting orthogonal basis is not unique. We have used the direct square root of the overlap matrix. Another common choice is the transformation that, in addition to producing an orthogonal basis, minimizes the spread of the resulting orbitals [37]. We choose the phases in Φ so that the states become real in the limit of vanishing magnetic field.

The Hamiltonian H, (1), acts in the space spanned by placing three electrons in the states $c^\dagger_{i,s}|0\rangle$, where the index $i = a,b,c$ counts the Wannier orbitals, and $s = \pm 1/2$ labels the spin. The matrix elements of single-particle part of H between FD states, $\langle \mathrm{FD1}|H_0 + H_{\mathrm{SO}}|\mathrm{FD2}\rangle$, and the matrix elements of Coulomb interaction between the pairs of FD states, $\langle \mathrm{FD1}, \mathrm{FD2}|C|\mathrm{FD3}, \mathrm{FD4}\rangle$ are calculated explicitly and presented in appendix. They are combined into matrix elements between the Wannier states. The effects of indistinguishability of the particles are accounted for by assigning the signs to the vacuum expectation value of the products of 8 creation and annihilation operators for spin-1/2 electrons in Wannier states when calculating the matrix elements of single particle operator $H_0 + H_{\mathrm{SO}}$, and to the products of ten operators in two-particle operator C.

Resulting Hamiltonian is the Hubbard model for three electrons in three orbitals centered at the dots positions. The effective spin Hamiltonian is found by calculating the matrix elements of the Hamiltonian H between the states of three spin-1/2 electrons in Wannier orbitals, and projecting the result to the low-energy space, using the Schrieffer–Wolff (SW) transformation up to the fourth order [38, 39]. This perturbative calculation is valid when the separation in energy between the singly- and doubly-occupied states, which is of the order of on-site repulsion U, is much larger than the matrix elements connecting the states, t. In our calculations $t/U < 0.25$.

The effective spin Hamiltonian of three localized spin-1/2 particles is

$$H = \sum_i H_i^{(1)}(\mathbf{S}_i) + \sum_{\langle i,j\rangle} H_{ij}^{(2)}(\mathbf{S}_i, \mathbf{S}_j) + H_{abc}^{(3)}(\mathbf{S}_a, \mathbf{S}_b, \mathbf{S}_c). \tag{13}$$

In the most general case, single-, two- and three-spin interactions ($H^{(1)}$, $H^{(2)}$, and $H^{(3)}$) appear in (13). The dominant terms, H_0 and C in the Hamiltonian (1) are spin-independent and the dominant spin interaction is two-electron isotropic exchange $H_{ex}(\mathbf{S}_i, \mathbf{S}_j) = J_{ij}\mathbf{S}_i \cdot \mathbf{S}_j$. The interactions are parameterized as

$$H_i^{(1)} = \mathbf{b}_i \cdot \mathbf{S}_i, \tag{14}$$

$$H_{ij}^{(2)} = J_{ij}\mathbf{S}_i \cdot \mathbf{S}_j + \mathbf{d}_{ij} \cdot (\mathbf{S}_i \times \mathbf{S}_j) + \mathbf{S}_i \cdot \Gamma_{ij} \cdot \mathbf{S}_j, \tag{15}$$

$$H_{abc}^{(3)} = \sum_{ijk} \gamma_{ijk} S_a^i S_b^j S_c^k, \tag{16}$$

where the isotropic exchange couplings J_{ij}, $i \neq j = a,b,c$ are scalars, effective magnetic fields $\mathbf{b}_i$, $i = a,b,c$, and antisymmetric anisotropies $\mathbf{d}_{ij}$, $i \neq j = a,b,c$ are vectors, symmetric anisotropies Γ_{ij}, $i \neq j = a,b,c$, are symmetric traceless rank-2 tensors, and γ_{ijk}, $i,j,k \in \{x,y,z\}$ are components of a direct product of three spin components that can combine into various rank-3 tensors. We will later use a scalar $\alpha = (1/6)\sum_{i,j,k} \varepsilon_{ijk}\gamma_{ijk}$ to parameterize the mixed product contribution to the three-spin interaction $H_\alpha^{(3)} = \alpha \mathbf{S}_a \cdot (\mathbf{S}_b \times \mathbf{S}_c)$.

Before we proceed, we expose our goals regarding the analysis of the effective spin Hamiltonian, since the coupled quantum dots system has already been exhaustively studied before. The simplest way to study this problem is to use tight-binding t-U model [27] for spin-independent terms, in which magnetic field is included through Peierls phases. The t-U model can not be used to study dependence of exchange parameters on the distance of the dots and/or the applied external magnetic field, which also affects the tunneling matrix elements. In a more detailed approach [26], magnetic field and distance dependence are incorporated in the parameters of Hubbard model. We expand on these results in two ways and focus on the case of three electrons in a triple dot that is relevant for quantum computing applications. We calculate the anisotropic exchange, parameterized by $\mathbf{d}_{ij}$, $i \neq j = a,b,c$ in the full triple-dot setup. In addition, we find that both this anisotropy and the dominant isotropic exchange parameterized by J_{ij}, $i \neq j = a,b,c$ depend on the full system geometry that includes the position of the third dot. These parameters are important in any implementation of a three-spin qubit. They quantify the deviations from the ideal case of pure isotropic exchange, and it is for this ideal form of interaction that the gate implementations were developed. Furthermore, even in the absence of accurate predictions of the intensity of resulting interactions, their symmetry may

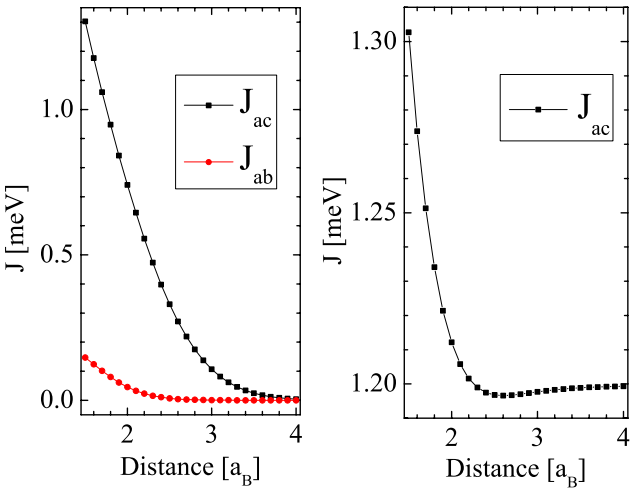

Figure 2. Exchange interaction in a linear triple quantum dot. In the left panel, exchange interaction parameters are plotted versus distance of the dots a and c in a symmetric arrangement. Dot c is fixed at the origin while the other two dots are able to move in such manner that $-a = b$. Dependence of the nearest neighbor interaction on the position of the third dot is illustrated in the right panel. For the linear arrangement of the dots with $a = -1.5a_B$ and $c = 0$, dependence of J_{ac} versus the distance of the dots bc (going from $1.5a_B$ to $4a_B$) is plotted. Parameters of the potential are $h = 3$ and $\lambda = 0.2$.

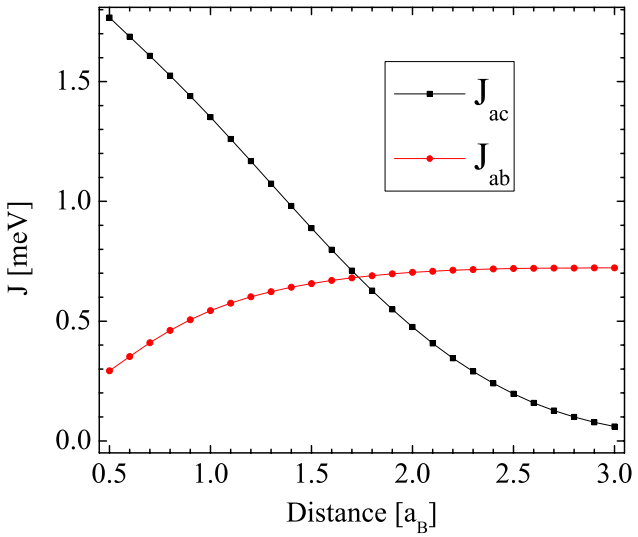

Figure 3. Exchange interaction parameters for the isosceles triangular arrangement. The plot shows the strength of exchange interaction as a function of deviation from the linear arrangement. Dot $a(b)$ is fixed at the $(-a_B, 0)((a_B, 0))$ and the c dot moves along the y axis from $0.5a_B$ to $3a_B$. In this case $J_{ac} = J_{bc}$, so only two different exchange parameters are plotted. When $c = \sqrt{3}a_B$, equilateral geometry is achieved with $J_{ac} = J_{bc} = J_{ab}$. Parameters of the potential are $h = 3$ and $\lambda = 0.2$.

provide valuable information in designing the time-dependent spin Hamiltonians that are not affected by this deviation from the ideal. Having these goals in mind, we proceed with the analysis of the effective spin Hamiltonian.

4. Isotropic interaction

The dominant terms in our model Hamiltonian are kinetic energy, confinement and Coulomb repulsion. All of these terms are spin-independent, so they cause an effective spin interaction invariant to spin rotation. Isotropic Hamiltonian with pairwise interaction can be written in the form

$$H_{\text{iso}} = J_{ab}\mathbf{S}_a \cdot \mathbf{S}_b + J_{ac}\mathbf{S}_a \cdot \mathbf{S}_c + J_{bc}\mathbf{S}_b \cdot \mathbf{S}_c, \qquad (17)$$

parameterized by the exchange interaction strengths J_{ab}, J_{ac}, and J_{bc}, as in (15). We analyze the dependence of these interactions on the geometry of the system. Raising (lowering) of the barrier height between the dots has the same effect as an increase (decrease) of the distance between them. This observation connects our results with experiments in control of the exchange strength. In the heart of the effective spin Hamiltonian approach is the requirement that orbitals of electrons are well localized at the centers of the quantum dots. Our results suggest that this condition is satisfied for $\ell > 1.5a_B$, and in this region $t/U < 0.23$. Exchange interactions in the linear arrangement, with equal nearest neighbor distances ($\ell_{ac} = \ell_{bc} = \ell$), are present in each pair of dots, as shown in figure 2. The distance dependence reveals the influence of third dot on two-spin interaction. In contrast to the standard approach in deriving the effective Hamiltonian using the Hubbard model of an isolated pair of dots, with only nearest neighbor interaction [40], our model also includes the matrix elements between the dots a and b, leading to a new term $J_{ab}\mathbf{S}_a \cdot \mathbf{S}_b$ in the Hamiltonian. This term is smaller, but comparable to J_{ac} for the $\ell < 2a_B$, see figure 2 (left). Since J_{ab} tends to zero much faster than J_{ac}, for $\ell > 2.5a_B$ it can be neglected.

In QD based quantum computing the control over spins is achieved through switching the pairwise exchange interactions on and off. It is assumed that while a gate is performed between the spins on neighboring QDs, all the other spins do not interact at all. In the effective Hamiltonian (17), H_{iso}, indirect coupling terms between the two dots are present due to the existence of the third dot. Second order contributions are smaller than the direct coupling, but observable.

Pairwise interaction between neighboring quantum dots depends on the position of the third one. In (figure 2 (right)), J_{ac} is plotted as a function of distance cb, while the distance ac is fixed at $1.5a_B$, explicitly showing the effect of the third dot. In the regime of totally decoupled third dot, exchange interaction for the double QD case is obtained. The variations of pairwise exchange coupling with the position of the third dot, show that the interaction J_{ac} can be controlled indirectly, by moving the dot b or by changing the barrier height between the dots c and b.

When the dots lie in a triangular arrangement, the relative strengths of isotropic exchange show a wider variety. We analyze these differences in an isosceles triangular arrangement (figure 3). The dots on x axis have the coordinates $(\pm a_B, 0)$, while y coordinate of the middle dot is moved along the y axis from $0.5a_B$ (t/U is then 0.17) to $3a_B$. Coupling is antiferromagnetic in this case, as in the case of double dot and in the linear arrangement of triple dot. Intensities of interactions $J_{ac} = J_{bc}$ decrease and tend to zero with the separation of the middle dot. On the other hand, J_{ab} has a slight increase due to

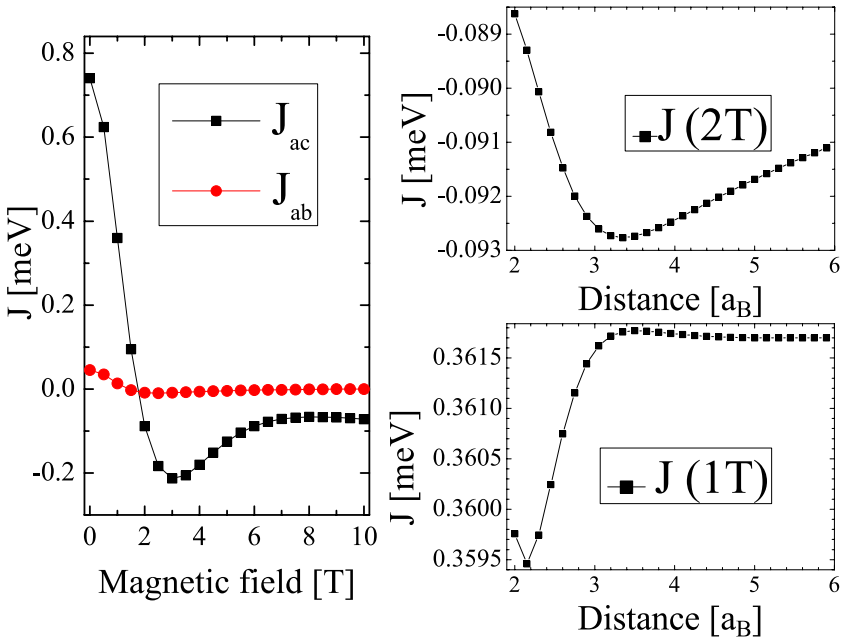

Figure 4. Exchange interaction in the magnetic field. In the linear arrangement of the dots with $ac = cb = 2a_B$, magnetic field alters the exchange interaction, and can even change its sign, as seen in the left panel. In the right panel, exchange parameter J_{ac} ($ac = 2a_B$) is plotted as function of the distance cb. The couplings are markedly different in external fields of 1 T and 2 T. Parameters of the potential are $h = 3$ and $\lambda = 0.2$.

the vanishing of negative hopping terms from a to b through c. Nonzero limit of J_{ab} and zero of J_{ac} suggest that we are in the regime of two dots decoupled from the third. For the equilateral arrangement ($c \approx 1.73a_B$), $J_{ab} = J_{ac}$, as expected. The main difference with respect to the linear setup is that all three dots can contribute to the full Hamiltonian. In the equilateral case, the symmetry requires that the eigenstates are fully delocalized across the three dots, and the eigenstates of three spins are correlated across the dots [41–43].

In the presence of magnetic fields, the orbitals of quantum dots shrink, and the overlaps become complex. In the linear arrangement, low-energy Hamiltonian has the same form as (17), but the intensities and the sign of these parameters are magnetic field dependent. In (figure 4 (left)), we illustrate the exchange coupling in a linear system with $ac = cb = 2a_B$ and the magnetic field strength going from 0 T to 10 T. In contrast to the nonmagnetic case, for magnetic field $1\ \mathrm{T} < B_z < 2\ \mathrm{T}$ we observe the transition from antiferromagnetic to ferromagnetic coupling constants due to the long-range Coulomb interaction. This transition was already observed in double quantum dots [44]. The antiferro-ferro transition can also be obtained by electrical means [45]. Magnetic field contributes to the FD states through the phase factor and magnetic squeezing, leading to a better localization of orbitals and weaker interaction. This is the reason for decline of isotropic exchange interaction strength, see (figure 4 (left)). In (figure 4 (right)) we illustrate the effect of the dot b on the exchange parameter J_{ac}. We start with the case where $ac = cb = 2a_B$, and move b so that cb goes from $2a_B$ to $6a_B$. Interactions in this setup depend on the magnetic field. In contrast to the case of linear geometry, the influence of dot b on J_{ac} is weak.

In the triangular arrangement, when magnetic field is introduced, a new term,

$$H_\alpha^{(3)} = \alpha \mathbf{S}_a(\mathbf{S}_b \times \mathbf{S}_c), \tag{18}$$

appears in the effective Hamiltonian [27–29]. This term depends on the flux enclosed by the three dots loop, and vanishes in the linear setup. Three-spin interaction in the Hubbard model is described by the three hopping matrix elements, making it weaker than the exchange interaction by an order of magnitude. In the triangles with large surface area, electrons show more delocalization across the dots in the low-energy states. In order to localize these electrons at the dots, and make their state more similar to perfectly localized spins of spin-based quantum dot qubits, the dot separation need to be larger than in the absence of magnetic field.

This condition further means that all the gate operations are much slower than in the linear setup since exchange parameters are weaker in this case. On the other hand, three-spin term can potentially be useful for preparation of the states with three-spin entanglement. The distance dependencies of the exchange parameters ($J_{ab} = J_{ac} = J_{bc} = J$) and the three-spin interaction in the equilateral geometry are illustrated in (figure 5). Spins are decoupled for magnetic fields stronger than 2 T. In weaker fields, $B_z < 2$ T the exchange interaction and the three-spin term grow to the values that can affect the quantum computation.

5. Anisotropic interaction

The spin–orbit interaction, described by H_{SO}, introduces anisotropy into the effective spin Hamiltonian. The strongest interaction is rotationally invariant and given in (17). The weak terms describing tunneling caused by SO interaction, $|\mathbf{\Omega}|/|t| \sim 0.1$ produce a second-order correction to the isotropic exchange parameters in the effective spin Hamiltonian.

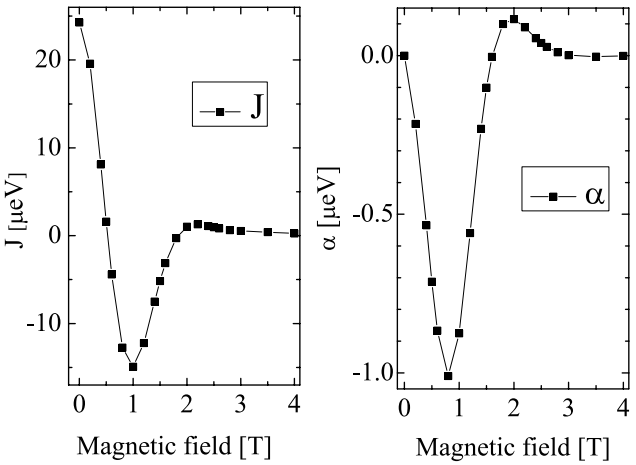

Figure 5. Exchange interaction parameter J and the three-spin term α for the equilateral triangular arrangement as a function of the magnetic field strength. Distance between the dots is $3.5a_B$. Parameters of the potential are $h = 3$ and $\lambda = 0.2$.

The dominant SO effect is the reduction of the symmetry of effective Hamiltonian, expressed as a sum of three antisymmetric Dzyaloshinsky–Moriya (DM) terms

$$H_{DM} = \mathbf{d}_{ab} \cdot (\mathbf{S}_a \times \mathbf{S}_b) + \mathbf{d}_{ac} \cdot (\mathbf{S}_a \times \mathbf{S}_c) + \mathbf{d}_{bc} \cdot (\mathbf{S}_b \times \mathbf{S}_c), \tag{19}$$

where the z components of all three $\mathbf{d}$ vectors are equal to zero. Higher-order contributions of SO interaction give the Γ-terms of $H^{(2)}$ in (15), which are another factor $|\mathbf{\Omega}|/t$ weaker than H_{DM}. We analyze only the DM terms, being the dominant correction to the isotropic interaction. Vectors $\mathbf{d}$ originate from the orbital Hamiltonian written in a scalar product form (8). On hopping between the dots, these terms flips the component of spin $\mathbf{S}$ along the quantization axis, with or without an additional phase. The hopping amplitude and the direction of spin after hopping depend on $\mathbf{\Omega}(\boldsymbol{k})$. Matrix elements $\boldsymbol{\beta}_{ij} = \langle\varphi_i|\mathbf{\Omega}(\boldsymbol{k})|\varphi_j\rangle$ of $\mathbf{\Omega}(\boldsymbol{k})$ between FD states are calculated in appendix. Parameters $\boldsymbol{\beta}_{ij}$ depend on the geometry of the system (parameters a, b and c), overlap integrals S_{ij} between the FD states φ_i and φ_j, Rashba and Dresselhaus parameters f_{R} and f_{D}, as well as on the orientation of the triple dot with respect to the crystallographic axes, as described by θ. If we scale every $\boldsymbol{\beta}$ vector by the appropriate overlap integral, we obtain a simple relation

$$\frac{\boldsymbol{\beta}_{ab}}{S_{ab}} + \frac{\boldsymbol{\beta}_{bc}}{S_{bc}} + \frac{\boldsymbol{\beta}_{ca}}{S_{ca}} = 0. \tag{20}$$

Additionally, the components of these vectors are constrained by the geometry of triple dot to satisfy relations

$$\frac{\boldsymbol{\beta}^y_{ab}}{\boldsymbol{\beta}^x_{ab}} = \frac{f_{\mathrm{R}}\cos\theta + f_{\mathrm{D}}\sin\theta}{f_{\mathrm{D}}\cos\theta + f_{\mathrm{R}}\sin\theta}, \tag{21}$$

$$\frac{\boldsymbol{\beta}^y_{\ell c}}{\boldsymbol{\beta}^x_{\ell c}} = \frac{(\ell f_{\mathrm{R}} + c f_{\mathrm{D}})\cos\theta + (-c f_{\mathrm{R}} + \ell f_{\mathrm{D}})\sin\theta}{(c f_{\mathrm{R}} + \ell f_{\mathrm{D}})\cos\theta + (\ell f_{\mathrm{R}} - c f_{\mathrm{D}})\sin\theta}, \tag{22}$$

where $\ell \in \{a, b\}$. Since every FD state centered at the observed point is the largest contributor to the Wannier state in the same dot, we expect that the relation between the components of $\boldsymbol{\beta}$ parameters in (21) is paralleled by the same relation between the components of $\mathbf{d}$ parameters scaled by the isotropic exchange interaction strengths J. We investigate this relation and find the $\mathbf{d}$ vectors as a function of the system's geometry, SO parameters f_{R}, f_{D} and the orientation of the system with respect to the crystallographic axes, θ.

In the linear arrangement, the triple dot is an extension of the double quantum dot, and some of the properties of the double quantum dot [10], also hold true in this case. For example, when $f_{\mathrm{D}} = f_{\mathrm{R}}$ and $\theta = \frac{3\pi}{4}$, SO effects are equal to zero. The ratio d^y_{ij}/d^x_{ij} is independent of the dots positions,

$$\frac{d^y_{ij}}{d^x_{ij}} = \frac{f_{\mathrm{R}}\cos\theta + f_{\mathrm{D}}\sin\theta}{f_{\mathrm{D}}\cos\theta + f_{\mathrm{R}}\sin\theta}, \tag{23}$$

for every pair of dots. Our numerical analysis is performed for the Rashba and Dresselhaus parameters equal to $f_{\mathrm{R}} = 5$ meVÅ and $f_{\mathrm{D}} = 16.25$ meVÅ [46], respectively, and the angles $\theta = 0$ and $\pi/4$. For $\theta = 0$, ratio was $\frac{d^y}{d^x} = \frac{f_{\mathrm{R}}}{f_{\mathrm{D}}}$. For $\theta = \frac{\pi}{4}$, x and y component were equal, suggesting that SO vectors are along the crystallographic axis, independent on the f_{R} and f_{D}. The intensities of SO vectors for the cases discussed above are plotted as functions of the nearest neighbor distance in (figure 6 (left)). The condition analogous to (20), with $\boldsymbol{\beta}$ vectors replaced by $\mathbf{d}$ vectors is never satisfied in the linear setup.

In three-spin qubits, anisotropy is an important source of deviations from the ideal behavior. We analyze the effect of the third dot on DM vector between the other two dots. In (figure 6 (right)) we show this effect for spin–orbit angles 0 and $\pi/4$ and Rashba and Dresselhaus parameters, $f_{\mathrm{R}} = 5$ meV Å and $f_{\mathrm{D}} = 16.25$ meV Å, respectively. The direction of DM vector does not change, but its intensity does. Orientation of the dots within the plane, described by θ, does not change the nature of this dependence, but only the intensities of $\mathbf{d}_{ij}$.

Spin–orbit coupling always influences spins in the triangular arrangement, due to the fact that all three $\boldsymbol{\beta}$ vectors cannot be zero at the same time. The vector $\boldsymbol{\beta}_{ab}$ is zero when $f_{\mathrm{R}} = f_{\mathrm{D}}$ and $\theta = 3\pi/4$, while $\boldsymbol{\beta}_{ac}$ vanishes when $f_{\mathrm{R}} = f_{\mathrm{D}}$ and $\tan\theta = \frac{c+a}{c-a}$. Condition $\boldsymbol{\beta}_{bc} = 0$ yields $f_{\mathrm{R}} = f_{\mathrm{D}}$ and $\tan\theta = \frac{c+b}{c-b}$. These requirements are compatible only when $c = 0$, i.e. with the dots in linear arrangement.

Apart from the fact that SO effects cannot be neglected, in this setup the directions of antisymmetric anisotropies $\mathbf{d}$ can vary. To illustrate this feature, we analyze the isosceles right triangle geometry (figure 7) for different orientations of the triple dot with respect to crystalline axes ($\theta = 0$ and $\theta = \frac{\pi}{4}$). In this geometry, every dot is at the same distance from the origin, $-a = b = c$ and the values of f_{R} and f_{D} are unchanged from their values in the previously considered case of aligned dots. Using the relation (21) for this geometry we find

$$\frac{\beta^y_{ab}}{\beta^x_{ab}} = \frac{f_{\mathrm{R}}}{f_{\mathrm{D}}}, \quad \frac{\beta^y_{ac}}{\beta^x_{ac}} = 1, \quad \frac{\beta^y_{bc}}{\beta^x_{bc}} = -1 \quad (\theta = 0), \tag{24}$$

$$\frac{\beta^y_{ab}}{\beta^x_{ab}} = 1, \quad \frac{\beta^y_{ac}}{\beta^x_{ac}} = \frac{f_{\mathrm{D}}}{f_{\mathrm{R}}}, \quad \frac{\beta^y_{bc}}{\beta^x_{bc}} = \frac{f_{\mathrm{R}}}{f_{\mathrm{D}}} \quad (\theta = \frac{\pi}{4}). \tag{25}$$

Our numerical results suggest that the analogous ratios of the components of $\mathbf{d}$ vectors are reached when the dots are more

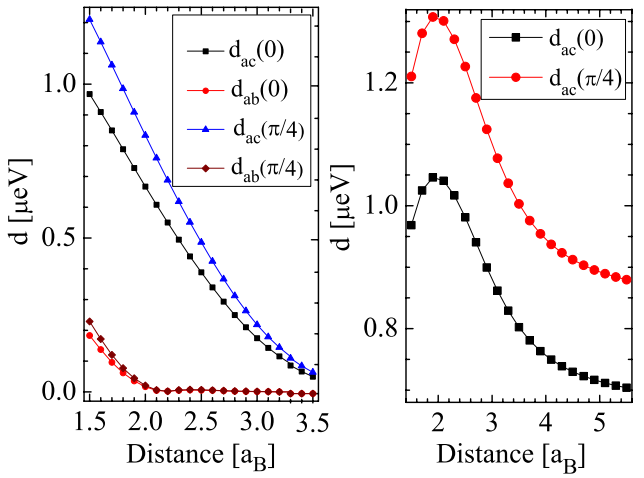

Figure 6. Dependence of anisotropy in two-spin interaction on geometry and on the orientation of linear triple quantum dot. (left) Intensity of SO parameters for the linear triple quantum dot in the cases of SO angles 0 and $\pi/4$. Dot c is fixed at the origin. Distances ac and bc are equal and vary from $1.5a_B$ to $3.5a_B$. (right) Dependence of the DM vector $\mathbf{d}_{ac}$ on the position of the dot b for SO angles 0 and $\pi/4$. Distance ac is fixed at $1.5a_B$, while distance cb varies from $1.5a_B$ to $5.5a_B$. Potential parameters are $h = 3$ and $\lambda = 0.2$. Rashba coefficient is $f_R = 5$ meV Å and Dresselhaus $f_D = 16.25$ meV Å.

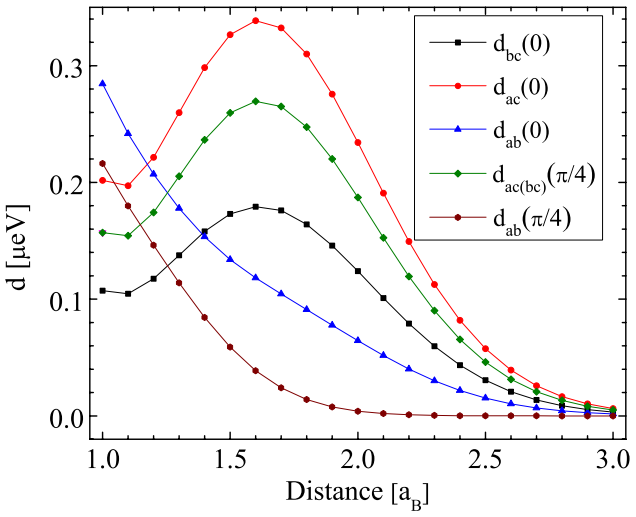

Figure 7. Intensity of SO parameters for the isosceles triple quantum dot for SO angles 0 and $\pi/4$ versus distance of each dot from the origin ($-a = b = c$). Potential parameters are $h = 3$ and $\lambda = 0.2$. Rashba coefficient is $f_R = 5$ meV Å and Dresselhaus $f_D = 16.25$ meV Å.

than $2a_B$ apart from each other. The relation analogous to (20) is never satisfied.

Equilateral arrangement is the only setup in which equation analogous to (20) is satisfied. Due to the fact that $S_{ab} = S_{ac} = S_{bc}$, we can write it as $\boldsymbol{\beta}_{ab} + \boldsymbol{\beta}_{bc} + \boldsymbol{\beta}_{ca} = 0$. We have numerically checked that condition $\mathbf{d}_{ab} + \mathbf{d}_{bc} + \mathbf{d}_{ca} \approx 0$ holds to numerical accuracy. While this symmetry seems promising for reducing the effects of anisotropy in spin interaction on the operation of the three-spin qubit, it is always associated with the simultaneous isotropic exchange interaction of all three spins, $J_{ab} = J_{bc} = J_{ca}$. Since this interaction conserves all the quantum numbers of encoded three spin qubits, it does not produce any quantum gate.

The magnetic field normal to the plane of triple dot adds to the anisotropy of effective spin interaction, in addition to squeezing of the orbitals and introduction of phases to the overlaps. The Dzyaloshinsky–Moriya vectors are magnetic field dependent since spin–orbit Hamiltonian depends on the momentum, acquiring the term $q\mathbf{A}$ in the magnetic field. We analyze the magnetic field dependence of anisotropy in the linear geometry of a triple dot. In contrast to the zero-field case, where $\boldsymbol{\beta}$ vectors were purely imaginary and ratio of their components was real number, in a magnetic field $\boldsymbol{\beta}$ has both real and imaginary component, so the connection with $\mathbf{d}$ is less straightforward. Our numerical analysis shows that the ratios of antisymmetric anisotropy components are dependent on the magnetic field strength and the position of the third dot. In (figure 8 (left)) we plot the dependence of intensity of antisymmetric anisotropy vectors on magnetic field strength for distance $ac = cb = 2a_B$ between the dots. Intensity reaches a minimum for the fields around 1 T. In stronger fields, the intensity grows until $B_z = 3$ T, and then declines towards zero. Dependence of antisymmetric anisotropy on the position of the third dot is studied and presented in (figure 8 (right)) for magnetic fields of 2 T and 1 T.

For the triangular arrangement we were unable to make a parameterization of the dominant SO effects in terms of DM vectors. We believe that single-orbital model cannot describe the accumulated phase factor (different from 1) due to the magnetic field and SO field in the closed loop geometry. There is a way to overcome this problem by using a spin and position dependent transformation [47, 48] which is able to gauge away the linear SO terms. This was done in the case of double QD [49], in which SO effects needed to be studied in terms of eigenenergies due to the basis transformation. Since our study is done using the fixed basis and DM parameters, it is beyond the scope of this work.

The dependence of effective interaction between a pair of spins in a triple quantum dot on the position of the third one is a potential tool for experimental realization of quantum gates. In experiments on multiple dots, the gate is applied by time-dependent voltages on electrostatic gates that modify the confinement potential. As the quantum dots position coincides with the local minima of confinement potential, and the potential is locally parabolic, the small variations of gate voltages are equivalent to the motion of the dots. Therefore, a solution of time-dependent Schrödinger equation for our Hamiltonian with time dependent dot coordinates models the spin evolution driven by a time-dependent voltage.

As the spin–orbit interaction is seen as a nuisance in exchange-only quantum computing schemes, we wish to find if there is a way to remove the linear SO effects in triple QDs. It has been shown [8] that, by the proper local rotation of one spin, a double QD Hamiltonian, up to the linear SO contribution, can be written as $J(R^{\theta}_{\mathbf{u}}(\mathbf{S}_a)) \cdot \mathbf{S}_b$, where $R^{\theta}_{\mathbf{u}}$ represents a rotational matrix for an angle $\theta = |\mathbf{d}|/J$ around an axis $\mathbf{u} = (d_x, d_y, 0)/\theta J$. There is a simple prescription for removing DM terms in a linear array of QDs. Since in

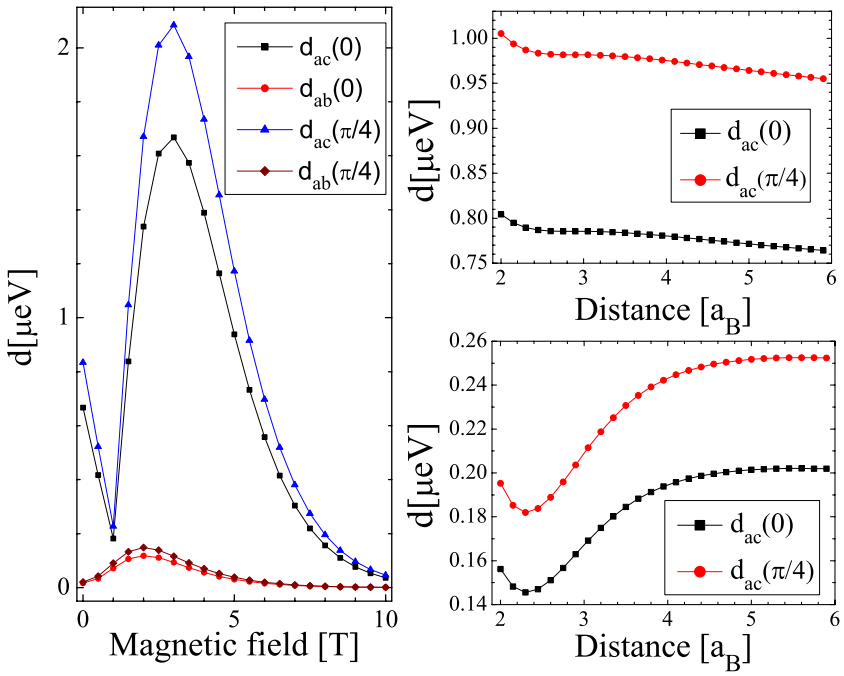

Figure 8. Dependence of two-spin interaction anisotropy on magnetic field and the position of third dot. (left) Intensity of SO parameters for the linear arrangement in the presence of perpendicular magnetic field. The geometry is set by $a(b) = -(+)2a_B$, $c = 0$. SO angles are 0 and $\pi/4$. (right) Intensity of SO parameter d_{ac} for the fixed distance $ac = 2a_B$ and magnetic field strengths 2 T (upper right) and 1 T (lower right) with respect to the distance cb going from $2a_B$ to $6a_B$. SO angles are 0 and $\pi/4$. Potential parameters are $h = 3$ and $\lambda = 0.2$. Rashba coefficient is $f_R = 5$ meV Å and Dresselhaus $f_D = 16.25$ meV Å .

that case nearest neighbor exchange is the dominant energy scale and the most quantum computation schemes use only this interaction [16, 18], it is enough to rotate two nearest neighbor spins in the same fashion as above. On the other hand, in triangular triple quantum dots, there is an additional freedom in the choice of time dependent interaction that implements a quantum gate. A different time-dependent Hamiltonian can be applied to each pair of spins, since now there is no clear distinction between nearest neighbor and next-nearest neighbor exchange. The question remains whether we can remove all three DM terms. We have a freedom of choice to rotate two spins in order to get rid of two DM terms: for instance, we are going to rotate spins $\mathbf{S}_b$ and $\mathbf{S}_c$ by the angles $\theta_{ab} = |\mathbf{d}_{ab}|/J_{ab}$ and $\theta_{bc} = |\mathbf{d}_{bc}|/J_{bc}$ around the vectors $\mathbf{u}_{ab} = (-d^x_{ab}, -d^y_{ab}, 0)/\theta_{ab}J_{ab}$ and $\mathbf{u}_{bc} = (-d^x_{bc}, -d^y_{bc}, 0)/\theta_{bc}J_{bc}$, respectively. Now that we have lost two DM terms, we are left with the double QD Hamiltonian of two rotated spins, $J_{bc}R^{\theta_{ab}}_{\mathbf{u}_{ab}}(\mathbf{S}_b)R^{\theta_{bc}}_{\mathbf{u}_{bc}}(\mathbf{S}_c)$. This Hamiltonian is equal to $J_{bc}\mathbf{S}_b \cdot \mathbf{S}_c + \mathbf{d}_{bc}(\mathbf{S}_b \times \mathbf{S}_c)$ if the condition

$$\frac{\mathbf{d}_{ab}}{J_{ab}} + \frac{\mathbf{d}_{bc}}{J_{bc}} + \frac{\mathbf{d}_{ca}}{J_{ca}} = 0 \tag{26}$$

holds. Our calculation shows that equilateral triple QD in zero magnetic field satisfies (26), but does not produce a useful gate. Therefore, architectures with the linear arrangements are the only ones where exchange-only quantum computation proceeds with a simple global redefinition of spin states. In other cases, spin-nonconserving transitions to noncomputational states has to be removed.

6. Conclusions

We have studied triple quantum dot system in linear and triangular arrangements. In the linear arrangement, antiferromagnetic exchange is present between all three pairs of dots. Exchange interaction between the outer dots is smaller than the nearest neighbor exchange but comparable to it when the distances of the neighboring dots is smaller than $2a_B$. The influence of the third dot on the exchange interaction between the other two dots is considerable for both the linear and triangular system in zero magnetic field. Magnetic field suppresses this dependence on the position of third dot. At the critical field strength in the range of 1 T, we observe a transition from antiferromagnetic to ferromagnetic exchange parameters in both linear and triangular setups.

In the linear arrangement, the Dzyaloshinsky–Moriya vectors between every pair of dots point in the same direction, and depend only on Rashba (f_R) and Dresselhaus (f_D) parameters, as well as on the angle θ between the crystallographic axis and the direction connecting the dots. We have shown that Dzyaloshinsky–Moriya vector intensity between two dots is highly dependent on the position of the third one. When $f_D = f_R$ and $\theta = 3\pi/4$ the effects of spin–orbit interaction vanishes, as in the case of double dot. In the magnetic field, dependence of Dzyaloshinsky–Moriya vectors direction on magnetic field as well as on the position of the third dot is observed while Dzyaloshinsky–Moriya vectors intensity is less sensitive to the third dot than in a nonmagnetic case. Anisotropy is always present in triangular arrangements. In this setup, Dzyaloshinsky–Moriya vectors directions are

additionally dependent on the third dot. For the equilateral arrangement, equation $\mathbf{d}_{ab}+\mathbf{d}_{bc}+\mathbf{d}_{ca}=0$ is satisfied, helping us to remove dominant spin–orbit effects by the proper local spin rotation of two quantum dots.

Acknowledgments

This research is funded by the MPNTR grants ON171035 and ON171032, SNF SCOPES IZ73Z0152500, and DAAD grant 451-03-01858201309-3.

Appendix. Details of the Hamiltonian calculation

Matrix elements of S, $\hat{x}$, $\hat{y}$, $\hat{p}_x$ and $\hat{p}_y$ between two Fock–Darwin states $\varphi_i(x,y)=\mathrm{e}^{\mathrm{i}\frac{eB_z}{2\hbar}(x_iy-y_ix)}\sqrt{\frac{m\omega}{\pi\hbar}}\mathrm{e}^{-\frac{m\omega}{2\hbar}((x-x_i)^2+(y-y_i)^2)}$ and $\varphi_j(x,y)=\mathrm{e}^{\mathrm{i}\frac{eB_z}{2\hbar}(x_jy-y_jx)}\sqrt{\frac{m\omega}{\pi\hbar}}\mathrm{e}^{-\frac{m\omega}{2\hbar}((x-x_j)^2+(y-y_j)^2)}$, centered at (x_i,y_i) and (x_j,y_j) are equal to

$$\begin{aligned}S_{ij}=&\langle\varphi_i|\varphi_j\rangle\\&=\exp\left[-\frac{4m^2\omega^2+e^2B_z^2}{16m\omega\hbar}((x_i-x_j)^2+(y_i-y_j)^2)]\,\exp[\mathrm{i}\frac{eB_z}{2\hbar}(y_ix_j-x_iy_j)\right],\end{aligned}\tag{A.1}$$

$$\hat{x}^{ij}=\langle\varphi_i|\hat{x}|\varphi_j\rangle=S_{ij}\left(\frac{1}{2}(x_i+x_j)+\mathrm{i}\frac{eB_z}{4m\omega}(y_i-y_j)\right),\tag{A.2}$$

$$\hat{y}^{ij}=\langle\varphi_i|\hat{y}|\varphi_j\rangle=S_{ij}\left(\frac{1}{2}(y_i+y_j)-\mathrm{i}\frac{eB_z}{4m\omega}(x_i-x_j)\right),\tag{A.3}$$

$$\hat{p}_x^{ij}=\langle\varphi_i|\hat{p}_x|\varphi_j\rangle=S_{ij}\left(\frac{\mathrm{i}m\omega}{2}(x_i-x_j)-\frac{eB_z}{4}(y_i+y_j)\right),\tag{A.4}$$

$$\hat{p}_y^{ij}=\langle\varphi_i|\hat{p}_y|\varphi_j\rangle=S_{ij}\left(\frac{\mathrm{i}m\omega}{2}(y_i-y_j)+\frac{eB_z}{4}(x_i+x_j)\right).\tag{A.5}$$

Matrix element of H_0 (1)

$$\begin{aligned}\langle\varphi_i|H_0|\varphi_j\rangle=&\hbar\omega_0S_{ij}-\frac{m^2\omega_0^2\omega}{2\pi\hbar}(I^p(x_i,x_j)I^s(y_i,y_j)+I^s(x_i,x_j)I^p(y_i,y_j))\\&+\frac{m\omega}{\pi\hbar}\Big[\frac{1}{2}m\omega_0^2(1-\frac{h}{\lambda^2})\sum_{k=a,b,c}(F^s(x_k,x_i,x_j)F^p(y_k,y_i,y_j)\\&+F^p(x_k,x_i,x_j)F^s(y_k,y_i,y_j))\\&+\hbar\omega_0h\big(3\frac{\pi\hbar}{m\omega}S_{ij}-\sum_{k=a,b,c}F^p(x_k,x_i,x_j)F^p(y_k,y_i,y_j)\big)\Big],\end{aligned}\tag{A.6}$$

where

$$\begin{aligned}F^p(x_k,x_i,x_j)&=\sqrt{\frac{\pi}{A}}\exp\left[-\frac{m}{2\hbar}\left(\omega(x_i^2+x_j^2)+\omega_0\frac{x_k^2}{\lambda^2}\right)+\frac{(B+\mathrm{i}E_x)^2}{4A}\right],\\F^s(x_k,x_i,x_j)&=\frac{1}{4A^2}\left[(B+\mathrm{i}E_x)^2+2A(1-2(B+\mathrm{i}E_x)x_k+2Ax_k^2)\right]\\&\quad F^p(x_i,x_j,x_k),\\I^p(x_i,x_j)&=\sqrt{\frac{\pi}{C}}\exp\left[-\frac{m\omega}{2\hbar}(x_i^2+x_j^2)+\frac{(D+\mathrm{i}E_x)^2}{4C}\right],\\I^s(x_i,x_j)&=\frac{1}{4C^2}\left[(D+\mathrm{i}E_x)^2+2C(1-2(D+\mathrm{i}E_x)x_j+2Cx_j^2)\right]I^p(x_i,x_j),\end{aligned}\tag{A.7}$$

with $A=\frac{m}{\hbar}(\omega+\frac{\omega_0}{2\lambda^2})$, $B=\frac{m}{\hbar}(\omega(x_i+x_j)+\omega_0\frac{x_k}{2\lambda^2})$, $C=\frac{m\omega}{\hbar}$, $D=(x_i+x_j)C$, $E_x=\frac{1}{2\hbar}(y_i-y_j)eB_z$.

Expressions $F^p(y_k,y_i,y_j)$ and $F^s(y_k,y_i,y_j)$, $I^p(y_i,y_j)$ and $I^s(y_i,y_j)$ have the same form, only the set of numbers $\{x_k,x_i,x_j\}$ is changed with the set $\{y_k,y_i,y_j\}$ and E_x is changed with $E_y=\frac{1}{2\hbar}(x_j-x_i)eB_z$.

Matrix elements of $\boldsymbol{\Omega}(\boldsymbol{k})$ (9)

$$\begin{aligned}\boldsymbol{\beta}_{ij}=&\langle\varphi_i|\boldsymbol{\Omega}(\boldsymbol{k})|\varphi_j\rangle\\&=\Big[-\frac{\hat{p}_x^{ij}+\frac{1}{2}eB_z\hat{y}^{ij}}{\hbar}(f_\mathrm{D}\cos\theta+f_\mathrm{R}\sin\theta)\\&\quad+\frac{\hat{p}_y^{ij}-\frac{1}{2}eB_z\hat{x}^{ij}}{\hbar}(f_\mathrm{R}\cos\theta-f_\mathrm{D}\sin\theta)\Big]\boldsymbol{e}_x\\&\quad+\Big[-\frac{\hat{p}_x^{ij}+\frac{1}{2}eB_z\hat{y}^{ij}}{\hbar}(f_\mathrm{D}\sin\theta\\&\quad+f_\mathrm{R}\cos\theta)+\frac{\hat{p}_y^{ij}-\frac{1}{2}eB_z\hat{x}^{ij}}{\hbar}(f_\mathrm{D}\cos\theta-f_\mathrm{R}\sin\theta)\Big]\boldsymbol{e}_y.\end{aligned}\tag{A.8}$$

H_SO (1) matrix element between the Fock–Darwin states φ_i and φ_j with spin components included is

$$\begin{aligned}\langle\varphi_i\pm|H_\mathrm{SO}|\varphi_j\mp\rangle=&\Big[-\frac{\hat{p}_x^{ij}+\frac{1}{2}eB_z\hat{y}^{ij}}{\hbar}(f_\mathrm{D}\cos\theta+f_\mathrm{R}\sin\theta)\\&+\frac{\hat{p}_y^{ij}-\frac{1}{2}eB_z\hat{x}^{ij}}{\hbar}(f_\mathrm{R}\cos\theta-f_\mathrm{D}\sin\theta)\Big]\\&+\Big[\pm\mathrm{i}\frac{\hat{p}_x^{ij}+\frac{1}{2}eB_z\hat{y}^{ij}}{\hbar}(f_\mathrm{D}\sin\theta+f_\mathrm{R}\cos\theta)\\&\mp\mathrm{i}\frac{\hat{p}_y^{ij}-\frac{1}{2}eB_z\hat{x}^{ij}}{\hbar}(f_\mathrm{D}\cos\theta-f_\mathrm{R}\sin\theta)\Big].\end{aligned}\tag{A.9}$$

Coulomb interaction Hamiltonian C (1) is two-particle operator whose matrix elements between four different Fock–Darwin states positioned at $\mathbf{a}=(a_1,a_2)$, $\mathbf{b}=(b_1,b_2)$, $\mathbf{c}=(c_1,c_2)$ and $\mathbf{d}=(d_1,d_2)$ ($\varphi_t(x,y)=\mathrm{e}^{\mathrm{i}\frac{eB_z}{2\hbar}(t_1y-t_2x)}\sqrt{\frac{m\omega}{\pi\hbar}}\mathrm{e}^{-\frac{m\omega}{2\hbar}((x-t_1)^2+(y-t_2)^2)}$ for $t\in\{a,b,c,d\}$) is equal to

$$\begin{aligned}C_{abcd}=&\sqrt{\frac{m\omega\pi}{2\hbar}}\exp\Big[\mathrm{i}\frac{eB_z}{8\hbar}[z_1(a_2+b_2-c_2-d_2)\\&+z_2(-a_1-b_1+c_1+d_1)]\Big]\exp[\frac{e^2B_z^2}{32m\omega\hbar}(\alpha_1^2+\alpha_2^2)]\\&\times\exp[\frac{\hbar}{16m\omega}(\zeta_1^2+\zeta_2^2)]I_0(\frac{\hbar}{16m\omega}(\zeta_1^2+\zeta_2^2))\\&\times\exp\left[\frac{m\omega}{8\hbar}\left(|\mathbf{z}|^2-4[|\mathbf{a}|^2+|\mathbf{b}|^2+|\mathbf{c}|^2+|\mathbf{d}|^2]\right)\right],\end{aligned}\tag{A.10}$$

where $\mathbf{z}=\mathbf{a}+\mathbf{b}+\mathbf{c}+\mathbf{d}$, $\alpha_1=a_2+b_2-c_2-d_2$, $\alpha_2=-a_1-b_1+c_1+d_1$, $\zeta_1=-\frac{m\omega}{\hbar}(b_1+d_1-a_1-c_1)+\mathrm{i}\frac{eB_z}{2\hbar}(a_2+d_2-b_2-c_2)$, $\zeta_2=-\frac{m\omega}{\hbar}(b_2+d_2-a_2-c_2)-\mathrm{i}\frac{eB_z}{2\hbar}(a_1+d_1-b_1-c_1)$.

References

[1] Loss D and DiVincenzo D P 1998 *Phys. Rev.* A **57** 120
[2] Imamoglu A, Awschalom D D, Burkard G, DiVincenzo D P, Loss D, Sherwin M and Small A 1999 *Phys. Rev. Lett.* **83** 4204

[3] Kloeffel C and Loss D 2013 *Annu. Rev. Condens. Matter Phys.* **4** 51
[4] Nadj-Perge S, Frolov S M, Bakkers E P A M and Kouwenhoven L P 2010 *Nature* **468** 1084
[5] Schroer M D, Petersson K D, Jung M and Petta J R 2011 *Phys. Rev. Lett.* **107** 176811
[6] Nadj-Perge S, Pribiag V S, Van Den Berg J W G, Zuo K, Plissard S R, Bakkers E P A M, Frolov S M and Kouwenhoven L P 2012 *Phys. Rev. Lett.* **108** 166801
[7] Golovach V N, Borhani M and Loss D 2006 *Phys. Rev.* B **74** 165319
[8] Bonesteel N E, Stepanenko D and DiVincenzo D P 2001 *Phys. Rev. Lett.* **87** 207901
[9] Burkard G and Loss D 2002 *Phys. Rev. Lett.* **88** 047903
[10] Stepanenko D, Bonesteel N E, DiVincenco D P, Burkard G and Loss D 2003 *Phys. Rev.* B **68** 115306
[11] Stepanenko D and Bonesteel N E 2004 *Phys. Rev. Lett.* **93** 140501
[12] Coish W A and Loss D 2005 *Phys. Rev.* B **72** 125337
[13] Khaetskii A V, Loss D and Glazman L 2002 *Phys. Rev. Lett.* **88** 186802
[14] Chekhovich E A, Makhonin M N, Tartakovskii A I, Yacoby A, Bluhm H, Nowack K C and Vandersypen L M K 2013 *Nat. Mater.* **12** 494
[15] Hanson R, Kouwenhoven L P, Petta J R, Tarucha S and Vandersypen L M K 2007 *Rev. Mod. Phys.* **79** 1217
[16] DiVincenzo D P, Bacon D, Kempe J, Burkard G and Whaley K B 2000 *Nature* **408** 339
[17] Fong B H and Wandzura S M 2011 *Quantum Inf. Comput.* **11** 1003
[18] Setiawan F, Hui H-Y, Kestner J P, Wang X and Das Sarma S 2014 *Phys. Rev.* B **89** 085314
[19] Zeuch D, Cipri R and Bonesteel N E 2014 *Phys. Rev.* B **90** 045306
[20] Zeuch D and Bonesteel N E 2016 *Phys. Rev.* A **93** 010303
[21] Taylor J M, Srinivasa V and Medford J 2013 *Phys. Rev. Lett.* **111** 050502
[22] Medford J, Beil J, Taylor J M, Rashba E I, Lu H, Gossard A C and Marcus C M 2013 *Phys. Rev. Lett.* **111** 050501
[23] Doherty A C and Wardrop M P 2013 *Phys. Rev. Lett.* **111** 050503
[24] Hawrylak P and Korkusinski M 2005 *Solid State Commun.* **136** 508
[25] Baart T A, Fujita T, Reichl C, Wegscheider W and Vandersypen L M K 2017 *Nat. Nanotechnol.* **12** 26
[26] Delgado F, Shim Y-P, Korkusinski M and Hawrylak P 2007 *Phys. Rev.* B **76** 115332
[27] Scarola V W, Park K and Das Sarma S 2004 *Phys. Rev. Lett.* **93** 120503
[28] Hsieh C-Y, Rene A and Hawrylak P 2012 *Phys. Rev.* B **86** 115312
[29] Hsieh C-Y, Shim Y-P, Korkusinski M and Hawrylak P 2012 *Rep. Prog. Phys.* **75** 114501
[30] Tarucha S, Austing D G, Honda T, Van Der Hage R J and Kouwenhowen L P 1996 *Phys. Rev. Lett.* **77** 3613
Kouwenhowen L P, Oosterkamp T H, Danoesastro M W S, Eto M, Austing D G, Honda T and Tarucha S 1997 *Science* **278** 1788
[31] Dresselhaus G 1955 *Phys. Rev.* **100** 580
[32] Rashba E I 1960 *Fiz. Tv. Tela* **2** 1224
Rashba E I 1960 *Sov. Phys. Solid State* **2** 1109
[33] Petta J R, Johnson A C, Taylor J M, Laird E A, Yacoby A, Lukin M D, Marcus C M, Hanson M P and Gossard A C 2005 *Science* **309** 2180
Johnson A C, Petta J R, Taylor J M, Yacoby A, Lukin M D, Marcus C M, Hanson M P and Gossard A C 2005 *Nature* **435** 925
[34] Koppens F H L, Buizert C, Tielrooij K J, Vink I T, Nowack K C, Meunier T, Kouwenhoven L P and Vandersypen L M K 2006 *Nature* **442** 766
[35] Gaudreau L, Studenikin S A, Sachrajda A S, Zawadzki P, Kam A, Lapointe J, Korkusinski M and Hawrylak P 2006 *Phys. Rev. Lett.* **97** 036807
[36] Fock V 1928 *Z. Phys.* **47** 446
Darwin C 1930 *Math. Proc. Camb. Phil. Soc.* **27** 86
[37] Marzari N, Mostofi A A, Yates J R, Souza I and Vanderbilt D 2012 *Rev. Mod. Phys.* **84** 1419
[38] Bravyi S, DiVincenzo D P and Loss D 2011 *Ann. Phys.* **10** 2793
[39] Winkler R 2003 *Spin–Orbit Coupling Effects in Two-Dimensional Electron and Hole Systems*, *Springer Tracts in Modern Physics* vol 191 (Berlin: Springer)
[40] Russ M and Burkard G 2015 *Phys. Rev.* B **91** 235411
[41] Weinstein Y S and Hellberg C S 2005 *Phys. Rev.* A **72** 022319
[42] Georgeot B and Mila F 2010 *Phys. Rev. Lett.* **104** 200502
[43] Trif M, Troiani F, Stepanenko D and Loss D 2008 *Phys. Rev. Lett.* **101** 217201
[44] Burkard G, Loss D and DiVincenzo D P 1999 *Phys. Rev.* B **59** 2070
[45] Shim Y-P and Hawrylak P 2008 *Phys. Rev.* B **78** 165317
[46] Dickman S and Hawrylak P 2003 *JETP* **77** 34
[47] Levitov L S and Rashba E I 2003 *Phys. Rev.* B **67** 115324
[48] Aleiner I L and Fal'ko V I 2001 *Phys. Rev. Lett.* **87** 256801
[49] Baruffa F, Stano P and Fabian J 2010 *Phys. Rev. Lett.* **104** 126401
Baruffa F, Stano P and Fabian J 2010 *Phys. Rev.* B **82** 045311

Ceramics International 43 (2017) 16531–16538

Contents lists available at ScienceDirect

Ceramics International

journal homepage: www.elsevier.com/locate/ceramint

Dielectric and ferroelectric properties of Ho-doped $BiFeO_3$ nanopowders across the structural phase transition

Bojan Stojadinović[a], Zorana Dohčević-Mitrović[a,*], Dimitrije Stepanenko[a], Milena Rosić[b], Ivan Petronijević[c], Nikola Tasić[d], Nikola Ilić[d], Branko Matović[b], Biljana Stojanović[d]

[a] Center for Solid State Physics and New Materials, Institute of Physics Belgrade, University of Belgrade, Pregrevica 118, 11080 Belgrade, Serbia
[b] Institute for Nuclear sciences, Centre of Excellence-CextremeLab "Vinča", University of Belgrade, 11000 Belgrade, Serbia
[c] Faculty of Physics, University of Belgrade, Studentski trg 12-16, 11000 Belgrade, Serbia
[d] Institute for Multidisciplinary Research, University of Belgrade, Kneza Višeslava 1, 11000 Belgrade, Serbia

ARTICLE INFO

Keywords:
Sol-gel processes
X-ray methods
Dielectric properties
Ferroelectric properties
Perovskites

ABSTRACT

We have studied Ho-doped $BiFeO_3$ nanopowders ($Bi_{1-x}Ho_xFeO_3$, x = 0–0.15), prepared via sol-gel method, in order to analyse the effect of substitution-driven structural transition on dielectric and ferroelectric properties of bismuth ferrite. X-ray diffraction and Raman study demonstrated that an increased Ho concentration ($x \geq 0.1$) has induced gradual phase transition from rhombohedral to orthorhombic phase. The frequency dependent permittivity of $Bi_{1-x}Ho_xFeO_3$ nanopowders was analysed within a model which incorporates Debye-like dielectric response and dc and ac conductivity contributions based on universal dielectric response. It was shown that influence of leakage current and grain boundary/interface effects on dielectric and ferroelectric properties was substantially reduced in biphasic $Bi_{1-x}Ho_xFeO_3$ ($x > 0.1$) samples. The electrical performance of $Bi_{0.85}Ho_{0.15}FeO_3$ sample, for which orthorhombic phase prevailed, was significantly improved and $Bi_{0.85}Ho_{0.15}FeO_3$ has sustained strong applied electric fields (up to 100 kV/cm) without breakdown. Under strong external fields, the polarization exhibited strong frequency dependence. The low-frequency remnant polarization and coercive field of $Bi_{0.85}Ho_{0.15}FeO_3$ were significantly enhanced. It was proposed that defect dipolar polarization substantially contributed to the intrinsic polarization of $Bi_{0.85}Ho_{0.15}FeO_3$ under strong electric fields at low frequencies.

1. Introduction

Multiferroics, materials which simultaneously exhibit at least two ferroic properties among electric, magnetic, and elastic responses, are quite rare. They are of great interest for both fundamental physics and potential applications. Among multiferroic materials, bismuth ferrite ($BiFeO_3$) possesses unique property, i.e. exhibits multiferroic behavior at room temperature. Having high ferroelectric ($T_C \sim 1100$ K) and antiferromagnetic ($T_N \sim 640$ K) transition temperatures, $BiFeO_3$ is a promising material for the applications in spintronic devices, electrically controlled magnetic memories and functional sensors [1,2]. Nevertheless, problems of low resistivity and sinterability and appearance of secondary phases present a serious obstacle for the application of $BiFeO_3$ (BFO) in devices. BFO suffers from high leakage current which causes large dielectric loss and degradation of the ferroelectric properties. The main cause of leakage is disorder, usually in the form of charge defects, like oxygen or bismuth vacancies and secondary phases. Attempts at minimizing the leakage current density through doping with rare earth ions at Bi sites, have led to improvement of electric and magnetic properties of BFO [3–6]. These studies have demonstrated that substitution of Bi sites with rare-earth ions effectively controls the volatility of Bi^{3+} ions and the amount of defects, while suppressing the secondary phase appearance.

Despite a significant body of work dealing with rare-earth doped BFO [3,4,7–10], BFO doped with Ho is less investigated. There are several studies dealing with the influence of Ho doping on leakage current, and on magnetic or ferroelectric properties of BFO, for which BFO is either phase stabilized [11–16] or exhibits biphasic character with increased Ho doping [17–20]. Among these studies, only Song and coauthors [20] showed that dielectric constant was significantly increased with small amount of Ho substitution (x = 0.05, 0.10) for which BFO retained rhombohedral structure and then decreased when the orthorhombic phase appeared with higher doping (x = 0.15, 0.20). They also deduced that the dielectric loss of doped samples behaves in a complicated manner, probably influenced by the conductivity of material. Song and coauthors did not analyse the reasons of obtaining

* Corresponding author.
E-mail address: zordoh@ipb.ac.rs (Z. Dohčević-Mitrović).

http://dx.doi.org/10.1016/j.ceramint.2017.09.038
Received 3 July 2017; Received in revised form 22 August 2017; Accepted 5 September 2017
Available online 06 September 2017

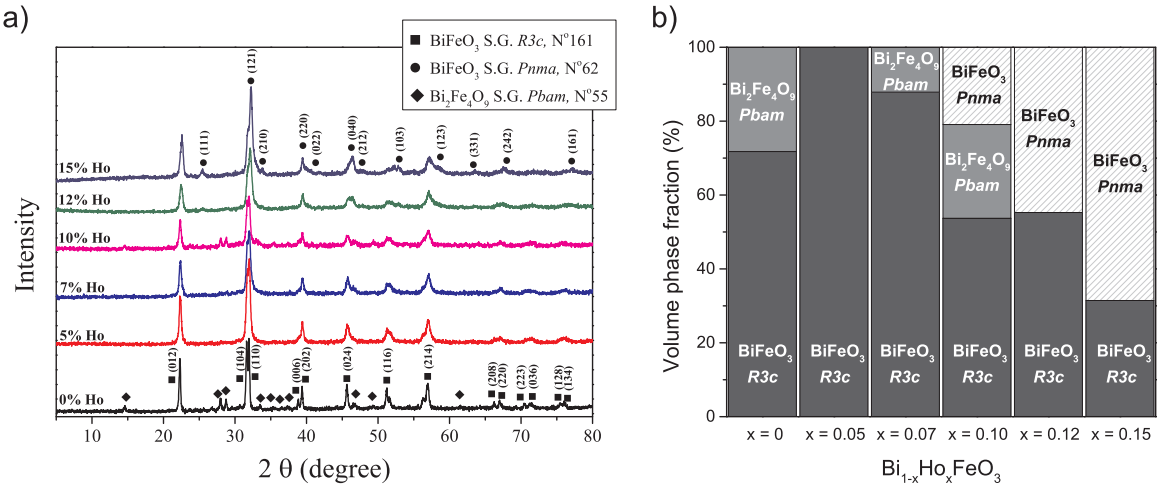

Fig. 1. a) X-ray diffraction patterns and b) volume phase fraction analysis of the $Bi_{1-x}Ho_xFeO_3$ ($0 \le x \le 0.15$) samples.

colossal dielectric constant, nor assumed that quite often these phenomena can be explained by Maxwell-Wagner-type contributions of depletion layers at the interface between sample and contacts or at grain boundaries. Furthermore, it is quite reasonable to assume that various polarization mechanisms can appear in biphasic BFO and influence the dielectric and ferroelectric properties of BFO. To the best of our knowledge, influence of structural phase transformation caused by Ho doping on polarization mechanisms, which can exert a strong influence on the dielectric and ferroelectric properties of BFO, has not been studied.

Herein, we investigated how the structural phase transformation induced by Ho doping influenced the dielectric and ferroelectric properties of $Bi_{1-x}Ho_xFeO_3$ nanopowders. Detailed analysis of the frequency dependent permittivity, using combined model which incorporated Debay-like dielectric relaxation, as well as dc and ac conductivity contributions, was performed. This analysis enabled us to estimate the influence of leakage current and grain boundary/interface effects on the dielectric and ferroelectric properties of single phase and biphasic $Bi_{1-x}Ho_xFeO_3$ nanopowders. Origin of improved electric performances of biphasic $Bi_{1-x}Ho_xFeO_3$ nanostructures, for which orthorhombic phase prevailed, was discussed in detail. These results may provide new insight into modified electrical properties of $BiFeO_3$ by Ho doping, which can be important for potential applications.

2. Experimental procedure

2.1. Materials synthesis

$Bi_{1-x}Ho_xFeO_3$ (x = 0, 0.05, 0.07, 0.10, 0.12, and 0.15) powders were synthesized by a sol-gel method. The stoichiometric amounts of bismuth nitrate ($Bi(NO_3)_3{\cdot}6H_2O$), iron nitrate ($Fe(NO_3)_3{\cdot}9H_2O$), and holmium nitrate ($Ho(NO_3)_3{\cdot}5H_2O$) were used. 2-Methoxyethanol and acetic acid (CH_3COOH) were mixed and stirred for 30 min, before adding the nitrates. Obtained solutions were stirred and heated at 80 °C. After a partial liquid evaporation, the solutions have turned into brown gels. The gels were dried for 45 min at 150 °C. Dried samples were calcinated at 650 °C for 6 h. The pristine and doped samples were named according to the Ho content as BFO, BHFO5, BHFO7, BHFO10, BHFO12 and BHFO15.

2.2. Materials characterization

The phase composition and crystal structure of $Bi_{1-x}Ho_xFeO_3$ samples were analysed using X-ray diffractometer Rigaku Ultima IV with nickel filtered Cu K_α radiation in the 2θ range of 10–80° with the step of 0.02° and the scanning rate of 0.5°/min. XRD pattern analysis was performed using Powder Cell programme (http://powdercell-for-windows.software.informer.com/2.4/) [21]. The TCH pseudo-Voigt profile function gave the best fit to the experimental data. The surface morphology was studied by scanning electron microscopy (SEM, TESCAN SM-300). The micro-Raman spectra were measured at room temperature using a Jobin Yvon T64000 spectrometer equipped with a nitrogen-cooled CCD detector. The λ = 532 nm line of solid state Nd:YAG laser was used as an excitation source with an incident laser power less than 40 mW in order to minimize the heating effects. The dielectric properties of the samples were examined in the frequency range of 80 Hz to 8 MHz. The Digital Programmable LCR Bridge HM8118 (Hameg) was used in the range 80 Hz–120 kHz, and the Digital LCR Meter 4285 A (HP/Agilent) was used in the range 80 kHz–8 MHz. Each sample was placed in a closed capacitor cell housed in a Faraday cage with an AC signal of 1.5 V applied across the cell. The disk-shaped samples had a diameter close to the diameter of the cell electrodes (8 mm). Standard bipolar measurements in the frequency range 1 Hz–1 kHz were performed on Precision Multiferroic Test System (Radiant Technologies, Inc.), using a triangular electric field waveform. All measurements were performed at room temperature.

3. Results and discussion

Fig. 1(a) shows XRD patterns of the $Bi_{1-x}Ho_xFeO_3$ ($0 \le x \le 0.15$) samples. The XRD pattern of pristine BFO matches the rhombohedral *R3c* structure with a presence of weak diffraction peaks which correspond to the orthorhombic $Bi_2Fe_4O_9$ secondary phase of *Pbam* space group (№ 55, ICSD #20067). XRD spectra of the BHFO5 and BHFO7 samples maintain *R3c* structure. No secondary peaks were detected in BHFO5 sample, whereas the traces of secondary phase were observed in the BHFO7 sample. Addition of Ho dopant induced a gradual broadening of XRD peaks and their shifts towards higher angles. These changes suggest structural distortion of BFO lattice and can be attributed to the unit cell contraction due to the substitution of Bi^{3+} ions with smaller Ho^{3+} dopant. Significant changes with increased Ho concentration were observed in doublet (104) and (110) diffraction peaks at 2θ ~ 32°. These peaks were shifted towards larger 2θ values, and in the samples with higher Ho content (x > 0.07) they gradually merged into a single broad peak (BHFO15 sample). In addition, the (006), (116) and (202) diffraction peaks of *R3c* phase became weak and disappeared in the samples with higher Ho concentration (x > 0.1). In the spectra of BHFO12 and BHFO15 samples, a new single peak appeared at 2θ ~ 38°, whereas additional peak at 2θ ~ 25° was found in BHFO15 sample.

Such changes have already been seen in the XRD spectra of doped

Table 1
The lattice parameters (Å), volume of the unit cell (Å^3) and volume phase fraction (vol%).

Phase	BFO	BHFO5	BHFO7	BHFO10	BHFO12	BHFO15
$BiFeO_3$ rhombohedral *R3c*	a = 5.5722 c = 13.8511 V = 372.45 71.75%	a = 5.5636 c = 13.8216 V = 370.51 100.00%	a = 5.5575 c = 13.8145 V = 369.51 87.86%	a = 5.5651 c = 13.8143 V = 370.51 53.72%	a = 5.5675 c = 13.8542 V = 371.91 55.27%	a = 5.5441 c = 13.8127 V = 367.68 31.45%
$Bi_2Fe_4O_9$ orthorhombic *Pbam*	a = 7.9477 b = 8.4582 c = 6.0050 V = 403.68 28.25%	/	a = 7.9769 b = 8.5299 c = 5.9448 V = 404.50 12.14%	a = 7.9501 b = 8.4580 c = 5.9976 V = 403.29 25.36%	/	/
$BiFeO_3$ orthorhombic *Pnma*	/	/	/	a = 5.5830 b = 7.8825 c = 5.4192 V = 238.49 20.92%	a = 5.5993 b = 7.8679 c = 5.4540 V = 240.27 44.73%	a = 5.5907 b = 7.8129 c = 5.4297 V = 237.17 68.55%
Rp	5.81	6.27	5.94	4.86	6.18	5.42
Rwp	7.44	7.92	7.60	6.14	7.92	6.91
Rexp	0.11	0.12	0.09	0.06	0.07	0.09

$BiFeO_3$ nanoparticles [17,22], ceramics [23–25] and films [26], and were ascribed to the presence of orthorhombic phase. All these notable changes in the XRD spectra indicate structural phase transformation from rhombohedral to orthorhombic phase in the samples doped with higher Ho content (x = 0.10, 0.12 and 0.15). $Bi_2Fe_4O_9$ phase is still present in the BHFO10 sample, but with further increase of Ho doping (BFHO12 and BFHO15 samples) the secondary $Bi_2Fe_4O_9$ phase is completely suppressed. Furthermore, the absence of diffraction peaks which correspond to Ho oxides, even at higher concentrations, implies that Ho ions have entered substitutionally into BFO lattice.

The measured XRD patterns were further refined using PowderCell programme in order to calculate the structural parameters and estimate the volume fraction of each phase. The best fits of the measured data were obtained using rhombohedral *R3c* structure for BHFO5 and BHFO7 samples. The orthorhombic phase appeared in BHFO10 samples and with further Ho doping this phase becomes dominant in BHFO15 sample. Unit cell parameters and the estimated volume fractions of different phases are presented in Table 1 for pristine and Ho-doped BFO samples. The decreasing trend in lattice constants and the unit cell contraction of *R3c* phase confirm that Bi^{3+} ions are substituted with smaller Ho^{3+} ions. A similar behavior has been reported in Tb-doped $BiFeO_3$ [10] as well as in rare-earth doped $BiFeO_3$ ceramics [27,28]. The slight increase of *R3c* phase lattice parameters in BHFO10 and BHFO12 samples can be ascribed to increased strain at phase boundary between rhombohedral and orthorhombic crystal structure. Levin et al. have also found abrupt expansion of the *R3c* unit cell volume at the rhombohedral-orthorombic phase transition in Nd-substituted $BiFeO_3$ [29]. The results of quantitative phase analysis of the $Bi_{1-x}Ho_xFeO_3$ samples are presented in Fig. 1(b).

The influence of structural changes on surface morphology of BFO is illustrated in Fig. 2, where the SEM images of pristine and BHFO15 samples are shown for comparison. Changes in the surface morphology are clearly visible. Certain amount of intergranular porosity and non-uniformity of particles can be observed in the BFO sample, including very small spherical particles and big clumps. With incorporation of Ho^{3+} ions in BFO, the particles became more uniform and compact, whereas the particle size was reduced, as seen in 10% Ho-doped BFO [30]. In the enlarged images (Fig. 2c and d) it can be seen that pure and Ho-doped BFO samples consist of small particles and large irregularly shaped agglomerates.

Changes of $Bi_{1-x}Ho_xFeO_3$ crystal structure are reflected in the changes of $BiFeO_3$ vibrational properties, i.e. through the changes in intensity, position, and width of the Raman modes. Fig. 3 shows the room-temperature Raman spectra of $Bi_{1-x}Ho_xFeO_3$ samples. Raman spectrum of undoped $BiFeO_3$ was deconvoluted using Lorentzian profiles and all 13 Raman active modes ($4A_1 + 9E$) of the rhombohedral $BiFeO_3$ [31] are observed. The most prominent Raman modes for *R3c* structure (marked as E-1, A_1-1, A_1-2, and A_1-3) are positioned at 75, 140, 171, and 218 cm^{-1}, respectively and are related to Bi–O bonds. The A_1-4 mode at 430 cm^{-1} and eight E modes at 124, 274, 344, 369, 468, 520, 550 and 598 cm^{-1} with quite weak scattering intensity are related to Fe–O bonds.

Raman spectroscopy is sensitive to atomic displacements. The A_1-1, A_1-2 and A_1-3 modes are blue-shifted due to the substitution of Bi^{3+} ions with smaller Ho^{3+} ions. Modes E-1, A_1-1, A_1-2 and A_1-3 became broader and of reduced intensity, whereas higher frequency E modes (E-4, E-5) have almost disappeared. The peak broadening and reduced intensities of Raman modes imply the distortion of rhombohedral structure with incorporation of Ho. With increasing Ho concentration ($x \geq 0.1$), further changes in the Raman spectra are the result of decreased stereochemical activity of Bi lone electron pair. The intensities of A_1 and E modes are drastically reduced in BHFO10 and BHFO12 samples. These modes are barely visible in the Raman spectra of BHFO15 sample. Moreover, in BHFO12 sample three new modes approximately at 300, 400, and 510 cm^{-1}, are observed. Reduced intensities of phonon modes, characteristic for rhombohedral phase, and the presence of additional modes suggest the appearance of new crystalline phase. In the Raman spectrum of BFHO15 sample which is significantly different from the spectrum of pristine BFO, the most prominent modes are at ~ 300, 400, and 510 cm^{-1}. These modes are characteristic for orthorhombic perovskite $LaMnO_3$ and $YMnO_3$ structures [32] and are also observed in doped BFO powders [17]. All notable changes in the Raman spectra of BHFO12 and BHFO15 samples are consistent with the results of XRD analysis, confirming a structural transformation from rhombohedral to orthorhombic paraelectric phase. Hence, Raman spectroscopy is powerful tool for detecting changes of Bi–O covalent bonds during the phase transition.

Fig. 4(a) and (b) illustrate the frequency dependence of real (ε') and imaginary (ε'') part of the complex permittivity ε of $Bi_{1-x}Ho_xFeO_3$ samples. In the lower frequency range, both ε' and ε'' decrease with increasing frequency and become nearly constant at higher frequencies. Among the samples with *R3c* structure, BHFO5 sample has shown pronounced dispersion at lower frequencies and higher values of ε' and ε'' than BFO. The BHFO7 sample displayed almost no dispersion over the whole frequency range. Among the samples with higher Ho content in which orthorombic phase appears, BHFO10 sample displayed more dispersive characteristic than BHFO12 and BHFO15 samples for which permittivity dispersions were negligible.

BFO nanostructures in the form of nanopowders or thin films usually suffer from large leakage current due to the presence of oxygen vacancies, Fe^{2+} ions or some other impurities. The inhomogeneity of BFO microstructure and composition originates from the regions with

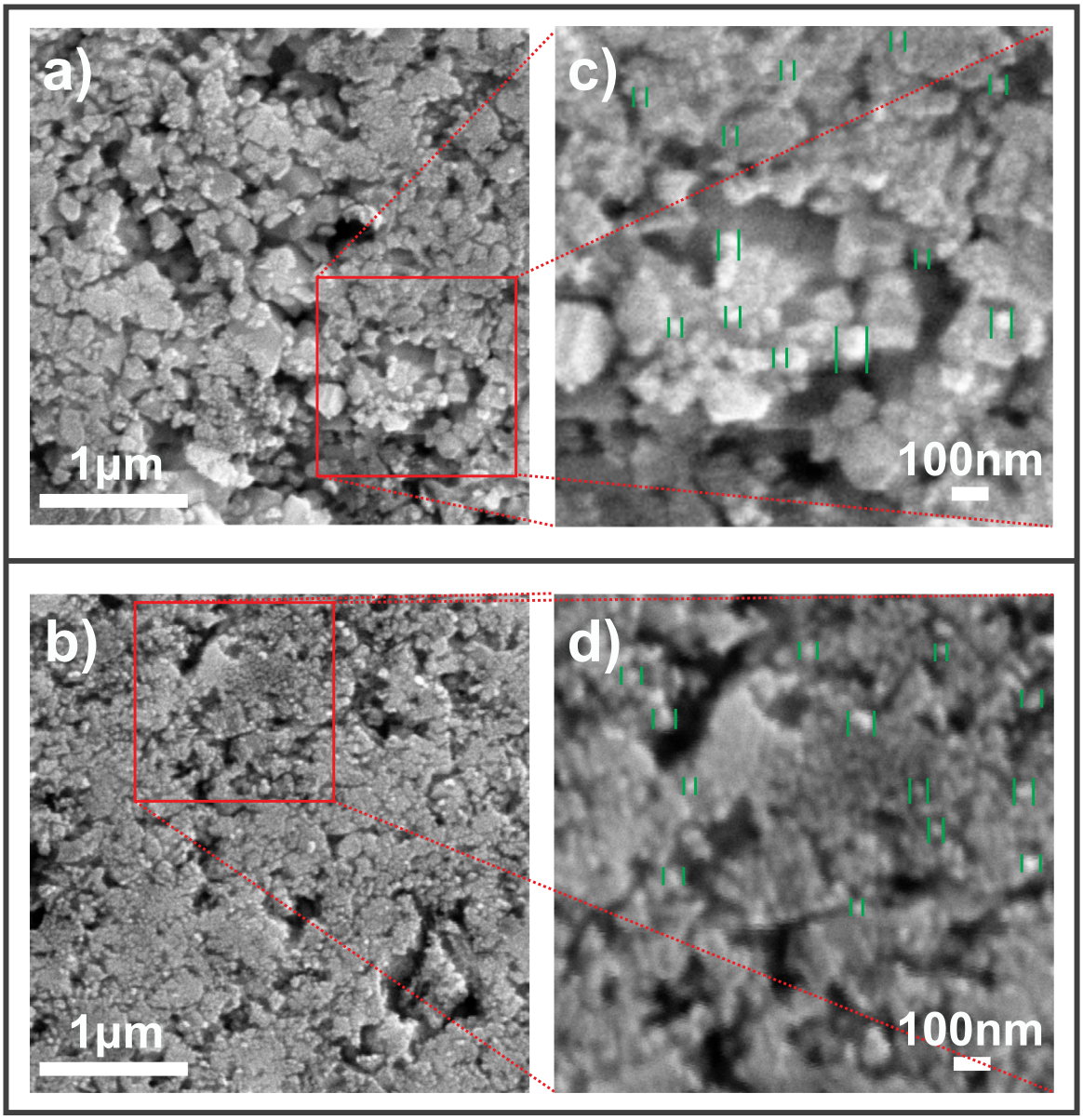

Fig. 2. SEM images of a) $BiFeO_3$ and b) $Bi_{0.85}Ho_{0.15}FeO_3$ samples. High-magnification SEM images of the c) $BiFeO_3$ and d) $Bi_{0.85}Ho_{0.15}FeO_3$ samples.

different conductivity, for example bulk and grain boundaries or from depletion layers formed at the interface of the electrode/sample surface. In addition to the dipolar or orientational polarization which occurs in the frequency range of 10^3–10^6 Hz, the grain boundary or interface effects give rise to the Maxwell-Wagner polarization which can substantially contribute to the permittivity and its dispersion at lower frequencies [3].

The dielectric relaxation processes in pure and Ho-doped BFO nanopowders were analysed within a model which includes Cole-Cole empirical expression, dc and ac conductivity terms. This model describes dielectric relaxation processes due to dipole relaxation, and the contributions from leakage current and grain boundary/interface effects. The advantages of this model for analyzing the dielectric properties of pristine $BiFeO_3$ films have been shown by Li and coworkers [33]. The total complex permittivity is of the form [33,34]:

$$\varepsilon = \varepsilon' + i\varepsilon'' = \frac{\varepsilon_s - \varepsilon_\infty}{1+(i\omega\tau)^{1-\alpha}} + \frac{\sigma_0}{\varepsilon_0} tan\left(\frac{\pi s}{2}\right)\omega^{s-1} + i\left(\frac{\sigma_{DC}}{\omega\varepsilon_0} + \frac{\sigma_0}{\varepsilon_0}\omega^{s-1}\right) \quad (1)$$

The first term in Eq. (1) corresponds to the Cole-Cole formula, where ε_s and ε_∞ are static and high frequency dielectric permittivity, τ is the relaxation time, andα, taking the value between 0 and 1, describes the distribution of relaxation times. For an ideal Debye relaxation $\alpha = 0$. For $\alpha < 0$ the loss peaks are broader and deviate in shape from the symmetric Debye peak [35]. The frequency-independent dc conductivity contributes only to the imaginary part of permittivity (ε'') through the term $\sigma_{DC}/\omega\varepsilon_0$, whilst the frequency-dependent ac conductivity represented by UDR ansatz [34,35], influences both ε' and ε'' through terms $(\sigma_0/\varepsilon_0)tan\left(\frac{\pi s}{2}\right)\omega^{s-1}$ and $(\sigma_0/\varepsilon_0)\,\omega^{s-1}$, where σ_0 is a pre-power term and s is a frequency exponent which takes values between 0 and 1.

The fits of $\varepsilon'(\omega)$ and $\varepsilon''(\omega)$, based on Eq. (1), are presented with solid lines on Figs. 4(a) and 4(b) and the values of fit parameters for $Bi_{1-x}Ho_xFeO_3$ samples are summarized in Table 2. The values of σ_{DC} and σ_0 for $Bi_{1-x}Ho_xFeO_3$ samples, based on the fitting results, are presented in Fig. 4(d). BFO sample has relatively high σ_{DC} value of $6.1{\cdot}10^{-9}\,\Omega^{-1}\,cm^{-1}$, whereas the value of σ_0 is an order of magnitude lower. These values are comparable with reported data [15,33,36]. It can be concluded that the permittivity of BFO sample is dominated by the leakage current contribution, whereas the ac dependent mechanisms are less prominent. Among the Ho-doped samples with *R3c*

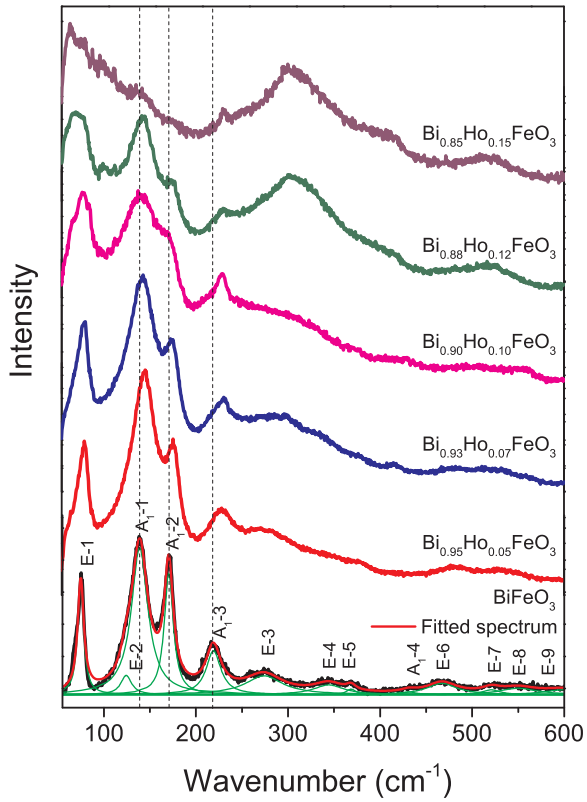

Fig. 3. Room-temperature Raman spectra of the $Bi_{1-x}Ho_xFeO_3$ ($0 \le x \le 0.15$) samples together with the deconvoluted Raman spectrum of pristine $BiFeO_3$.

structure, the highest dc and ac conductivity exhibits the BFHO5 sample, meaning that leakage current and grain boundary or interface effects can be a cause of permittivity dispersion and its higher value at lower frequencies. This finding offers an explanation for the collosal dielectric constant of Ho doped samples found by Song et al. [20]. The σ_{DC} and σ_0 values of BHFO7 sample are much lower than in BFO and BHFO5 samples. Despite the fact that the amount of secondary phase in BFHO7 is almost the same as in pristine BFO and having in mind that BFHO5 sample is phase pure, it seems that BHFO5 and BFO samples are more conductive than BHFO7 sample. This fact can explain the flat frequency dependence of $\varepsilon'(\omega)$ and $\varepsilon''(\omega)$ (Figs. 4(a) and (b)) of BHFO7 sample and imply that the presence of secondary phase has no great influence on the BFO conductivity, but defects in the form of oxygen vacancies and grain boundary or interface effects play a major role in the conductivity of BHFO5 and BFO samples. A significant increase of σ_{DC} value, which is almost twice as large as in pristine BFO and BHFO5 samples, was found in a case of BHFO10. Although it is expected that increased Ho doping reduces the leakage current due to the suppressed concentration of oxygen and bismuth vacancies, this sample seems to be more leaky than the pristine BFO. The σ_{DC} value, higher than in all the other samples, and pronounced dispersion of $\varepsilon''(\omega)$ implies that the leakage current affects the dielectric properties of BHFO10 to a great extent.

The changes in dielectric properties of BHFO10 sample can be related to the appearance of orthorhombic phase, because the dielectric properties are dependent on the sample structure and therefore can be modified near the phase transformation boundary [3]. The dc and ac conductivities were significantly reduced in BHFO12 sample, whereas BHFO15 sample, for which orthorhombic phase prevails, had an order of magnitude lower dc conductivity ($5.7 \cdot 10^{-10}\ \Omega^{-1}\ cm^{-1}$) than the BFO ($6.1 \cdot 10^{-9}\ \Omega^{-1}\ cm^{-1}$). Therefore, we argue that higher Ho content reduces the leakage current, and weakens the ac conductivity contribution to the dielectric response. The frequency dependence of dielectric loss (*tan δ*) of $Bi_{1-x}Ho_xFeO_3$ samples is presented in Fig. 4(c). The dielectric loss follows a trend similar to the permittivity in the frequency range of 100 Hz to 8 MHz, i.e. it decreases with increasing frequency. The BFO, BHFO5 and BHFO10 samples have higher *tan δ* value than other Ho-doped samples with pronounced dispersion at lower frequencies. There is an indication of dielectric relaxation peak in conductive BFO and BHFO10 samples at frequency of 5 kHz, which can be ascribed to the carrier hopping process between Fe^{2+} and Fe^{3+} ions inside the particles [37] or to the hopping along the Fe^{2+}-$V_O^{\bullet}$ -Fe^{3+} chain [38]. This peak is slightly shifted to lower frequency in BHFO5 sample. This low frequency relaxation can be attributed to the grain boundary conduction [39]. Reduced *tan δ* values and the absence of relaxation peaks in BHFO7, BHFO12 and BHFO15 samples point at an increased resistivity of these samples.

Polarization-electric field (P-E) hysteresis loops of $Bi_{1-x}Ho_xFeO_3$ samples, measured at frequency of 100 Hz, are presented in Fig. 5(a). The BFO sample has an unsaturated P-E loop due to non negligible contribution of leakage current ($\sigma_{DC} = 6.1 \cdot 10^{-9}\ \Omega^{-1}\ cm^{-1}$). The maximal polarization, remnant polarization (P_r), and coercive field (E_c) reached the highest values in BFO sample and decreased with Ho-doping. The BHFO5 sample has a pinched P-E loop, characteristic for leaky materials. The permittivity analysis has shown that BHFO5 is less resistive than BFO and that grain boundary effects and leakage current dominate its dielectric properties. Therefore, the degraded ferroelectric properties can be attributed to the presence of oxygen vacancies and valence fluctuations of Fe ions (between Fe^{3+} and Fe^{2+}), because the appearance of oxygen vacancies and Fe^{2+} ions, especially at grain boundaries, is unfavorable for the polarization switching. The study of dielectric properties has shown that BHFO7 is more resistive than BFO and BHFO5. This fact explains slightly improved P-E loop compared to BHFO5 sample, but still lower P_r and E_c values than in BFO can originate from a decrease in stereochemical activity of Bi lone electron pair with increase of Ho content. P-E loops of the BHFO10, BHFO12 and BHFO15 samples are very similar to the P-E loops of BHFO5 sample. The degraded ferroelectricity of BHFO10 mainly originates from the contribution of dc conductivity (σ_{DC}) which is the highest among all analysed samples (see Fig. 4(d) and Table 2). Although BHFO12 and BHFO15 samples are more resistive than BFO and all the other Ho-doped samples, their ferroelectric properties are degraded because of the possible appearance of paraelectric phase regions in highly Ho doped BFO. This is supported by the changes noticed in the Raman spectra of these samples. Near the ferroelectric-paraelectric phase transition, the intensities of the Raman modes characteristic for Bi–O bonds [28] were reduced in BHFO12 sample and have almost disappeared in BHFO15 sample.

Furthermore, the presence of orthorhombic phase increases the breakdown field strength of $Bi_{1-x}Ho_xFeO_3$ samples (inset of Fig. 5(a)). The breakdown in BFO and $Bi_{1-x}Ho_xFeO_3$ samples with rhombohedral structure ($x < 0.1$) happens at the applied electric fields of around 20 kV/cm. The BHFO10 and BHFO12 samples, in which rhombohedral and orthorhombic phase coexist, withstand applied fields that are approximately twice as high. The BHFO15 sample in which orthorhombic phase prevails, withstands even higher electric fields (> 50 kV/cm) without breakdown (marked with arrow on the inset). The reason can be found in reduced dc conductivity of BHFO15 and in increasing number of Ho–O bonds with large bond energy, almost two times larger than the Bi–O bond [15]. Knowing that BHFO15 sample withstands high external fields without breakdown, the P-E loops of BHFO15 sample were measured at different testing frequencies from 2 Hz to 100 Hz under the applied field of 50 kV/cm, as shown in Fig. 5(b). It is obvious that P-E loops exhibit frequency-dependent behavior by showing rapid increase of P_r, E_c and maximal polarization at lower frequencies. Frequency dependence of the $2P_r$ for BHFO15 sample is presented in the top-left inset of Fig. 5(b), from which it is clear that $2P_r$ has the highest value of 0.21 μC/cm^2 at 2 Hz and rapidly decreases to 0.07 μC/cm^2 at 20 Hz. The P-E loops of BHFO15 measured in a high amplitude electric field of 100 kV/cm and at low frequencies of 1 Hz

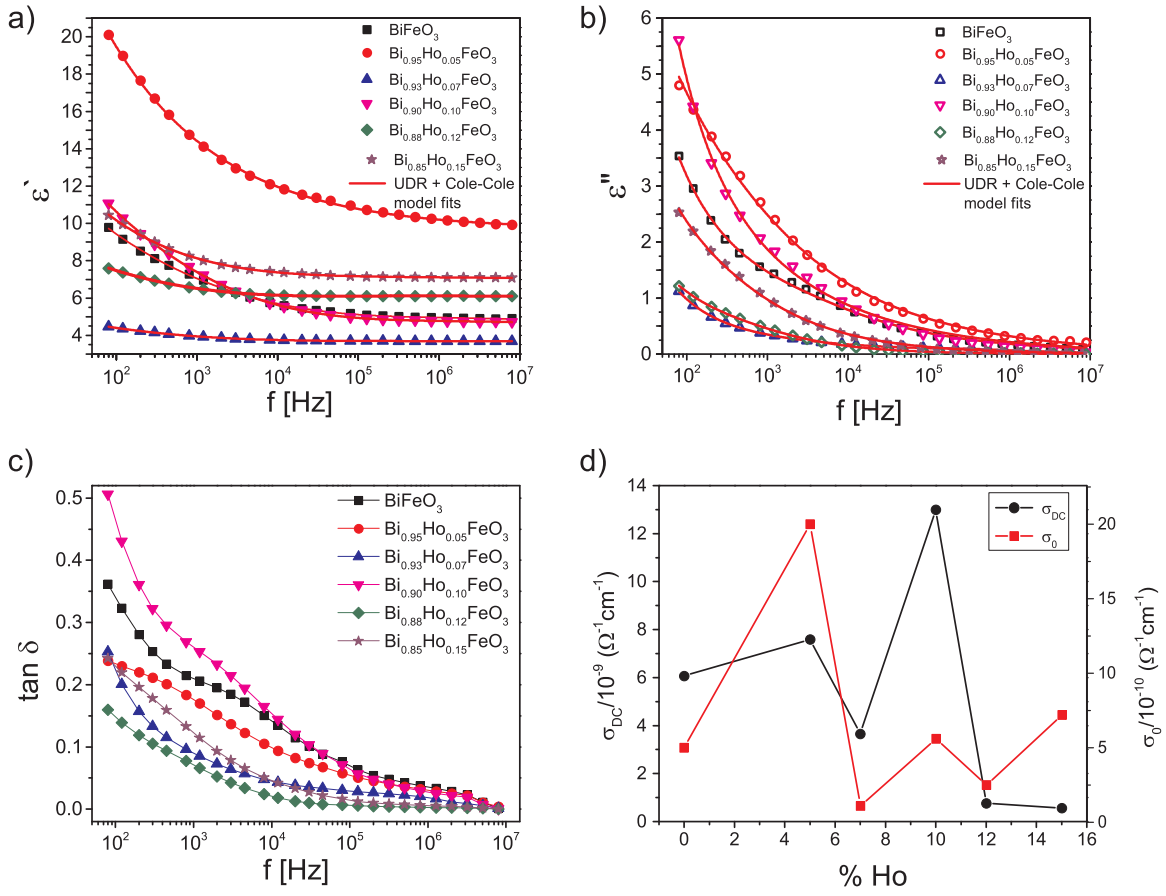

Fig. 4. Room-temperature (a) real (ε') and (b) imaginary (ε'') part of the complex permittivity. Full lines present the corresponding fits applying the combined model (Eq. 1), (c) loss tangent ($tan\ \delta$) and (d) the dependence of σ_{DC} and σ_0 values on Ho content for $Bi_{1-x}Ho_xFeO_3$ samples.

and 2 Hz are presented in the right-bottom inset of Fig. 5(b). The $2P_r$ value is larger by a factor of two than the one obtained at the same frequency in the field of 50 kV/cm. Such a behavior can be explained by the effect of external field on the reorientation of defect dipoles and their role in domain wall switching in BFO. The presence of mobile, single defects (like V'''_{Bi}, $V^{\bullet}_{O}$ or $V^{\bullet\bullet}_{O}$) or defect complexes (oxygen vacancy-cation associated dipoles) in BFO plays an important role in the domain wall pinning. It leads to the deterioration of polarization-switching properties by suppression of intrinsic polarization and increase of leakage current. The ferroelectric domain depinning can be achieved by applying high electric field or can be favoured at elevated temperatures and a secondary re-oxidation annealing [40–43]. On the other hand, in high electric fields the defect complexes can orient along the direction of spontaneous polarization and follow the domain switching, enhancing polarization properties of BFO [42–45]. Inherent defect dipoles are expected not to switch during fast field cycling, since their reorientation takes more time than the domain switching process. Therefore, the influence of defect dipole polarization on the overall polarization can be seen in high fields at low frequencies, as defect complexes can keep up with reversal of the field and contribute to the bulk ferroelectric polarization [40,44]. It is plausible to suppose that inherent defect complexes like $V'''_{Bi} - V^{\bullet\bullet}_{O}$, $Fe'_{Fe^{2+}} - V^{\bullet}_{O}$ or $Fe'_{Fe^{2+}} - V^{\bullet\bullet}_{O}$ form during the crystallization process in $Bi_{1-x}Ho_xFeO_3$ samples. Among all $Bi_{1-x}Ho_xFeO_3$ samples, only BHFO15 sample has supported high external field of 50 kV/cm which can induce defect dipole reorientation. By applying strong external field at low frequencies, defect dipoles can orient along the direction of spontaneous polarization following the domain switching. With increasing of the field strength to 100 kV/cm and by lowering the frequency to 1 Hz, the effect of defect dipolar polarization was more pronounced. Therefore, the reorientation of internal defect complexes under high external field gives rise to the enhancement of intrinsic polarization of BHFO15 sample.

4. Conclusions

In summary, the phase transformation from rhombohedral to orthorhombic phase induced by increased Ho substitution, affected to a great extent the dielectric and ferroelectric properties of $Bi_{1-x}Ho_xFeO_3$ nanopowders. The frequency dependent permittivity was analysed using combined model which incorporated Debye-like dielectric

Table 2
The fitting parameters for $Bi_{1-x}Ho_xFeO_3$ samples obtained from combined model.

Parameter	BFO	BHFO5	BHFO7	BHFO10	BHFO12	BHFO15
α	0.55	0.69	0.65	0.69	0.60	0.67
τ(s)	$5.3{\cdot}10^{-6}$	$2.2{\cdot}10^{-6}$	$5.2{\cdot}10^{-5}$	$1.2{\cdot}10^{-5}$	$5.6{\cdot}10^{-5}$	$3.2{\cdot}10^{-5}$
s	0.79	0.66	0.80	0.85	0.78	0.75
$\sigma_0(\Omega^{-1}\,cm^{-1})$	$5.0{\cdot}10^{-10}$	$1.8{\cdot}10^{-9}$	$1.1{\cdot}10^{-10}$	$5.6{\cdot}10^{-10}$	$2.5{\cdot}10^{-10}$	$7.2{\cdot}10^{-10}$
$\sigma_{DC}(\Omega^{-1}\,cm^{-1})$	$6.1{\cdot}10^{-9}$	$7.6{\cdot}10^{-9}$	$3.6{\cdot}10^{-9}$	$1.3{\cdot}10^{-8}$	$7.7{\cdot}10^{-10}$	$5.7{\cdot}10^{-10}$

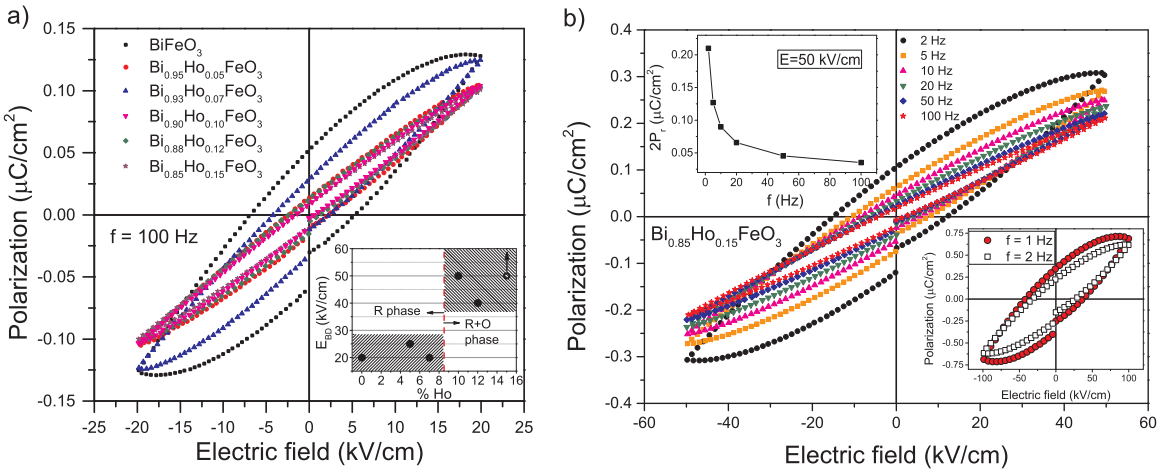

Fig. 5. a) Room-temperature P-E loops of $Bi_{1-x}Ho_xFeO_3$ samples. Inset presents breakdown fields for all samples except for BHFO15. b) P-E loops of BHFO15 sample taken at different frequencies. The frequency dependence of $2P_r$ is shown in the top-left corner inset, and the P-E loops in the field of large amplitude at low frequencies are shown in the bottom-right corner inset.

response and dc and ac conductivity contributions. It was shown that not only dc conductivity, but also grain boundary and interfacial effects were much reduced in biphasic $Bi_{1-x}Ho_xFeO_3$ ($x > 0.1$) samples. The dominant presence of orthorhombic phase in $Bi_{0.85}Ho_{0.15}FeO_3$ sample has stabilized the perovskite structure of BFO, significantly increased the breakdown field and improved BFO electrical performances. In high external electric fields (50 kV/cm and 100 kV/cm), P-E loops of $Bi_{0.85}Ho_{0.15}FeO_3$ sample manifested strong frequency dependence and abrupt increase of remnant polarization and coercive field at low frequencies. It was proposed that defect dipoles were oriented along the direction of spontaneous polarization, following the domain switching, and were therefore a primary cause of the enhanced polarization properties of $Bi_{0.85}Ho_{0.15}FeO_3$ sample. Although it is well established opinion that appearance of orthorhombic paraelectric phase degrades ferroelectricity of BFO, our study contributes to better understanding of polarization mechanisms in biphasic bismuth ferrite.

Acknowledgments

This work was financially supported by the Ministry of Education, Science and Technological Development of the Republic of Serbia under the projects ON171032 and III45018.

References

[1] G. Catalan, J.F. Scott, Physics and applications of bismuth ferrite, Adv. Mater. 21 (2009) 2463–2485.
[2] R. Ramesh, N.A. Spaldin, Multiferroics: progress and prospects in thin films, Nat. Mater. 6 (2007) 21–29.
[3] S.K. Pradhan, B.K. Roul, Effect of Gd doping on structural, electrical and magnetic properties of $BiFeO_3$ electroceramic, J. Phys. Chem. Solids 72 (2011) 1180–1187.
[4] G.L. Yuan, Siu Wing Or, J.M. Liu, Z.G. Liu, Structural transformation and ferroelectromagnetic behavior in single-phase $Bi_{1-x}Nd_xFeO_3$ multiferroic ceramics, Appl. Phys. Lett. 89 (2006) 052905.
[5] G.L. Yuan, S.W. Or, H.L.W. Chan, Reduced ferroelectric coercivity in multiferroic $Bi_{0.825}Nd_{0.175}FeO_3$ thin film, J. Appl. Phys. 101 (2007) 024106.
[6] J. Liu, M. Li, L. Pei, J. Wang, B. Yu, X. Wang, X. Zhao, Structural and multiferroic properties of the Ce-doped $BiFeO_3$ thin films, J. Alloy. Compd. 493 (2010) 544–548.
[7] K.S. Nalwa, A. Gart, A. Upadhyaya, Effect of samarium doping on the properties of solid-state synthesized multiferroic bismuth ferrite, Mater. Lett. 62 (2008) 878–881.
[8] W. Sun, J.F. Li, Q. Yu, L.Q. Cheng, Phase transition and piezoelectricity of sol-gel-processed Sm-doped $BiFeO_3$ thin films on $Pt(111)/Ti/SiO_2/Si$ substrates, J. Mater. Chem. C 3 (2015) 2115–2122.
[9] D. Varshney, P. Sharma, S. Satapathy, P.K. Gupta, Structural, magnetic and dielectric properties of Pr-modified $BiFeO_3$ multiferroic, J. Alloy. Compd. 584 (2014) 232–239.
[10] Y. Wang, C.W. Nan, Effect of Tb doping on electric and magnetic behavior of $BiFeO_3$ thin films, J. Appl. Phys. 103 (2008) 024103.
[11] S. Chatuvedi, R. Bag, V. Sathe, S. Kulkarni, S. Singh, Holmium induced enhanced functionality at room temperature and structural phase transition at high temperature in bismuth ferrite nanoparticles, J. Mater. Chem. C 4 (2016) 780–792.
[12] P. Suresh, P.D. Babu, S. Srinath, Effect of Ho substitution on structure and magnetic properties of $BiFeO_3$, J. Appl. Phys. 115 (2014) 17D905.
[13] S.K. Pradhan, B.K. Roul, D.R. Sahu, Enhancement of ferromagnetism and multiferroicity in Ho doped Fe rich $BiFeO_3$, Solid State Commun. 152 (2012) 1176–1180.
[14] S.K. Pradhan, J. Das, P.P. Rout, V.R. Mohanta, S.K. Das, S. Samantray, D.R. Sahu, J.L. Huang, S. Verma, B.K. Roul, Effect of holmium substitution for the improvement of multiferroic properties of $BiFeO_3$, J. Phys. Chem. Solids 71 (2010) 1557–1564.
[15] N. Jeon, D. Rout, W. Kim, S.-J.L. Kang, Enhanced multiferroic properties of single-phase $BiFeO_3$ bulk ceramics by Ho doping, Appl. Phys. Lett. 98 (2011) 072901.
[16] H. Singh, K.L. Yadav, Enhanced magnetization with unusual low temperature magnetic ordering behaviour and spin reorientation in holmium-modified multiferroic $BiFeO_3$ perovskite ceramics, J. Phys. D: Appl. Phys. 48 (2015) 205001.
[17] Y. Wu, J. Zhang, X.-K. Chen, X.-J. Chen, Phase evolution and magnetic property of $Bi_{1-x}Ho_xFeO_3$ powders, Solid State Commun. 151 (2011) 1936–1940.
[18] Z.L. Hou, H.F. Zhou, L.B. Kong, H.B. Jin, X. Qi, M.S. Cao, Enhanced ferromagnetism and microwave absorption properties of $BiFeO_3$ nanocrystals with Ho substitution, Mater. Lett. 84 (2012) 110–113.
[19] Y.Q. Liu, Y.J. Wang, J. Zhang, M. Gao, Y.J. Zhang, M.B. Wei, J.H. Yang, Effect of Ho substitution on structure and magnetic property of $BiFeO_3$ prepared by solgel method, Mater. Sci. Semicond. Proc. 40 (2015) 787–795.
[20] G.L. Song, G.J. Ma, J. Su, T.X. Wang, H.Y. Yang, F.G. Chang, Effect of Ho^{3+} doping on the electric, dielectric, ferromagnetic properties and TC of $BiFeO_3$ ceramics, Ceram. Int. 40 (2014) 3579–3587.
[21] W. Kraus, G. Nolze, POWDER CELL – a program for the representation and manipulation of crystal structures and calculation of the resulting X-ray powder patterns, J. Appl. Cryst. 29 (1996) 301.
[22] L. Chen, L. Zheng, Y. He, J. Zhang, Z. Mao, X. Chen, The local distortion and electronic behavior in Mn doped $BiFeO_3$, J. Alloy. Compd. 633 (2015) 216–219.
[23] V. Singh, S. Sharma, M. Kumar, R.K. Kotnala, R.K. Dwivedi, Structural transition, magnetic and optical properties of Pr and Ti co-doped $BiFeO_3$ ceramics, J. Magn. Magn. Mater. 349 (2014) 264–267.
[24] P.C. Sati, M. Arora, S. Chauhan, M. Kumar, S. Chhoker, Structural, magnetic, vibrational and impedance properties of Pr and Ti codoped BiFeO3 multiferroic ceramics, Creram. Int. 40 (2014) 7805–7816.
[25] B. Stojadinović, Z. Dohčević-Mitrović, N. Paunović, N. Ilić, N. Tasić, I. Petronijević, D. Popović, B. Stojanović, Comparative study of structural and electrical properties of Pr and Ce doped $BiFeO_3$ ceramics synthesized by auto-combustion method, J. Alloy. Compd. 657 (2016) 866–872.
[26] V.A. Khomchenko, D.V. Karpinsky, A.L. Kholkin, N.A. Sobolev, G.N. Kakazei, J.P. Araujo, I.O. Troyanchuk, B.F.O. Costa, J.A. Paixão, Rhombohedral-to-orthorhombic transition and multiferroic properties of Dy-substituted $BiFeO_3$, J. Appl. Phys. 108 (2010) 074109.
[27] P.C. Sati, M. Kumar, S. Chhoker, M. Jewariya, Inuence of Eu substitution on structural, magnetic, optical and dielectric properties of $BiFeO_3$ multiferroic ceramics, Creram. Int. 41 (2015) 2389–2398.
[28] P. Pandit, S. Satapathy, P. Sharma, P.K. Gupta, S.M. Yusuf, V.G. Sathe, Structural, dielectric and multiferroic properties of Er and La substituted $BiFeO_3$ ceramics, B, Mater. Sci. 34 (2011) 899–905.
[29] I. Levin, M.G. Tucker, H. Wu, V. Provenzano, C.L. Dennis, S. Karimi, T. Comyn, T. Stevenson, R.I. Smith, I.M., Reaney displacive phase transitions and magnetic structures in Nd-substituted $BiFeO_3$, Chem. Mater. 23 (2011) 2166–2175.
[30] X. Xue, G. Tan, W. Liu, H. Ren, Comparative study on multiferroic $(Bi_{0.9}RE_{0.1})(Fe_{0.97}Co_{0.03})O_{3-\delta}$ (RE = Ce and Ho) thin films: structural, electrical and optical properties, Creram. Int. 40 (2014) 6247–6254.
[31] P. Hermet, M. Goffinet, J. Kreisel, P. Ghosez, Raman and infrared spectra of multiferroic bismuth ferrite from frst principles, Phys. Rev. B 75 (2007) 220102.
[32] M. Iliev, M. Abrashev, H.G. Lee, V. Popov, Y. Sun, C. Thomsen, R. Meng, C. Chu,

Raman spectroscopy of orthorhombic perovskitelike $YMnO_3$ and $LaMnO_3$, Phys. Rev. B 57 (1998) 2872–2877.
[33] Y.W. Li, Z.G. Hu, F.Y. Yue, P.X. Yang, Y.N. Qian, W.J. Cheng, X.M. Ma, J.H. Chu, Oxygen-vacancy-related dielectric relaxation in $BiFeO_3$ films grown by pulsed laser deposition, J. Phys. D: Appl. Phys. 41 (2008) 215403.
[34] P. Lunkenheimer, V. Bobnar, A.V. Pronin, A.I. Ritus, A.A. Volkov, A. Loidl, Origin of apparent colossal dielectric constants, Phys. Rev. B 66 (2002) 052105.
[35] A.K. Jonscher, The universal dielectric response, Nature 267 (1977) 673–679.
[36] Q. Yun, Y. Bai, J. Chen, W. Gao, A. Bai, S. Zhao, Improved ferroelectric and fatigue properties in Ho doped $BiFeO_3$ thin films, Mater. Lett. 129 (2014) 166–169.
[37] E. Markiewicz, B. Hilczer, M. Blaszyk, A. Pietraszko, E. Talik, Dielectric properties of $BiFeO_3$ ceramics obtained from mechanochemically synthesized nanopowders, J. Electroceram. 27 (2011) 154–161.
[38] Q. Ke, X. Lou, Y. Wang, J. Wang, Oxygen-vacancy-related relaxation and scaling behaviors of $Bi_{0.9}La_{0.1}Fe_{0.98}Mg_{0.02}O_3$ ferroelectric thin films, Phys. Rev. B 82 (2010) 024102.
[39] S. Mukherjee, R. Gupta, A. Garg, V. Bansal, S. Bhargava, Inuence of Zr doping on the structure and ferroelectric properties of $BiFeO_3$ thin films, J. Appl. Phys. 107 (2010) 123535.
[40] B. Li, G. Li, Q. Yin, Z. Zhu, A. Ding, W. Cao, Pinning and depinning mechanism of defect dipoles in PMnNPZT ceramics, J. Phys. D: Appl. Phys. 38 (2005) 1107–1111.
[41] I. Bretos, R. Jiménez, C. Gutiérrez-Lázaro, I. Montero, L. Calzada, Defect-mediated ferroelectric domain depinning of polycrystalline $BiFeO_3$ multiferroic thin films, Appl. Phys. A 104 (2014) 092905.
[42] D. Guo, C. Wang, Q. Shen, L. Zhang, M. Li, J. Liu, Effect of measuring factors on ferroelectric properties of $Bi_{3.15}Nd_{0.85}Ti_3O_{12}$ thin films prepared by solgel method for non-volatile memory, Appl. Phys. A 97 (2009) 877–881.
[43] J. Lv, X. Lou, J. Wu, Defect dipole-induced poling characteristics and ferroelectricity of quenched bismuth ferrite-based ceramics, J. Mater. Chem. C 4 (2016) 6140–6151.
[44] L. Zhang, E. Erdem, X. Ren, R.-A. Eichel, Reorientation of $(Mn''_{Ti}\text{-}V_O^{\bullet\bullet})$X defect dipoles in acceptormodified BaTiO3 single crystals: an electron paramagnetic resonance study, Appl. Phys. Lett. 93 (2008) 202901.
[45] Y. Chrishima, Y. Noguchi, Y. Kitanaka, M. Miyayama, Defect control for polarization switching in $BiFeO_3$ single crystals, IEEE Trans. Ultrason. Ferroelectr. Freq. Control 57 (2010) 2233–2236.

PHYSICAL REVIEW B **94**, 241301(R) (2016)

Coherent manipulation of single electron spins with Landau-Zener sweeps

Marko J. Rančić*
Department of Physics, University of Konstanz, D-78457 Konstanz, Germany

Dimitrije Stepanenko†
Institute of Physics Belgrade, University of Belgrade, Pregrevica 118, 11080 Belgrade, Serbia

(Received 23 August 2016; revised manuscript received 3 November 2016; published 12 December 2016)

We propose a method to manipulate the state of a single electron spin in a semiconductor quantum dot (QD). The manipulation is achieved by tunnel coupling a QD, labeled L, and occupied with an electron to an adjacent QD, labeled R, which is not occupied by an electron but having an energy linearly varying in time. We identify a parameter regime in which a complete population transfer between the spin eigenstates $|L\uparrow\rangle$ and $|L\downarrow\rangle$ is achieved without occupying the adjacent QD. This method is convenient due to the fact that manipulation can be done electrically, without precise knowledge of the spin resonance condition, and is robust against Zeeman level broadening caused by nuclear spins.

DOI: 10.1103/PhysRevB.94.241301

Introduction. The initialization, manipulation, and readout of single electron spins in an efficient way are necessary for the implementation of single electron spin qubits [1]. Spin-orbit interactions and stray magnetic fields of micromagnets provide a necessary toolkit to control the single electron spin [2–7]. In electric dipole spin resonance (EDSR), microwaves drive an electron to oscillate in the spin-orbit field and/or the magnetic field gradient, producing a coherent spin rotation.

The Landau-Zener-Stückelberg-Majorana (LZSM) model [8–11] is one of the few analytically solvable time-dependent problems in quantum mechanics. It has found applications modeling nanoelectromechanical systems [12], optomechanical systems [13], Bose liquids [14], molecular magnets [15], Rydberg atoms [16], superconducting qubits [12,17–20], and semiconductor singlet-triplet qubits [21–23]. In the LZSM model the energy difference between two coupled states is varied linearly in time, while the coupling between the states is time independent. This results in a transition between the states with the probability determined by the coupling constant and the rate of the sweep.

Unlike the two-level LZSM problem, multilevel LZSM problems are not exactly analytically solvable for a general case [24–30]. Chirped Raman adiabatic passage (CHIRAP) [31,32,32–34] and similar techniques [35–41] allow for the efficient transfer of populations between two uncoupled levels. In order to utilize CHIRAP, the energy of the radiatively decaying state is varied linearly in time with laser pulses having chirped frequencies.

Equivalently to CHIRAP, the goal of our scheme is to transfer the population between two uncoupled levels $|L\uparrow\rangle$ and $|L\downarrow\rangle$ by coupling the levels of the L electrostatically defined quantum dot (QD) in a time-independent manner to an adjacent electrostatically defined quantum dot, whose energy is linearly varying in time [42]. It should be noted that, as the probability to occupy the adjacent quantum dot R remains negligible in this scheme, the states in the R QD can be extremely susceptible to relaxation without influencing the efficiency of our scheme. The scheme under study is also applicable to coupled donors [43] and coupled donor-dot systems [44].

We discuss two possible realizations of our scheme. In the first realization the R quantum dot has significantly larger Zeeman splitting than the L quantum dot. Then, the scheme operates even in the case when the rate of non-spin-conserving tunneling events is significantly smaller than the rate of spin-conserving events. This regime is often present in GaAs double quantum dots. In the second realization the Zeeman splittings of the left L and right R quantum dots are comparable in magnitude but the rates of spin-conserving and non-spin-conserving tunneling events must be comparable. This regime can be reached for electrons in InAs double quantum dots and holes in GaAs double quantum dots.

The Hamiltonian. We model a situation where the electron spin is localized in the L quantum dot. The energy of the R quantum dot is varied linearly in time (Fig. 1),

$$H(t) = \sum_{c}\sum_{\sigma} E_{c,\sigma}(t)|c\sigma\rangle\langle c\sigma| + \tau\sum_{\sigma}\sum_{c\neq\bar{c}}|c\sigma\rangle\langle\bar{c}\sigma| + \tau_{\Delta}\sum_{\sigma\neq\bar{\sigma}}\sum_{c\neq\bar{c}}|c\sigma\rangle\langle\bar{c}\bar{\sigma}|. \quad (1)$$

The sum over the charge states runs over the left and the right quantum dots, $c = L, R$, and the sum over spin states runs over spin-up and spin-down states $\sigma = \uparrow, \downarrow$. Furthermore, $E_{c\sigma}$ represents the energy with charge state c and spin state σ. The energies of the L quantum dot are time independent, $E_{L\uparrow} = \Delta E_L/2$, $E_{L\downarrow} = -\Delta E_L/2$, where ΔE_L is the Zeeman splitting in the left quantum dot. The energies of the R quantum dot are time dependent with a linear time dependence, $E_{R\uparrow} = \Delta E_R + \beta t$, and $E_{R\downarrow} = \beta t$, where ΔE_R is the Zeeman splitting in the right quantum dot, t is time, and β the Landau-Zener velocity (see Fig. 1).

The off-diagonal terms in the Hamiltonian are the spin-conserving tunneling amplitude τ, and the non-spin-conserving tunneling amplitude τ_{Δ}. The non-spin-conserving tunneling can appear due to spin-orbit interaction or be induced by the stray field of the micromagnet, which is inhomogeneous in the tunneling direction [45,46].

*marko.rancic@uni-konstanz.de
†dimitrije.stepanenko@ipb.ac.rs

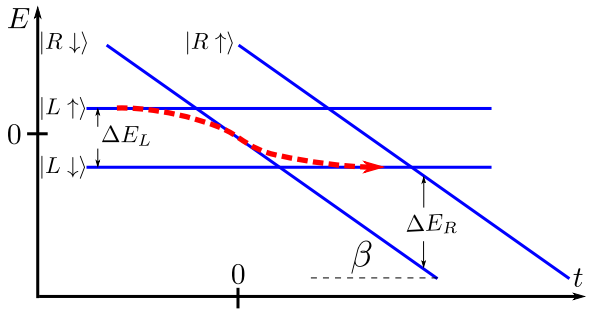

FIG. 1. The energy diagram. We initialize the electron in the $|L\uparrow\rangle$ state, with the R quantum dot being higher in energy. We ramp the energies of the states in R quantum dot with a Landau-Zener velocity β. In the figure, $\beta < 0$. The goal of our scheme is to find a parameter regime in which the adiabatic evolution path is followed (red dashed arrow). The Zeeman splittings of the L and R quantum dots are marked as ΔE_L and ΔE_R, respectively.

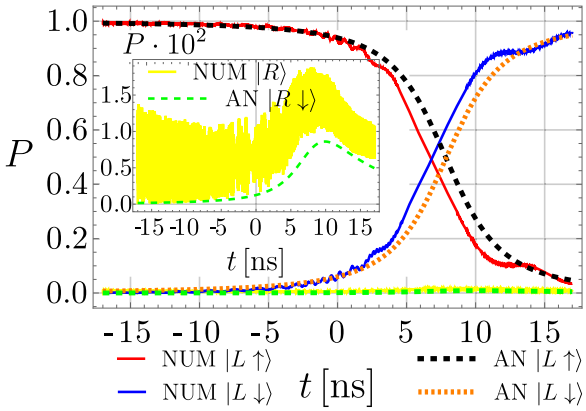

FIG. 2. The comparison between the numerically computed probabilities [obtained from evolving the state using the Hamiltonian of Eq. (1)] (Num) and analytic adiabatic three-level probabilities Eq. (2) (An). The parameters of the plot are the Landau-Zener velocity $\beta = 5 \times 10^3$ eV/s, the tunnel coupling $\tau = 6.5$ μeV, corresponding to an interdot separation of $l = 179$ nm (for more information, see the Supplemental Material [47]), the non-spin-conserving tunnel coupling $\tau_\Delta = 0.25\tau$, the external magnetic field Zeeman splitting in the left QD $\Delta E_L = 1$ μeV, and Zeeman splitting in the right quantum dot $\Delta E_R = 200\Delta E_L$. The inset represents the magnification of the occupation probabilities of the states in the R quantum dot.

Different Zeeman splittings. We initialize the system in the $|L\uparrow\rangle$ state, at a negative instance of time $-T/2$. If the product of the Landau-Zener velocity β and the total duration of the Landau-Zener sweep T is smaller than the Zeeman splitting of the right quantum dot $\Delta E_R > \beta T$, and if the R quantum dot is initially positively detuned with respect to the L quantum dot, our system behaves as an effective three-level system. Furthermore, if the evolution of the system is adiabatic ($\tau^2, \tau_\Delta^2 \gg \beta\hbar$), the system will remain in the instantaneous eigenstate of the Hamiltonian for the entire duration of the Landau-Zener sweep T. Given all these assumptions, we can calculate the adiabatic eigenvectors, and therefore the time evolution of our three state probabilities,

$$P_{L\uparrow} = \tau_\Delta^2 \frac{|\lambda(t) + \Delta E_L/2|^2}{N(t)^2}, \quad P_{L\downarrow} = \tau^2 \frac{|\lambda(t) - \Delta E_L/2|^2}{N(t)^2},$$
$$P_{R\downarrow} = \frac{\left|\lambda(t)^2 - \Delta E_L^2/4\right|^2}{N(t)^2}, \tag{2}$$

where $\lambda(t)$ is the appropriate adiabatic eigenvalue [see the Supplemental Material [47] for the expression for $\lambda(t)$] and $N(t)$ is the normalization of the adiabatic eigenvectors. For simplicity, we have omitted to explicitly state that $\lambda(t)$ is also a function of ΔE_L, β, τ, τ_Δ. Depending on the values of τ and τ_Δ, $\lambda(t) = 0$ close to $t = 0$ (for $\tau = \tau_\Delta$), $\lambda(t) = 0$ at $t > 0$ (for $\tau > \tau_\Delta$), and $\lambda(t) = 0$ at $t < 0$ (for $\tau < \tau_\Delta$). Furthermore, the adiabatic eigenvalue takes the following values, $\lambda(t = \mp\infty) = \pm\Delta E_L/2$, $-\Delta E_L/2 \leqslant \lambda(t) \leqslant \Delta E_L/2$, for every t. Therefore, the maximal possible occupation probabilities are $P_{L\uparrow}^{\max} \sim \tau_\Delta^2 \Delta E_L^2$, $P_{R\downarrow}^{\max} \sim \Delta E_L^4$, $P_{L\downarrow}^{\max} \sim \tau^2 \Delta E_L^2$. If $\tau, \tau_\Delta \gg \Delta E_L$, no significant population will occupy the R quantum dot, $P_R \approx 0$ at every instance of time (see Fig. 2), and a complete population transfer between the spin eigenstates $|L\uparrow\rangle$ and $|L\downarrow\rangle$ occurs.

In contrast to EDSR techniques, our scheme does not require precise knowledge of the spin resonance condition ΔE_L and operates without microwaves. However, in order for our scheme to be successful, a necessary requirement is that the quantum dots have significantly different Zeeman splittings $\Delta E_L \ll \Delta E_R$. For a typical double quantum dot system where the distance between the quantum dots is ∼200 nm, the required gradient would be $dB_z/dx \sim 10$ T/μm, which is for a factor of 10 larger than the currently maximally achieved experimental value [6,48]. A possible way to induce a large enough difference of Zeeman energies between quantum dots is to engineer the g factor of one of the quantum dots L to be almost zero, and engineer the g factor of the R QD to be significantly larger [49–52]. This could be achieved by locally inducing different content of Al in the GaAs mixture [50].

Equal Zeeman splittings. Again we initialize the system in the $|L\uparrow\rangle$ state, at a negative instance of time $-T/2$. Another way for our scheme to be successful is that the magnitude of spin-conserving and non-spin-conserving tunnelings are comparable, $\tau \approx \tau_\Delta$. The requirement for our scheme to work is $\tau/\tau_\Delta \sim 4l/3\Lambda_{SO} \approx 1$ can be fulfilled in InAs [53]. Here, l is the interdot separation and Λ_{SO} is the spin-orbit length, defined by [54,55] $\Lambda_{SO} = \hbar/m^*\sqrt{\cos\phi^2(\beta-\alpha)^2 + \sin\phi^2(\beta+\alpha)^2}$, for a two-dimensional electron gas (2DEG) in the (001) plane. Here, m^* is the effective electron mass, ϕ is the angle between the [110] crystallographic axis and the interdot connection axis, and β and α are Dresselhaus and Rashba spin-orbit constants, respectively. Possible ways of controlling the spin-orbit interaction is the variation of angle between the external magnetic field and the spin-orbit field [56], variation of the direction in which the double quantum dot (DQD) is grown [57] (and therefore maximizing $\cos\phi$), isotopic control of indium in InGaAs, or electric field control of the Rashba constant [58,59].

In the adiabatic limit ($\tau^2 = \tau_\Delta^2 \gg \beta\hbar$), the system will remain in the instantaneous eigenstate of the Hamiltonian for the entire duration of the Landau-Zener sweep T. In that limit, we can calculate the adiabatic eigenvectors, and therefore the

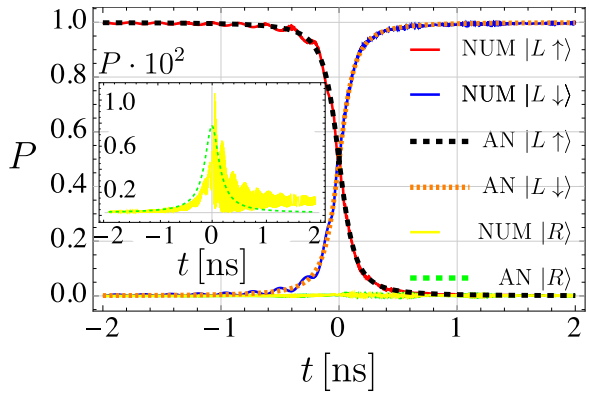

FIG. 3. Comparison between the numerically computed probabilities [obtained from evolving the state using the Hamiltonian of Eq. (1)] (Num) and analytic adiabatic four-level probabilities Eq. (3) (An). The inset represents the magnification of the probability to occupy the R quantum dot. The parameters of the plot are the Landau-Zener velocity $\beta = 4 \times 10^6$ eV/s, the tunnel hopping $\tau = 50$ μeV, corresponding to interdot distance of $l = 280$ nm for $m^* = 0.023 m_e$ (for more information, see the Supplemental Material [47]), the Zeeman energies $\Delta E_L = \Delta E_R = 17$ μeV.

time evolution of our four state probabilities,

$$P_{L\uparrow} = \tau^2 \frac{|\Lambda(t) + \Delta E_L/2|^2}{\tilde{N}(t)^2}, \quad P_{L\downarrow} = \tau^2 \frac{|\Lambda(t) - \Delta E_L/2|^2}{\tilde{N}(t)^2},$$
$$P_{R\downarrow} = P_{R\uparrow} = \frac{\left|\Lambda(t)^2 - \Delta E_L^2/4\right|^2}{2\tilde{N}(t)^2}, \tag{3}$$

where $\Lambda(t)$ is the corresponding adiabatic eigenvalue and $\tilde{N}(t)$ the wave-function normalization.

The requirement that spin-conserving and non-spin-conserving tunnel couplings are equal is due to the fact that when $\Delta E_L = \Delta E_R$, the adiabatic eigenfunctions have only a vanishing contribution of the two states of the R quantum dot when $\tau \approx \tau_\Delta$ is fulfilled. In the case of $\tau \gg \tau_\Delta$, the adiabatic eigenfunctions have only a small component in the $|R\downarrow\rangle$ state when $\Delta E_L \ll \tau, \tau_\Delta$, and the $|R\uparrow\rangle$ state is detuned during the duration of the Landau-Zener sweep T.

Similarly to the previous implementation of our scheme, the appropriate adiabatic eigenvalue spans between $\Lambda(t = \mp\infty) = \pm\Delta E_L/2, -\Delta E_L/2 \leqslant \Lambda(t) \leqslant \Delta E_L/2$, for every t, with $\Lambda(t) = 0$ for $t \approx 0$. The maximal possible occupations of states for the case $\Delta E_L = \Delta E_R$ are $P_{L\uparrow}^{\max} \sim \tau^2 \Delta E_L^2$, $P_{L\downarrow}^{\max} \sim \tau^2 \Delta E_L^2$, and $P_{R\uparrow}^{\max} = P_{R\downarrow}^{\max} \sim \Delta E_L^4/2$. Equivalently to CHIRAP, the probabilities to occupy the $|R\downarrow\rangle$ and $|R\uparrow\rangle$ states are negligible at all instances of time $P_R \approx 0$ in the case when $\tau \gg \Delta E_L$ (see Fig. 3), and a complete population transfer between the spin eigenstates $|L\uparrow\rangle$ and $|L\downarrow\rangle$ occurs.

Experimental realizations. Our control scheme works optimally when the Zeeman splitting of the L QD is small. Furthermore, different signs of the Landau-Zener velocity and initial detunings need to be used for different initial spin states. We will address the problem of initializing and measuring electron spin states when the Zeeman splitting in the L QD is small in the remaining part of this section.

If the thermal broadening of the lead is smaller than the Zeeman splitting of the electron spin states $k_B T_e \ll \Delta E_L$, the state of the spin qubit can be initialized by tuning the chemical potential of a nearby lead close to the $|\Downarrow\rangle$ state of the spin qubit. When lead-to-dot relaxation occurs, the only possible state to which the electron can relax from the lead is the $|\Downarrow\rangle$ state. Furthermore, single-shot measurement of the electron spin state can be achieved in a similar manner [60], by tuning the chemical potential of the lead in such a way so that only one of the states can tunnel out of the quantum dot to the lead.

As our scheme operates optimally in low magnetic fields $k_B T_e > \Delta E_L$, the initialization and readout, validating the efficiency of our scheme, must be done in an alternative way, via the R QD. The chemical potential of the lead coupled to the R QD can be tuned between the spin states of the R QD. After successful initialization of the $|R\downarrow\rangle$ state, the spin is shuttled to the $|L\downarrow\rangle$ state, followed by a manipulation of the spin according to our scheme.

After the manipulation stage, the modification in the current of a quantum point contact (QPC) near R is monitored. If the current of the QPC is unchanged, this means that the manipulation stage did not produce any leakage to the R quantum dot and that the spin measurement stage can follow. In the spin measurement stage, states $|L\downarrow\rangle$ and $|R\downarrow\rangle$ are aligned in energy one more time. If the electron spin was in the $|L\downarrow\rangle$ state, a tunneling event occurs and a nearby QPC modifies its current accordingly [61,62]. On the other hand, if the electron spin was in the $|L\uparrow\rangle$ state, the current of the QPC would remain unchanged.

In the case of $\Delta E_L = \Delta E_R$ (and therefore $\tau \approx \tau_\Delta$) and when $\Delta E_L < k_B T_e$, the initialization could still be achieved by waiting a sufficiently long time for the electron spin to relax to the thermal equilibrium state. However, spin readout would need to be done with alternative methods, because both spin eigenstates are energetically allowed to tunnel to the R QD when $|L\downarrow\rangle$ and $|R\downarrow\rangle$ are aligned in energy. This is why we consider the case $\Delta E_L \ll \Delta E_R$ to be more likely to implement in future experiments, and only consider the influence of nuclear spin noise for this realization.

Errors due to nuclear spins. We model the influence of nuclear spins as a distribution of the magnetic field in the L and R quantum dot, centered around the external magnetic field in the left and the right dot $\Delta E_L, \Delta E_R$, with standard deviations $\sigma = g_L \mu_B B_N$, $\chi = g_R \mu_B B_N$, where $g_{L(R)}$ is the electron g factor in the left (right) quantum dot, μ_B is the Bohr magneton, and B_N is the root mean square of the distribution of the nuclear magnetic field [63]. The influence of nuclear spins on our manipulation scheme can be estimated by averaging the probabilities of all relevant states over a distribution of nuclear spins,

$$\bar{P}_{c\sigma} = \iint_{-\infty}^{\infty} \frac{P_{c\sigma}}{2\pi\chi\sigma} e^{-\frac{(\Delta E - \Delta E_L)^2 + (\tilde{\beta}\tilde{t} - \beta t)^2}{4\sigma^2\chi^2}} d(\Delta E) d(\tilde{\beta}\tilde{t}), \tag{4}$$

where $c = L, R$, $\sigma = \uparrow, \downarrow$, with the exclusion of the detuned $|R\uparrow\rangle$ state.

In Fig. 4 we show how the nuclear spins influence our control scheme in the case of no uncertainty of the magnetic field in the right quantum dot, $\chi = 0$. If the random nuclear field is parallel with the external magnetic field, this gives rise

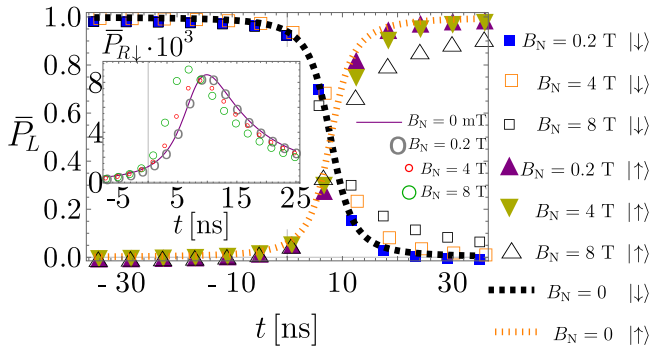

FIG. 4. Spin manipulation in the presence of nuclear spins. The parameters of the plot are the Landau-Zener velocity $\beta = 5 \times 10^3$ eV/s, the tunnel coupling $\tau = 6.5$ μeV, corresponding to an interdot separation of $l = 179$ nm (for more information, see the Supplemental Material [47]), the non-spin-conserving tunnel coupling $\tau_\Delta = 0.25\tau$, the Zeeman energy in the left quantum dot $\Delta E_L = 1$ μeV, the standard deviation in the right quantum dot $\chi = 0$, and the g factor in the left quantum dot $g_L = 1.2 \times 10^{-3}$. The inset represents occupation of the states in the R quantum dot.

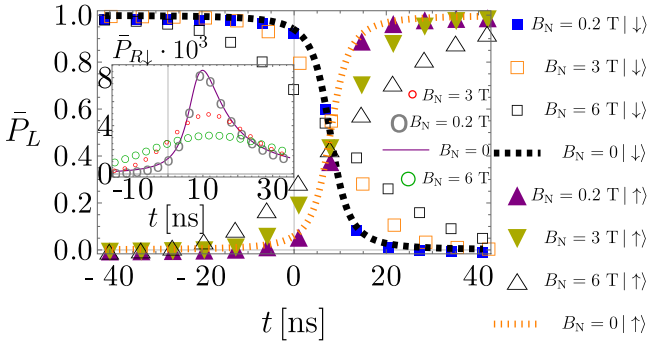

FIG. 5. Spin manipulation in the presence of nuclear spins. The parameters of the plot are the Landau-Zener velocity $\beta = 5 \times 10^3$ eV/s, the tunnel coupling $\tau = 6.5$ μeV, corresponding to an interdot separation of $l = 179$ nm (for more information, see the Supplemental Material [47]), the non-spin-conserving tunnel coupling $\tau_\Delta = 0.25\tau$, the Zeeman splitting in the left quantum dot $\Delta E_L = 1$ μeV, the g factor in the left quantum dot $g_L = 1.2 \times 10^{-3}$, and the g factor in the right quantum dot $g_R = 200 g_L$. The inset represents occupation of the states in the R quantum dot.

to more leakage into the $|R\downarrow\rangle$ state. However, if the random nuclear field is antiparallel with the external magnetic field, this gives rise to less leakage into the $|R\downarrow\rangle$ state, and these two effects (less and more leakage to $|R\rangle$) cancel first order in ΔE_L.

In Fig. 5 we present the behavior of our control scheme under an influence of random nuclear spins in both quantum dots. Other than the already mentioned mechanism of additional leakage, the uncertainties in the nuclear field in the right quantum dot (and therefore the position of the level $|R\downarrow\rangle$) lead to reduced maximal probability to occupy the $|R\downarrow\rangle$ state (Fig. 5, inset, dark gray versus green circles). In contrast to EDSR, we are able to achieve a full transfer of population between the spin eigenstates, even when the uncertainty in the energy difference between spin eigenstates is large (Fig. 5, black open squares and triangles).

An effective nuclear magnetic field of unknown intensity in the z direction is going to change the instance of time in which the energy of the state $|R\downarrow\rangle$ is located between the energies of the states $|L\uparrow\rangle$ and $|L\downarrow\rangle$. For a nuclear magnetic field parallel with the external field, the energy of the state $|R\downarrow\rangle$ is located between the energy of the states $|L\uparrow\rangle$ and $|L\downarrow\rangle$ at a time $t < 0$. In contrast to that, for a nuclear magnetic field antiparallel with the external field, the energy of the state $|R\downarrow\rangle$ is located between the energies of the states $|L\uparrow\rangle$ and $|L\downarrow\rangle$ at a time $t > 0$. A process such as this is described with a Gaussian distribution, centered around βt with a standard deviation $\chi = g_R \mu_B B_N$, where g_R is the g factor in the right quantum dot, $g_R \gg g_L$. This leads to a reduced maximal value of the occupation of the $|R\downarrow\rangle$ state, without changing the averaged occupation of the $|R\downarrow\rangle$ per unit time $\bar{\bar{P}}_{R\downarrow}(T) = \int_{-T/2}^{T/2} \bar{P}_{R\downarrow}(t) dt/T = \text{const}$ for a large enough T. Since the nuclear spins do not affect the final probabilities, our scheme can be operated in the presence of nuclear spin induced decoherence, as long as the total sweep time (in our case $\sim$80 ns) is shorter than the characteristic time of nuclear spin evolution (1 μs) [63]. It should be noted that quasistatic detuning noise yields the same effect as having an uncertain nuclear spin distribution in the R quantum dot, and therefore we do not address this issue separately in this Rapid Communication.

Conclusions and final remarks. To conclude, we have proposed a method to manipulate a single electron spin by using Landau-Zener sweeps. Our control method is robust against the uncertainties of the nuclear field and static charge noise, and operates without microwaves and without precise knowledge of the spin resonance condition.

Note added. In the process of preparing this Rapid Communication, we became aware of an article [42] implementing similar ideas for double quantum dot $S - T_+$ qubits.

Acknowledgments. We thank Marko Milivojević, Guido Burkard, Maximilian Russ, Alexander Pearce, and Ferdinand Kuemmeth for fruitful discussions. This work is funded from MPNTR Grant No. OI171032, DAAD Grant No. 451-03-01858201309-3, and European Union within the S^{3}nano initial training network.

[1] D. Loss and D. P. DiVincenzo, Phys. Rev. A **57**, 120 (1998).

[2] C. Flindt, A. S. Sørensen, and K. Flensberg, Phys. Rev. Lett. **97**, 240501 (2006).

[3] K. Nowack, F. Koppens, Y. V. Nazarov, and L. Vandersypen, Science **318**, 1430 (2007).

[4] S. Nadj-Perge, S. Frolov, E. Bakkers, and L. P. Kouwenhoven, Nature (London) **468**, 1084 (2010).

[5] Y. Tokura, W. G. van der Wiel, T. Obata, and S. Tarucha, Phys. Rev. Lett. **96**, 047202 (2006).

[6] M. Pioro-Ladriere, T. Obata, Y. Tokura, Y.-S. Shin, T. Kubo, K. Yoshida, T. Taniyama, and S. Tarucha, Nat. Phys. **4**, 776 (2008).

[7] E. Kawakami, P. Scarlino, D. Ward, F. Braakman, D. Savage, M. Lagally, M. Friesen, S. Coppersmith, M. Eriksson, and L. Vandersypen, Nat. Nanotechnol. **9**, 666 (2014).
[8] L. Landau, Phys. Z. Sowjetunion **2**, 46 (1932).
[9] C. Zener, Proc. R. Soc. London, Ser. A **137**, 696 (1932).
[10] E. C. G. Stueckelberg, Helv. Phys. Acta (Basel) **5**, 369 (1932).
[11] E. Majorana, Il Nuovo Cimento (1924-1942) **9**, 43 (1932).
[12] M. LaHaye, J. Suh, P. Echternach, K. C. Schwab, and M. L. Roukes, Nature (London) **459**, 960 (2009).
[13] G. Heinrich, J. G. E. Harris, and F. Marquardt, Phys. Rev. A **81**, 011801 (2010).
[14] Y.-A. Chen, S. D. Huber, S. Trotzky, I. Bloch, and E. Altman, Nat. Phys. **7**, 61 (2011).
[15] W. Wernsdorfer, R. Sessoli, A. Caneschi, D. Gatteschi, and A. Cornia, Europhys. Lett. **50**, 552 (2000).
[16] J. R. Rubbmark, M. M. Kash, M. G. Littman, and D. Kleppner, Phys. Rev. A **23**, 3107 (1981).
[17] W. D. Oliver, Y. Yu, J. C. Lee, K. K. Berggren, L. S. Levitov, and T. P. Orlando, Science **310**, 1653 (2005).
[18] M. Sillanpää, T. Lehtinen, A. Paila, Y. Makhlin, and P. Hakonen, Phys. Rev. Lett. **96**, 187002 (2006).
[19] C. M. Wilson, T. Duty, F. Persson, M. Sandberg, G. Johansson, and P. Delsing, Phys. Rev. Lett. **98**, 257003 (2007).
[20] A. Izmalkov, S. H. W. van der Ploeg, S. N. Shevchenko, M. Grajcar, E. Il'ichev, U. Hübner, A. N. Omelyanchouk, and H.-G. Meyer, Phys. Rev. Lett. **101**, 017003 (2008).
[21] J. R. Petta, A. C. Johnson, J. M. Taylor, E. A. Laird, A. Yacoby, M. D. Lukin, C. M. Marcus, M. P. Hanson, and A. C. Gossard, Science **309**, 2180 (2005).
[22] J. Petta, H. Lu, and A. Gossard, Science **327**, 669 (2010).
[23] H. Ribeiro and G. Burkard, Phys. Rev. Lett. **102**, 216802 (2009).
[24] Y. N. Demkov and V. Osherov, JETP **26**, 916 (1968).
[25] C. Carroll and F. Hioe, J. Phys. A: Math. Gen. **19**, 2061 (1986).
[26] Y. Kayanuma and S. Fukuchi, J. Phys. B: At. Mol. Phys. **18**, 4089 (1985).
[27] V. L. Pokrovsky and N. A. Sinitsyn, Phys. Rev. B **65**, 153105 (2002).
[28] Y. N. Demkov and V. Ostrovsky, J. Phys. B **34**, 2419 (2001).
[29] B. Damski, Phys. Rev. Lett. **95**, 035701 (2005).
[30] A. A. Rangelov, J. Piilo, and N. V. Vitanov, Phys. Rev. A **72**, 053404 (2005).
[31] J. Oreg, F. T. Hioe, and J. H. Eberly, Phys. Rev. A **29**, 690 (1984).
[32] B. Broers, H. B. van Linden van den Heuvell, and L. D. Noordam, Phys. Rev. Lett. **69**, 2062 (1992).
[33] S. Chelkowski and G. N. Gibson, Phys. Rev. A **52**, R3417 (1995).
[34] B. W. Shore, Acta Phys. Slovaca **63**, 361 (2013).
[35] U. Gaubatz, P. Rudecki, S. Schiemann, and K. Bergmann, J. Chem. Phys. **92**, 5363 (1990).
[36] N. V. Vitanov, T. Halfmann, B. W. Shore, and K. Bergmann, Annu. Rev. Phys. Chem. **52**, 763 (2001).
[37] B. W. Shore, K. Bergmann, A. Kuhn, S. Schiemann, J. Oreg, and J. H. Eberly, Phys. Rev. A **45**, 5297 (1992).
[38] D. A. Golter and H. Wang, Phys. Rev. Lett. **112**, 116403 (2014).
[39] K. S. Kumar, A. Vepsäläinen, S. Danilin, and G. S. Paraoanu, Nat. Commun. **7**, 10628 (2016).
[40] K. Bergmann, N. V. Vitanov, and B. W. Shore, J. Chem. Phys. **142**, 170901 (2015).
[41] K. Bergmann, H. Theuer, and B. W. Shore, Rev. Mod. Phys. **70**, 1003 (1998).
[42] J. Stehlik, M. Z. Maialle, M. H. Degani, and J. R. Petta, Phys. Rev. B **94**, 075307 (2016).
[43] R. Kalra, A. Laucht, C. D. Hill, and A. Morello, Phys. Rev. X **4**, 021044 (2014).
[44] P. Harvey-Collard, N. T. Jacobson, M. Rudolph, J. Dominguez, G. A. T. Eyck, J. R. Wendt, T. Pluym, J. K. Gamble, M. P. Lilly, M. Pioro-Ladrière, and M. S. Carroll, arXiv:1512.01606.
[45] V. F. Maisi, A. Hofmann, M. Röösli, J. Basset, C. Reichl, W. Wegscheider, T. Ihn, and K. Ensslin, Phys. Rev. Lett. **116**, 136803 (2016).
[46] F. R. Braakman, J. Danon, L. R. Schreiber, W. Wegscheider, and L. M. K. Vandersypen, Phys. Rev. B **89**, 075417 (2014).
[47] See Supplemental Material at http://link.aps.org/supplemental/10.1103/PhysRevB.94.241301 for adiabatic eigenfunctions and eigenvectors that are derived along with expressions for tunneling matrix elements.
[48] T. Obata, M. Pioro-Ladrière, Y. Tokura, Y.-S. Shin, T. Kubo, K. Yoshida, T. Taniyama, and S. Tarucha, Phys. Rev. B **81**, 085317 (2010).
[49] M. D. Schroer, K. D. Petersson, M. Jung, and J. R. Petta, Phys. Rev. Lett. **107**, 176811 (2011).
[50] G. Salis, Y. Kato, K. Ensslin, D. Driscoll, A. Gossard, and D. Awschalom, Nature (London) **414**, 619 (2001).
[51] H. W. Jiang and E. Yablonovitch, Phys. Rev. B **64**, 041307 (2001).
[52] J. H. Prechtel, F. Maier, J. Houel, A. V. Kuhlmann, A. Ludwig, A. D. Wieck, D. Loss, and R. J. Warburton, Phys. Rev. B **91**, 165304 (2015).
[53] A. E. Hansen, M. T. Björk, C. Fasth, C. Thelander, and L. Samuelson, Phys. Rev. B **71**, 205328 (2005).
[54] V. N. Golovach, A. Khaetskii, and D. Loss, Phys. Rev. Lett. **93**, 016601 (2004).
[55] D. Stepanenko, M. Rudner, B. I. Halperin, and D. Loss, Phys. Rev. B **85**, 075416 (2012).
[56] J. M. Nichol, S. P. Harvey, M. D. Shulman, A. Pal, V. Umansky, E. I. Rashba, B. I. Halperin, and A. Yacoby, Nat. Commun. **6**, 7682 (2015).
[57] M. J. Rančić and G. Burkard, Phys. Rev. B **90**, 245305 (2014).
[58] J. Nitta, T. Akazaki, H. Takayanagi, and T. Enoki, Phys. Rev. Lett. **78**, 1335 (1997).
[59] D. Liang and X. P. Gao, Nano Lett. **12**, 3263 (2012).
[60] J. Elzerman, R. Hanson, L. W. Van Beveren, B. Witkamp, L. Vandersypen, and L. P. Kouwenhoven, Nature (London) **430**, 431 (2004).
[61] S. D. Barrett and T. M. Stace, Phys. Rev. Lett. **96**, 017405 (2006).
[62] Y.-S. Shin, T. Obata, Y. Tokura, M. Pioro-Ladrière, R. Brunner, T. Kubo, K. Yoshida, and S. Tarucha, Phys. Rev. Lett. **104**, 046802 (2010).
[63] I. A. Merkulov, A. L. Efros, and M. Rosen, Phys. Rev. B **65**, 205309 (2002).

PAPER

Field-dependent superradiant quantum phase transition of molecular magnets in microwave cavities

IOP Publishing Semiconductor Science and Technology
Semicond. Sci. Technol. 31 (2016) 094003 (7pp) doi:10.1088/0268-1242/31/9/094003

Field-dependent superradiant quantum phase transition of molecular magnets in microwave cavities

Dimitrije Stepanenko[1], Mircea Trif[2], Oleksandr Tsyplyatyev[3,4] and Daniel Loss[5]

[1] Institute of Physics Belgrade, University of Belgrade, Pregrevica 118, 11080 Belgrade, Serbia
[2] Laboratoire de Physique des Solides, CNRS UMR-8502, Université Paris Sud, F-91405 Orsay Cedex, France
[3] School of Physics and Astronomy, The University of Birmingham, Birmingham, B15 2TT, UK
[4] Institut für Theoretische Physik, Universität Frankfurt, Max-von-Laue Strasse 1, D-60438 Frankfurt, Germany
[5] Department of Physics, University of Basel, Klingelbergstrasse 82, CH-4056 Basel, Switzerland

E-mail: Dimitrije.Stepanenko@ipb.ac.rs

Received 11 May 2016, revised 16 June 2016
Accepted for publication 12 July 2016
Published 25 August 2016

Abstract

We study a superradiant quantum phase transition in the model of triangular molecular magnets coupled to the electric component of a microwave cavity field. The transition occurs when the coupling strength exceeds a critical value, d_c, which, in sharp contrast to the standard two-level emitters, can be tuned by an external magnetic field. In addition to emitted radiation, the molecules develop an in-plane electric dipole moment at the transition. We estimate that the transition can be detected in state-of-the-art microwave cavities if their electric field couples to a crystal containing a sufficient number of oriented molecules.

Keywords: molecular magnets, quantum optics, quantum computing

(Some figures may appear in colour only in the online journal)

1. Introduction

The superradiant phase of a collection of emitters coupled to common electromagnetic field mode is characterized by a finite number of photons in the ground state of the combined system. In the model of two-level emitters coupled to a single cavity mode [1–4], the superradiant phase appears when the emitter-field coupling g exceeds some critical value g_c [5, 6]. Theoretical and experimental search for the superradiant phase transition has included atoms and molecules coupled to single- and multimode optical cavities, Josephson junction qubits in microwave resonators, as well as ultracold atoms in optical traps [7–11].

According to the no-go theorem [12–14], the ground state of any collection of two-level emitters with dipolar coupling to a mode of electromagnetic field does not contain cavity photons. This result seems to render the superradiant quantum phase transition impossible, and it was extended to the case of many electromagnetic field modes and many levels in Josephson junctions [13, 14]. However, the superradiant phase transition was predicted to occur in the interacting emitters as well as in an ensemble of inhomogeneously coupled emitters and many modes [7, 15]. It was indeed observed in ultracold gases [9]. Here, we consider emission from an ensemble of interacting spins, and we are not aware of any extension of the no-go theorem that applies to our case.

Two-level emitters interacting with the quantized electromagnetic field of resonant cavity are described by the standard Dicke, Jaynes–Cummings, and Tavis–Cummings models of quantum optics [2]. Motivated by the spin-electric coupling of molecular magnets [16], we introduce a new model for the emitter in a cavity. The emitter degree of freedom represents the chirality of ground-state spin texture in a triangular molecular magnet, which interacts with the molecule's total spin. A crystal with oriented molecular

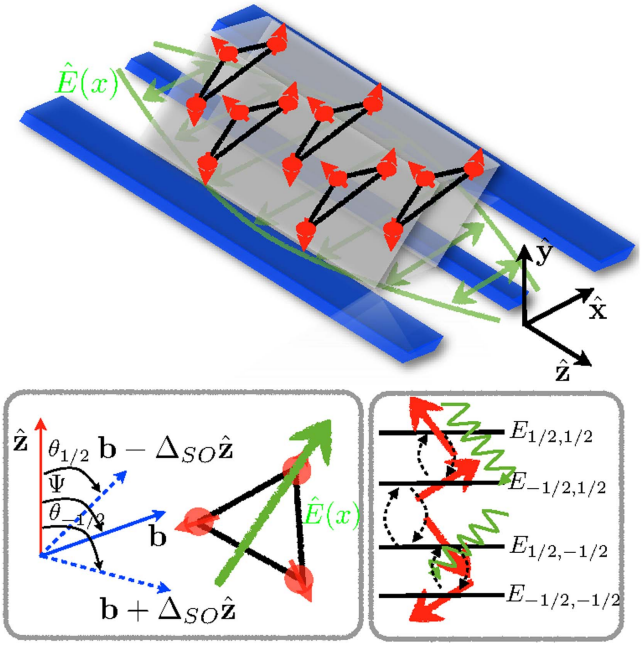

Figure 1. Geometry of a crystal of molecular magnets in a microwave cavity and external magnetic field. Electric field of the cavity mode is in the plane of the molecule (x–y), as shown on the top panel. External magnetic field $\mathbf{B}$ produces the effective fields $\mathbf{b} = g_{\rm mol}\mu_{\rm B}\mathbf{B}$, which is tilted by the angle ψ from the normal $\mathbf{e}_z$ to the plane of the molecules, and lies in the z–x plane. The fields $\tilde{\mathbf{b}}(\pm 1/2)$ form angles $\theta_{\pm 1/2}$ with the z-axis, and define quantization axes of spin, as shown on the bottom left panel and described in the main text. On the bottom right panels, the effective quantization axes of the states with energies E_{C_z,S_z} are illustrated by arrows. The cavity field induces transitions between the states of equal spins and different chiralities, represented by the wavy lines. The angle $\delta = \theta_{-1/2} - \theta_{1/2}$ determines the coupling strength of different transitions.

magnets in a strip-line cavity is then described by a generalization of the Dicke model, see figure 1.

Molecular magnets are molecules with strong exchange interaction and pronounced spin anisotropy in the low-energy sector. At low energies they can be described as a set of interacting spins localized at positions of magnetic centers. The strong anisotropy governs the relaxation from spin-ordered states so that the transitions occur through quantum tunneling of magnetization over the anisotropy-induced barrier. In antiferromagnetic triangular molecules, the low energy states are two doublets of total spin $S = 1/2$, distinguished by the chirality of their spin textures $C_z = \pm 1/2$. Symmetry analysis then leads to the prediction that the transitions between the states of same spin and different chiralities are induced by external electric fields in the molecule's plane. This transition suggests that the spin order in these molecules can be manipulated by an external electric fields.

We find that the cavity and molecular magnets can be driven through the transition by modifying the direction or intensity of the external magnetic field. The critical coupling for the transition is magnetic field dependent, due to the interaction between the spins within the molecules. Spin interaction makes the ground- and low-energy excited states coherent superpositions of entangled total spin and chirality of the spin texture. In molecular magnets [17], the quantum coherence was crucial for explaining the dynamics of magnetization: transitions between the spin states are coherent processes, and show the interference between transition paths [18–20] and the Berry phase [21–23]. The superradiant phase transition would therefore provide a way to study the spin coherence in the single-molecule magnets. In addition, observation of the magnetically controllable transition would prove the existence of spin-electric interaction.

Superradiance, the relaxation of an ensemble of emitters at a rate proportional to the square of their number, is another manifestation of coherent coupling of emitters to the quantized cavity field. It was predicted to occur in the molecular magnets, but the experimental results so far remain inconclusive [24–30]. As opposed to superradiance, the superradiant phase is a ground state property of the coupled emitter-cavity system. Therefore, the detection of the superradiant phase requires measurement of the static properties of the coupled emitter-cavity system, and not the following of the dynamics of relaxation from the excited state.

Control of our predicted superradiant phase transition is specific for the model of triangular spin-1/2 antiferromagnetic molecular magnets, since it depend on the form of spin-electric coupling. In addition to the specific form, the transition requires the interaction of sufficient strength. Experiments on molecular magnets, like charged Fe{4} clusters [31], and Mn ions in piezoelectric crystals [32] do show coupling of spins to electric fields. In these cases the electric fields modify the spin anisotropy. This interaction may allow for a similar analysis of electrically driven superradiant phase transition, once the details of the spin-electric interaction are known.

2. Model

At low energy, triangular molecular antiferromagents are characterized by the total spin, $\mathbf{S} = \sum_{i=1}^{3}\mathbf{s}_i$, where i counts the spins-1/2 on magnetic centers, and pseudospin-1/2 chirality $\mathbf{C}$, associated with the spin texture, see figure 1. The components of the chirality are defined in terms of spin operators as

$$C_x = -\frac{1}{3}(\mathbf{s}_1 \cdot \mathbf{s}_2 - 2\mathbf{s}_2 \cdot \mathbf{s}_3 + \mathbf{s}_3 \cdot \mathbf{s}_1), \tag{1}$$

$$C_y = \frac{1}{3}(\mathbf{s}_1 \cdot \mathbf{s}_2 - \mathbf{s}_3 \cdot \mathbf{s}_1), \tag{2}$$

$$C_z = \frac{1}{8\sqrt{2}}\mathbf{s}_1 \cdot (\mathbf{s}_2 \times \mathbf{s}_3). \tag{3}$$

The components C_x and C_y are two-spin operators that, in analogy with the Pauli spin operators, flip the chirality C_z, which is a three-spin operator [16]. The operators $\mathbf{S}$ and $\mathbf{C}$ are independent and satisfy spin commutation relations: $[S_i, S_j] = i\epsilon_{ijk}S_k$, $[C_i, C_j] = i\epsilon_{ijk}C_k$, and $[S_i, C_j] = 0$, where i, j, and k count the Cartesian components of spin and chirality [16, 33]. Strong antiferromagnetic exchange between the

molecular spins constrains the total spin of the molecule to $S = 1/2$. This model is valid at the temperatures below the gap to excited $S = 3/2$ states, typically of the order of 10 K in spin triangles [34].

The two degrees of freedom, **S** and **C**, couple differently to external fields: while the spin couples to the magnetic field via Zeeman term, the chirality couples to $\mathbf{E}_\parallel$, the components of external electric field in the plane of the triangular molecule [16]. The Hamiltonian of the molecular magnet in external electric and magnetic fields is [16]

$$H_{\rm mol} = 2\Delta_{\rm SO} C_z S_z + \mathbf{b}\cdot\mathbf{S} + d_0 \mathbf{E}_\parallel \cdot \mathbf{C}. \tag{4}$$

The Bohr magneton, $\mu_{\rm B}$, and the molecular gyromagnetic ratio, $g_{\rm mol}$, are absorbed in the effective magnetic field $\mathbf{b} = g_{\rm mol}\mu_{\rm B}\mathbf{B}$, and we set $\hbar = 1$. The zero-field splitting, $\Delta_{\rm SO}$, caused by the spin–orbit interaction and with a typical strength $\Delta_{\rm SO}/(g\mu_{\rm B}) \sim 1$ T, produces an Ising coupling between S_z and C_z, with the spin z axis normal to the molecule's plane [17, 34]. The chirality interacts with the in-plane components of the electric field and, through the Ising coupling, with **S**, the total spin [16, 33]. The selection rules for electrically driven transitions in equation (4) are set by the D_{3h} symmetry of the molecule, and read $\Delta C_z = \pm 1$. Therefore, it is possible to access the transitions that would be forbidden by the selection rules $\Delta S_z = \pm 1$ which are valid for the magnetic driving [33].

A crystal of N emitters interacting with a mode of the resonant cavity is described by

$$H = H_{\rm cav} + \sum_j H_{0,j} + \sum_j V_j, \tag{5}$$

where $H_{\rm cav} = \omega a^\dagger a$ describes the cavity photon, and each $H_{0,j} = 2\Delta_{\rm SO} C_{j,z} S_{j,z} + \mathbf{b}\cdot\mathbf{S}_j$ describes a molecule interacting with an external classical magnetic field **B**. The interaction terms

$$V_{\rm j} = d\,(a + a^\dagger) C_{j,x}, \tag{6}$$

are couplings of molecules to the electric component of quantized cavity field. The operator a ($a^\dagger$) annihilates (creates) a cavity photon. The coupling constant $d = d_0 E_x$ includes both the intrinsic single-molecule spin-electric coupling d_0 and the in-plane electric field amplitude E_x. The molecules in a crystal lie in parallel planes, so that their spin quantization axes all point in the same direction [35] that we label z, see figure 1. Any variation of molecular orientations, e.g., due to crystal defects, is equivalent to a change in the effective coupling between the molecular spins and the cavity photons. We assume that the Zeeman coupling of **S** to the magnetic component of the cavity field is weak, as in the microwave cavities with molecules placed near the maximum of the electric field amplitude [36], and do not include it in equation (5).

The non-interacting Hamiltonian, $H_0 = H_{\rm cav} + \sum_j H_{0,j}$, conserves the number of photons $\hat{n} = a^\dagger a$, as well as the z-components of chiralities, $C_{j,z}$. Within each simultaneous eigenspace of $\hat{n}$ and $C_{j,z}$ it reduces to a spin Hamiltonian

$$H_{0;j;n,c} = n\omega + \mathbf{b}\cdot\mathbf{S}_j + 2c\Delta_{\rm SO} S_{j,z}, \tag{7}$$

where n and c are the respective eigenvalues of the operators $\hat{n}$ and $C_{j,z}$. This reduced Hamiltonian is readily diagonalized, and we find the energies

$$E_{n,c,s} = s|\tilde{\mathbf{b}}(c)| + n\omega \tag{8}$$

and the eigenstates

$$|n,\, c,\, s\rangle = |n,\, c\rangle \otimes |\mathbf{S}\cdot\mathbf{e}_c = s\rangle. \tag{9}$$

The effective magnetic fields are $\tilde{\mathbf{b}}(c) = \mathbf{b} + 2c\Delta_{\rm SO}\mathbf{e}_z$, with $c = \pm 1/2$, and $s = \pm 1/2$ denotes the molecule's spin projection along $\mathbf{e}_c$, the direction of effective field $\tilde{\mathbf{b}}(c)$. Explicitly, the molecule's eigenstates in the $C_{j,z}$, $S_{j,z}$ basis are given by the unitary transformation $|n,\, c,\, s\rangle = |n\rangle \otimes U|c,\, s_z\rangle$, where $U = \sum_{c=\pm 1/2} P_{\rm c} \exp(-i\,\theta_{\rm c} S_y)\, P_{\rm c}$ maps the state $|c,\, s_z\rangle$ of the molecule with chirality c and spin projection s_z to the z-axis into a state with the same chirality and the spin projection $s = s_z$ along the rotated spin axis (see figure 1). The angles $\theta_{\pm 1/2}$ are

$$\theta_{\rm c} = \arccos \frac{2c\Delta_{\rm SO} + b\cos\psi}{\sqrt{b^2\sin^2\psi + (2c\Delta_{\rm SO} + b\cos\psi)^2}} \tag{10}$$

with ψ and b denoting the polar angle and intensity of the field **b**. The operators $P_{\rm c} = 2\,c\,C_z + 1/2$ are projectors to the states of a given chirality c.

3. Rotating wave approximation (RWA)

As opposed to the standard Jaynes–Cummings model in quantum optics [37], the RWA for a single-molecule magnet in a cavity cannot be obtained by simply neglecting the terms proportional to $C_+a^\dagger$ and C_-a, since the chirality interacts with the spin, which in addition couples to an external magnetic field.

To derive the RWA of equation (5) we switch to the interaction picture, $V_j(t) = e^{iH_0 t} V_j e^{-iH_0 t}$, with respect to the terms $H_0 = \sum_j H_{0,j}$ that do not involve the interaction of the molecule with the cavity electric field. Using the known eigenvalues and eigenstates of H_0, we find

$$V_j(t) = \frac{d}{2} \sum_{n,c,s,s'} e^{i(E_{n,c,s} - E_{n,-c,s'})t} M(c,\, s,\, s') \times |n,\, c,\, s\rangle\langle n,\, -c,\, s'|(e^{i\omega t}a^\dagger + e^{-i\omega t}a\,), \tag{11}$$

where $M(c,\, s,\, s') = \langle \mathbf{S}_j\cdot\mathbf{e}_c = s|\mathbf{S}_j\cdot\mathbf{e}_{-c} = s'\rangle$ is the scalar product of the spins with projections s and s' on the axes $\mathbf{e}_c$ and $\mathbf{e}_{-c}$. Explicitly, $M(c,\, s,\, s) = \cos(\delta/2)$, $M(\pm 1/2,\, s,\, -s) = \mp i\sin(\delta/2)$, $\delta = \theta_{-1/2} - \theta_{1/2}$, and the angles $\theta_{\pm 1/2}$ are given in equation (10).

The RWA consists of neglecting the terms in the interaction-picture Hamiltonian, equation (11), that oscillate with frequencies close to molecular transitions $\omega_{ij} \sim |E_i - E_j|$, and keeping the terms that oscillate slowly, with frequencies close to the detuning between the transition and the cavity mode. In this case the fast-oscillating terms average out to zero, and we can neglect them. The resonant frequencies in our model are $\omega_{\rm r}^{\pm} = (|\tilde{\mathbf{b}}(1/2)| \pm |\tilde{\mathbf{b}}(-1/2)|)/2$. We have set the direction of z axis so that $|\tilde{\mathbf{b}}(1/2)| \geqslant |\tilde{\mathbf{b}}(-1/2)|$.

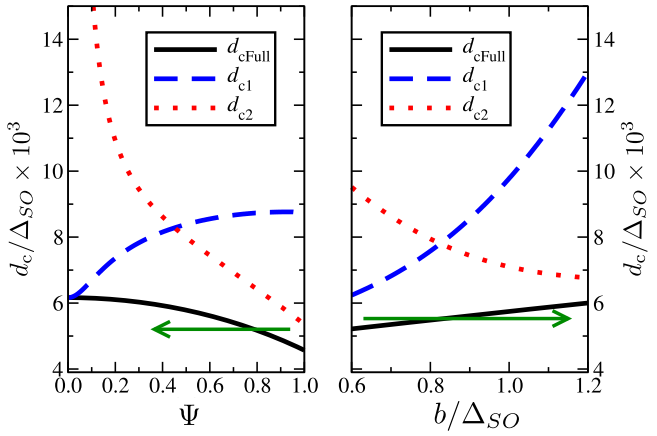

Figure 2. The critical couplings in the full RWA ($d_{\rm cFull}$), in standard RWAs near $\omega_{\rm r}^{+}$ ($d_{\rm c1}$), and near $\omega_{\rm r}^{-}$ ($d_{\rm c2}$), as a function of angle with respect to the normal to molecule's plane ψ, and the intensity b of the external magnetic field **b**, respectively. Variations in either ψ or b lead the system through the superradiant quantum phase transition (motion along the arrows switches from $d > d_{\rm c}$ to $d < d_{\rm c}$). For this figure, the number of molecules is $N = 10^5$, and the cavity frequency is the mean of the two resonant frequencies $\omega = (\omega_{\rm r}^{+} + \omega_{\rm r}^{-})/2$ (see text). On the first panel $b = 0.9\Delta_{\rm SO}$, and on the second $\psi = 0.6$ rad.

The condition for the validity of the RWA is that the molecule-cavity coupling constant d is much smaller than the resonant frequencies, $d \ll \omega_{\rm r}^{\pm}$. In addition, the RWA can reproduce the standard model of a two-level emitter when the cavity frequency is tuned close to one of the transitions and far from the other, e.g., $|\omega - \omega^{+}| \gg |\omega - \omega^{-}|$. This tuning is possible only when

$$|\omega_{\rm r}^{+} - \omega_{\rm r}^{-}| \gg d. \tag{12}$$

The condition in equation (12) can not be satisfied when $\mathbf{b} \approx \Delta_{\rm SO}\mathbf{e}_z$, i.e., when the magnetic field axis is near the normal to the molecule, and the magnetic field intensity is comparable to spin-orbit splitting $\Delta_{\rm SO}$. We will focus on the case when both resonances have to be taken into account, either due to the deliberate tuning of the cavity frequency, or due to violation of equation (12). In this case, the amplitudes of the resonant transitions vary strongly with the magnetic field, and we will see that this leads to new effects. When equation (12) is satisfied, the cavity can be tuned so that the RWA leads to the Tavis–Cummings model [3, 4], and consequently to the familiar superradiant phase transition and a single transition resonant with the cavity, see figure 2. We will label the critical couplings in approximations that keep a single transitions as $d_{c1}(d_{c2})$.

After the removal of the counter-rotating terms and switching back to the Schrödinger picture, the molecule-cavity interaction is

$$V_{\rm RWA} = d\sum_j (a + a^{\dagger})\left(\frac{\cos\delta}{2}C_{j,x} - \sin\delta\, S_{j,y}C_{j,y}\right) + i(a - a^{\dagger})\left(\sin\theta_{-\frac{1}{2}}S_{j,x} + \cos\theta_{-\frac{1}{2}}S_{j,z}\right)C_{j,y}. \tag{13}$$

The final Hamiltonian in RWA is $H_{\rm RWA} = H_0 + V_{\rm RWA}$, and it is analogous to the Tavis–Cummings model of two-level atoms in a resonant cavity. Similarly to the conservation of the number of excitations in the Tavis–Cummings model, $H_{\rm RWA}$ conserves the quantity

$$N_{\rm exc} = \hat{n} + \sum_j (1 + \tilde{S}_{j,z} + 2C_{j,z}\tilde{S}_{j,z}), \tag{14}$$

where $\tilde{\mathbf{S}}_j = U\mathbf{S}_j U^{\dagger}$, with U defined above equation (10). We interpret $N_{\rm exc}$ as the conserved number of excitations by counting molecules in the state $|c, s\rangle = |1/2, -1/2\rangle$ as zero excitations, molecules in the states $|-1/2, \pm 1/2\rangle$ as one excitation, molecules in the state $|1/2, 1/2\rangle$ as two excitations, and each cavity photon as one excitation. We choose an additive constant so that $N_{\rm exc} = 0$ corresponds to all the molecules in the state $|1/2, -1/2\rangle$ and no photons in the cavity.

4. Superradiant quantum phase transition

We study the superradiant phase transition in the rotating wave and mean-field approximations. This amounts to substituting photon annihilation(creation) operator $a(a^{\dagger})$ by their expectation value $\langle a\rangle(\langle a\rangle^*)$ in $H_{\rm RWA}$, thus neglecting any quantum fluctuations. This approximation is valid for large photon numbers, $n \gg 1$. The mean-field energy, $E_{\rm MF}(\langle a\rangle)$ is the ground state energy of

$$H_{\rm RWA}^{\rm MF}(\langle a\rangle) = \omega|\langle a\rangle|^2 + \sum_j H_{0,j} + V_{\rm RWA}(\langle a\rangle). \tag{15}$$

We find that $E_{\rm MF}(\langle a\rangle)$ is independent of the phase of $\langle a\rangle$, which we set to be real in further discussion. The mean-field value of the annihilation operator, $\langle a\rangle_{\rm MF}$ is, by the self-consistency condition, the value of $\langle a\rangle$ for which $E_{\rm MF}(\langle a\rangle)$ is at a minimum. Similarly, the mean field state of the molecules is the ground state of $H_{\rm RWA}^{\rm MF}(\langle a\rangle_{\rm MF})$. Without RWA, the phase of $\langle a\rangle_{\rm MF}$ is set by the minimization requirement so that the quantity is real [38].

When the cavity is decoupled from the molecules, $d = 0$, the system is in the normal state, and $\langle a\rangle_{\rm MF} = 0$. The superradiant phase transition means the appearance of $\langle a\rangle_{\rm MF} > 0$ for coupling strength larger than the critical value, $d > d_{\rm c}$. We analytically determine the critical coupling $d_{\rm c}$ from the properties of $E_{\rm MF}(\langle a\rangle)$. In the absence of photons, $E_{\rm MF}(0)$ is a finite ground state energy of N molecules in the ground state. For large photon numbers, the energy is dominated by the free photon term, and therefore diverges, $\lim_{\langle a\rangle\to\infty} E_{\rm MF} = \infty$. Furthermore, since $E_{\rm MF}(\langle a\rangle)$ explicitly depends only on the square of its argument, $\partial_{\langle a\rangle}E_{\rm MF}|_{\langle a\rangle=0} = 0$. We determine the critical coupling as the smallest value of d for which $\partial^2_{\langle a\rangle}E_{\rm MF}(\langle a\rangle)|_{\langle a\rangle=0} < 0$. Together with the limiting values and the zero derivative at zero, this condition guarantees the existence of a minimum for the mean-field energy that is lower than $E_{\rm MF}(0)$ at some finite value of $\langle a\rangle$.

The procedure of minimization applied to $H_{\rm RWA}^{\rm MF}$, equation (15), and using the RWA potential with both

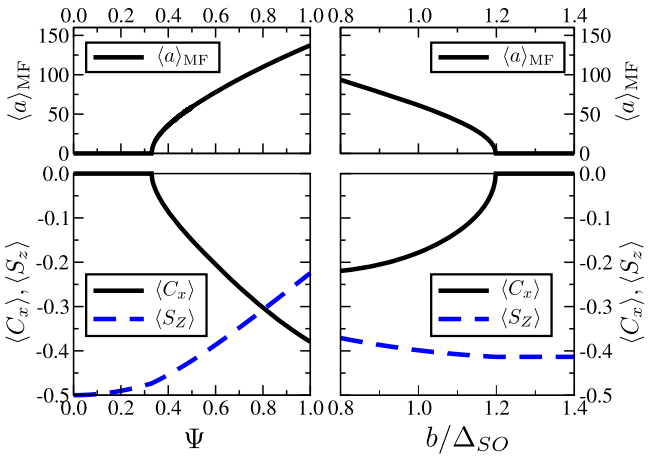

Figure 3. Response of molecules and cavity field to the changes in direction ψ (first panel) and intensity b (second panel) of the external magnetic field **b**. At the superradiant transition, the mean-field value of the photon annihilation operator $\langle a\rangle_{\rm MF}$ becomes nonzero (upper panels). At the same value of **b**, an in-plane electric polarization $\propto\langle C_x\rangle$ appears, signaling the superradiant phase. The magnetization normal to the molecule's plane $\propto\langle S_z\rangle$ shows a more rapid change with **b** then in the normal state. System parameters are the same as in figure 2, and $d = 6 \times 10^{-3}\Delta_{\rm SO}$.

resonances, equation (13) gives the critical coupling

$$d_{\rm cFull} = \sqrt{\frac{8\omega\Delta_{\rm SO}b}{N\left[\tilde{b}\left(\frac{1}{2}\right) + \tilde{b}\left(-\frac{1}{2}\right)\cos\delta\right]}}. \qquad (16)$$

This **b**-dependent $d_{\rm cFull}$ is one of our main results, figure 2. The dependence is due to both the modification of the energy levels of H_0, and to modification of the coupling constants for transitions through spin-overlap terms in equation (13). The result, equation (16) clearly can not be explained by the usual RWA at either of the resonant frequencies, as illustrated in figure 2. The value of $\langle a\rangle_{\rm MF}$ grows as $\langle a\rangle_{\rm MF} \propto \sqrt{d - d_{\rm c}}$ for $d > d_{\rm c}$, and $\langle a\rangle_{\rm MF} \propto \sqrt{N}$. We note that the mean-field approximation can be applied to the Hamiltonian equation (5) without the RWA, predicting the superradiant phase transition with the critical coupling scaled by a factor of 2 form the value in equation (16). The dependence of $d_{\rm c}$ on **b** allows for a controllable superradiant phase transition. Changes in $d_{\rm c}$, given by equation (16), can lead the system into or out of the superradiant phase, see figure 2. The measurement of the escaping radiation as done, for example, by using input–output theory [39], would then serve as a signature of superradiant state [9, 40–42]. Turning the tables, identifying the superradiant phase transition would allow to extract the value of the spin-electric coupling constant.

The quantum properties of escaping light can not be determined in the mean-field theory, since we assume that the radiation is in a specific classical state described by the expectation value $\langle a\rangle_{\rm MF}$. However, in the superradiant phase of the Dicke model, the emitted radiation is nonclassical in the sense that is cannot be described by a positive-definite probability distribution function [43]. We expect that there are quantum correlations of emitted light from our system, but their evaluation is beyond the scope of this work.

In addition to the nonzero photon occupation of the cavity mode, see figure 3, the transition is characterized by a change in the expectation value of the chirality. For $d < d_{\rm c}$, the molecules are in the state with $C_{j,z} = -1/2$, with zero expectation values of $C_{j,x(y)}$. After the transition, for $d > d_{\rm c}$, the in-plane components of chirality have nonzero expectation value, i.e., $\langle C_{j,x}\rangle \neq 0$ in our model. The fact that only the x-components gets a finite expectation value comes from our phase convention for $\langle a\rangle$, and the form of the interaction with the electric fields [38]. The molecules develop electric dipole moments for $d > d_{\rm c}$, and the transition can be detected by the electric response, for example by measuring the spin-electric susceptibility [33], as well as by the emitted radiation, lower panels of figure 3.

5. Experimental requirements

The detection of the controllable superradiant phase transition is possible in an experiment that would monitor the escaping radiation or the electric response of the molecular magnets coupled to a cavity, as they are driven through the transition by a change in external magnetic field. The transition occurs when $d_0 E_x > d_{\rm c}$, see equation (16), and the controllable transition can be achieved for large electric field amplitude E_x and strong molecular spin-electric coupling d_0. The critical coupling strength diminishes with the increasing number of molecules, $d_{\rm c} \propto N^{-1/2}$. Other parameters that influence $d_{\rm c}$ are the strength of the magnetic field required for control and the cavity frequency. Both are set by the zero-field splitting of the molecular magnet, $\Delta_{\rm SO} \approx g\mu_{\rm B}{\rm B} \approx \hbar\omega$. The typical value of zero-field splitting in triangular molecular antiferromagnets [34, 44] is $\Delta_{\rm SO} \sim 1\ {\rm K}\cdot k_{\rm B}$. Therefore, the relevant resonant frequencies lie in the microwave range, $f = \omega/(2\pi) \sim 15$ GHz, and the external magnetic fields needed for control are $B \sim 1$ T.

We take the estimate for the value of the molecular spin-electric coupling constant, $d_0 \sim 10^{-4}|eR_0|$, where R_0 is the distance between the magnetic centers in the molecule from the *ab-initio* work [45, 46]. The corresponding numerical value of the dipole moment is $d_0 \sim 10^{-32}$ Cm. Assuming the electric field amplitude $E_x = \sqrt{\hbar\omega/c_1 V}$, where c_1 is the resonator capacitance per unit length, and V is the mode volume, we estimate that $E_x \sim 100$ V/m is achievable in narrow strip-line cavities [47], giving $d = d_0 E_x \sim 10^{-11}$ eV. Under these conditions, the controllable superradiant phase transition will occur if the crystal coupled to the cavity electric field contains $N > N_{\rm c} \sim 10^{15}$ molecular magnets. Spin ensembles of comparable effective volume were coupled to microwaves by placing them on top of the resonators [48–50].

Coupling such a large number of molecules to a resonant cavity requires very dense crystals, with the intermolecular distances about 20 times shorter than typical 1 nm, i.e., the critical density $n_{\rm c}$ is four orders of magnitude too large. There are two molecular parameters that can be manipulated to relax

this requirement, the zero-field splitting, Δ_{SO}, and the intrinsic spin-electric coupling strength of a single molecule, d_0. Estimating the cavity electric field from a single photon energy in the mode volume implies $E_x \propto \sqrt{\omega}$. Taking into account that the control magnetic field, b, the effective fields, $\tilde{b}(\pm 1/2)$, and the resonant frequency, ω, all scale with Δ_{SO}, equation (16) implies

$$n_c \propto \frac{\Delta_{SO}}{d_0^2}. \tag{17}$$

Triangular molecular magnets come in great variety, and the chemical alteration of their composition gives access to many spin Hamiltonians at low energies. The zero field splitting can be as low as $\Delta_{SO} \approx 3 \times 10^{-2}$ K, and potentially even lower [51], with the values in V_{15}, Fe_8, and Cu_3 complexes in the range $10^{-2} - 1$ K [35, 51–55]. Modification of the intrinsic spin-electric coupling, d_0, can reduce the critical density even more. Since $n_c \propto d_0^{-2}$, and increase in d_0 does not affect any other experimental parameter, searching for the molecules with large d_0 may be the right way to achieve the proposed controllable superradiant phase transition in a laboratory. An increase in d_0 by a factor of 100 from the numerically predicted value [45, 46] would bring the critical density to the value of 1 nm^{-3}.

The magnetic field dependent critical coupling, equation (16), is found in the model that assumes an ideal cavity, zero temperature, and validity of the mean-field approach. The constraints for the realistic experiments are less stringent. The superradiant phase appears in the system's ground state which is predominantly occupied at temperatures lower than the first molecule's excitation, $T \ll \Delta_{SO}/k_B \sim 1$ K. The time scale of relaxation to the superradiant ground state is given by the spin relaxation time of the molecular magnet, which can be as long as a microsecond [44]. This time should be longer than the Rabi time of the collective coupling between the molecules and the field mode, i.e. there should be many Rabi oscillations before the spins relax. For $N > N_c$, this requirement is satisfied due to scaling of the Rabi frequency. In addition, the cavity decay time should be longer than the spin decay time, which would require the cavity Q-factor of the order $Q \sim 10^5$–10^6 for long spin coherence times of $\tau_s \sim 1\ \mu$s, and less stringent $Q \sim 10^3$–10^4 for $\tau_s \sim 10$ ns. In superconducting stripline cavities, the external magnetic field of the order of 1 T would reduce the Q-factor, unless the field lies in the plane of the strips. There is a geometry that allows for the variation of the angle ψ between the magnetic field **b** and the normal to triangles while keeping **b** in the plane of the superconductors. In this geometry, the triangles should lie in the plane normal to the axis of the strips. Further enhancement of Q-factor is possible by resonator engineering [56].

As a matter of principle, it is not necessary to use the stripline cavities, and any microwave resonator with large regions of significant electric field and sufficient Q-factor can support the superradiant phase transition. Manipulation of the electric field amplitude of the cavity mode and choosing a shape that can accommodate many molecules can be an efficient way to reach the required coupling strength, since $N_c \propto E_x^{-2}$. Therefore, 3D cavities can also be used.

The disorder in the molecule's energies due to imperfections of the crystal may bring some of the molecules out of resonance and reduce the effective N below the total number of molecules. However, the superradiant effect also suppresses such inhomogeneous broadening [57–59]. When the collective coupling of many emitters exceeds the bandwidth of their ensemble, the broadening vanishes altogether so that even far off-resonant molecules interact strongly with the field mode. This allows one to increase the number of active emitters in the cavity in realistic devices.

6. Conclusions

We have introduced a model of a crystal of single-molecule triangular antiferromagnets interacting with an external classical homogeneous magnetic field and the electric component of a quantized cavity field. The model shows a superradiant quantum phase transition with the critical coupling tunable by applied magnetic field. The strong coupling regime is characterized by nonzero mean photon number and electric dipole moment in the triangle plane. With state-of-the-art cavities and current estimates of spin-electric coupling strength, the tunable transition is achievable for 10^{15} molecules coupled to the cavity. This value can be reduced by choosing the molecules with weak zero-field splitting Δ_{SO} and strong intrinsic spin-electric coupling d_0. Observation of the predicted transition and its magnetic field dependence can serve as a probe of spin-electric interaction. While our models describes triangular single-molecule magnets, it can be extended in order to study of other emitters described by entangled discrete degrees of freedom.

Acknowledgments

We acknowledge discussions with Filippo Troiani. This work is funded from Serbian MPNTR grant OI171032, Swiss NF through NCCR QSIT and SCOPES IZ73Z0152500, public grant from the Laboratoire d'Excellence Physics Atom Light Matter (LabEx PALM, reference: ANR-10- LABX-0039), and EPSRC Grant No. EP/J016888/1.

References

[1] Dicke R H 1954 *Phys. Rev.* **93** 99
[2] Jaynes E and Cummings F 1963 *Proc. IEEE* **51** 89
[3] Tavis M and Cummings F W 1968 *Phys. Rev.* **170** 379
[4] Tavis M and Cummings F W 1969 *Phys. Rev.* **188** 692
[5] Hepp K and Lieb E H 1973 *Ann. Phys., NY* **76** 360
[6] Wang Y K and Hioe F T 1973 *Phys. Rev.* A **7** 831
[7] Strack P and Sachdev S 2011 *Phys. Rev. Lett.* **107** 277202
[8] Baumann K, Guerlin C, Brennecke F and Esslinger T 2009 *Nature* **464** 1301
[9] Baumann K, Mottl R, Brennecke F and Esslinger T 2011 *Phys. Rev. Lett.* **107** 140402

[10] Domokos P and Ritsch H 2002 *Phys. Rev. Lett.* **89** 253003
[11] Larson J and Lewenstein M 2009 *New J. Phys.* **11** 063027
[12] Knight J M, Aharonov Y and Hsieh G T C 1978 *Phys. Rev.* A **17** 1454
[13] Bialyncki-Birula I and Kazimierz R 1979 *Phys. Rev.* A **19** 301
[14] Viehmann O, von Delft J and Marquardt F 2011 *Phys. Rev. Lett.* **107** 113602
[15] Zou L J, Marcos D, Diehl S, Putz S, Schmiedmayer J, Majer J and Rabl P 2014 *Phys. Rev. Lett.* **113** 023603
[16] Trif M, Troiani F, Stepanenko D and Loss D 2008 *Phys. Rev. Lett.* **101** 217201
[17] Gatteschi D, Sessoli R and Villain J 2006 *Molecular Nanomagnets* (Oxford: Oxford University Press)
[18] Loss D, DiVincenzo D P and Grinstein G 1992 *Phys. Rev. Lett.* **69** 3232
[19] Leuenberger M N and Loss D 2000 *Phys. Rev.* B **61** 1286
[20] Leuenberger M N, Meier F and Loss D 2003 *Mon.hefte Chem.* **134** 217
[21] Wernsdorfer W and Sessoli R 1999 *Science* **284** 133
[22] González G and Leuenberger M N 2007 *Phys. Rev. Lett.* **98** 256804
[23] González G, Leuenberger M N and Mucciolo E R 2008 *Phys. Rev.* B **78** 054445
[24] Chudnovsky E M and Garanin D A 2002 *Phys. Rev. Lett.* **89** 157201
[25] Tejada J, Amigo R, Hernandez J M and Chudnovsky E M 2003 *Phys. Rev.* B **68** 014431
[26] Amigó R, Tejada J, Chudnovsky E, Hernandez J and Garca-Santiago A 2004 *J. Magn. Magn. Mater.* **272–276** 1106 Proc. Int. Conf. on Magnetism (ICM 2003), http://sciencedirect.com/science/article/pii/S0304885303026325
[27] Bal M, Friedman J R, Mertes K, Chen W, Rumberger E M, Hendrickson D N, Avraham N, Myasoedov Y, Shtrikman H and Zeldov E 2004 *Phys. Rev.* B **70** 140403
[28] Yukalov V I, Henner V K, Kharebov P V and Yukalova E P 2008 *Laser Phys. Lett.* **5** 887
[29] Shafir O and Keren A 2009 *Phys. Rev.* B **79** 180404
[30] Leviant T, Hanany S, Myasoedov Y and Keren A 2014 *Phys. Rev.* B **90** 054420
[31] Nossa J F, Islam M F, Canali C M and Pederson M R 2013 *Phys. Rev.* B **88** 224423
[32] George R E, Edwards J P and Ardavan A 2013 *Phys. Rev. Lett.* **110** 027601
[33] Trif M, Troiani F, Stepanenko D and Loss D 2010 *Phys. Rev.* B **82** 045429
[34] Choi K-Y, Matsuda Y H, Nojiri H, Kortz U, Hussain F, Stowe A C, Ramsey C and Dalal N S 2006 *Phys. Rev. Lett.* **96** 107202
[35] Bertaina S, Chen L, Groll N, Van Tol J, Dalal N S and Chiorescu I 2009 *Phys. Rev. Lett.* **102** 050501
[36] Imamoğlu A 2009 *Phys. Rev. Lett.* **102** 083602
[37] Mandel L and Wolf E 1995 *Optical Coherence and Quantum Optics* (Cambridge: Cambridge University Press)
[38] Baksic A and Ciuti C 2014 *Phys. Rev. Lett.* **112** 173601
[39] Clerk A A, Devoret M H, Girvin S M, Marquardt F and Schoelkopf R J 2010 *Rev. Mod. Phys.* **82** 1155
[40] Ciuti C, Bastard G and Carusotto I 2005 *Phys. Rev.* B **72** 115303
[41] Auer A and Burkard G 2012 *Phys. Rev.* B **85** 235140
[42] Kopylov W, Emary C and Brandes T 2013 *Phys. Rev.* A **87** 043840
[43] Nataf P, Dogan M and Hur K Le 2012 *Phys. Rev.* A **86** 043807
[44] Bertaina S, Gambarelli S, Mitra T, Tsukerblat B, Muller A and Barbara B 2008 *Nature* **453** 203
[45] Islam M F, Nossa J F, Canali C M and Pederson M 2010 *Phys. Rev.* B **82** 155446
[46] Nossa J F, Islam M F, Canali C M and Pederson M R 2012 *Phys. Rev.* B **85** 085427
[47] Trif M, Golovach V N and Loss D 2008 *Phys. Rev.* B **77** 045434
[48] Schuster D I *et al* 2010 *Phys. Rev. Lett.* **105** 140501
[49] Kubo Y *et al* 2011 *Phys. Rev. Lett.* **107** 220501
[50] Zhu X *et al* 2011 *Nature* **478** 221
[51] Spielberg E T, Gilb A, Plaul D, Geibig D, Hornig D, Schuch D, Buchholz A, Ardavan A and Plass W 2015 *Inorg. Chem.* **54** 3432
[52] Chiorescu I, Wernsdorfer W, Müller A, Bögge H and Barbara B 2000 *Phys. Rev. Lett.* **84** 3454
[53] De Raedt H, Miyashita S, Michielsen K and Machida M 2004 *Phys. Rev.* B **70** 064401
[54] Chaboussant G, Ochsenbein S T, Sieber A, Gudel H- U, Mutka H, Muller A and Barbara B 2004 *Europhys. Lett.* **66** 423
[55] Burzurí E, Luis F, Montero O, Barbara B, Ballou R and Maegawa S 2013 *Phys. Rev. Lett.* **111** 057201
[56] de Graaf S E, Danilov A V, Adamyan A, Bauch T and Kubatkin S E 2012 *J. Appl. Phys.* **112** 123905
[57] Tsyplyatyev O and Loss D 2009 *Phys. Rev.* A **80** 023803
[58] Tsyplyatyev O and Loss D 2010 *Phys. Rev.* B **82** 024305
[59] Sträter C, Tsyplyatyev O and Faribault A 2012 *Phys. Rev.* B **86** 195101

PAPER

Variation of electric properties across the grain boundaries in $BiFeO_3$ film

IOP Publishing Journal of Physics D: Applied Physics
J. Phys. D: Appl. Phys. **49** (2016) 045309 (9pp) doi:10.1088/0022-3727/49/4/045309

Variation of electric properties across the grain boundaries in $BiFeO_3$ film

Bojan Stojadinović[1], Borislav Vasić[1], Dimitrije Stepanenko[1], Nenad Tadić[2], Radoš Gajić[1] and Zorana Dohčević-Mitrović[1]

[1] Center for Solid State Physics and New Materials, Institute of Physics Belgrade, University of Belgrade, Pregrevica 118, 11080 Belgrade, Serbia
[2] Faculty of Physics, University of Belgrade, Studentski trg 12-16, 11000 Belgrade, Serbia

E-mail: bvasic@ipb.ac.rs and zordoh@ipb.ac.rs

Received 13 October 2015, revised 3 December 2015
Accepted for publication 8 December 2015
Published 29 December 2015

Abstract

Stark differences in charge transport properties between the interior and the boundary regions of grains in an undoped $BiFeO_3$ thin film have been found. The material is ferroelectric and each grain is a single domain. A spatial resolution that distinguishes between the grain interior and the boundary between the grains has been achieved by using piezoelectric force microscopy and conductive atomic force microscopy measurements. The local electric properties, as well as the local band gap show hysteresis only when probed in the grain interior, but do not show hysteresis when probed in the region around the boundary between two grains. The leakage current is more pronounced at the grain boundaries, and the region that carries significant current increases with the applied voltage.

Keywords: multiferroics, thin films, electrical properties, grain boundaries, scanning probe microscopy

S Online supplementary data available from stacks.iop.org/JPhysD/49/045309/mmedia

(Some figures may appear in colour only in the online journal)

1. Introduction

Multiferroic materials exhibit at least two ferroic properties among magnetic, electric, and elastic responses. Simultaneous presence of at least two hysteretic responses and interaction between the associated orders has spurred interest in the mechanisms that govern the phase transitions in multiferroics [1–3]. The explanation of the multiferroic order remains an interesting open problem of condensed matter physics. A pair of ferroic properties causes nonlinear and nonstandard responses, e.g. a material will produce electric polarization when exposed to an external magnetic field. Such responses make the multiferroics interesting from a practical point of view by allowing for novel forms of control. The most sought-after applications of multiferroics are electrically controlled magnetic memories [4], and emerging spintronic devices based on the simultaneous use of electric polarization, based on the orbital order, and magnetization, based on the spin order [2, 5].

The properties of multiferroic materials structured at the nanoscale can be drastically different from the corresponding properties of the bulk. Integration of materials into current semiconductor technology requires fabrication and structuring of thin films, leading to the interest in variation of the material properties with the nanoscale structure, as well as to the development of methods for their synthesis [6, 7]. In addition to reduced dimension, the thin films often show granular structure on the characteristic length scale of the order of 10 nm. Details of the grain structure contribute to the variation of the properties of both the material and the devices.

One of the most well-known multiferroic materials is the bismuth ferrite ($BiFeO_3$). It shows high critical temperatures, both for the ferroelectric ordering below 1104 K [8] and the antiferromagnetic ordering below 643 K [9]. The interest in $BiFeO_3$ stems from the possibility of having all the technologically desirable properties of multiferroics at and above the room temperature. A major obstacle for the applications of $BiFeO_3$ is the existence of relatively large leakage currents

which severely limit the electric fields that a material can sustain. The leakage currents have been explained by the existence of charge defects, for example the oxygen and bismuth vacancies [10]. Attempts at minimizing the leakage currents in $BiFeO_3$ thin films drive the interest in their electronic transport properties and their modification either by doping [11–14] or by modifying the conditions of film growth [15, 16].

The properties of multiferroic $BiFeO_3$ granular thin film strongly depend on the grain size. The Neel temperature was shown to correlate with the volume of the grains which affects the polar displacements of cations and changes in polarization [17]. The mechanical properties also depend on the grain size [18]. Therefore, the regions in proximity to the grain boundaries may play an important role in determining the material properties.

We have studied a film of an undoped, single crystallographic phase, $BiFeO_3$. The film has been produced by sol–gel spin coating. The film has shown granular structure, and we have probed the variation of the electronic properties on the spatial scale commensurate with the grain size. Our film did not have any holes and all the measured grains lied on the top of the film, and not on the substrate. The variation at probed length scale are therefore properties of the grain morphology and independent of the thickness or large-scale roughness of the film.

In our measurements, the local electric properties of the film have varied on two characteristic length scales, corresponding to the sizes of grains and boundary regions. In scanning probe measurements, we have found mild variations between the interiors of different grains when probing their band structure. On the other hand, the differences between the grain interiors and the grain boundaries have been drastic. We have measured the local electric properties of the $BiFeO_3$ film across the grain boundary, and have found that the boundary regions differ from the grain interior in the density of states, charge transport mechanism, and the absence of hysteresis in the I–V curves. Remarkably, all the measured properties have shown a hysteresis when measured in the grain interior, but there were no sings of hysteresis when probed at the boundary.

2. Experimental procedure

$BiFeO_3$ thin film was prepared via the sol–gel spin coating method. The details of preparation are presented in the supplementary material (stacks.iop.org/JPhysD/49/045309/mmedia).

Structural characterization was carried out using x-ray diffraction (XRD) with Cu–Kα radiation on a Rigaku Ultima IV diffractometer ($2\theta = 20°$–$60°$). Raman spectroscopy was used to study the vibrational properties of $BiFeO_3$ thin film. Micro-Raman spectra were collected using a Jobin Yvon T64000 spectrometer with a liquid-nitrogen-cooled CCD camera.

The morphology and phenomena at short length scales were recorded by atomic force microscopy (AFM). AFM imaging was performed using tapping mode on NT-MDT system Ntegra Prima and silicon NSG01 probes with the tip curvature radius of 6 nm. The phase lag of the cantilever oscillation was recorded simultaneously with the topography image.

We have investigated the electromechanical response of our sample by piezoresponse force microscopy (PFM). During PFM measurements, an AC bias with the amplitude of 10 V and frequency of 150 kHz has been applied between the tip and the substrate on which the $BiFeO_3$ film is grown. PFM measurements were done using TiN coated NSG01 probes with a tip curvature radius of 35 nm, a typical force constant of 5.1 N $m^{-1}$and typical resonant frequency of 150 kHz. The conductive tip was scanning the surface of the sample in contact mode while AC bias was applied to the tip. The AC bias was inducing the contraction and expansion of the sample, and these changes of the shape were monitored by the tip deflection. This local piezoelectricity of $BiFeO_3$ thin film was recorded in out-of-plane and in-plane polarization.

The local electrical conductivity of a $BiFeO_3$ film was probed by conductive atomic force microscopy (C-AFM). During C-AFM measurements, a DC bias voltage (from +2 to +6 volts) was applied between the tip and the substrate. Surface topography and current maps were obtained simultaneously by using a conducting probe in contact with the sample. The measurements were performed with the DCP20 probe of a nominal curvature radius of 50–70 nm and typical force constant of 48 N m^{-1}. In the same mode, the electrical measurements of current-voltage (I–V) characteristics were recorded in the bias voltage range from −10 V to +10 V. The I–V curves were measured using C-AFM at the points within the grain interior and at the points on the grain boundary. We have determined the band gap value of BiFeO3 film according to the same procedure as in references [20–22]. Thus, we have measured the local density of states and the local band gap in $BiFeO_3$ film using C-AFM. At each point we have repeated the measurements a few times, and therefore proved the reproducibility. Differential conductance spectra were obtained by averaging and differentiating five current-voltage curves measured on an individual grain of $BiFeO_3$ film. All AFM measurements were performed at ambient conditions (room temperature and air atmosphere).

3. Results and discussion

The crystallographic phase and structure of our sample have been determined by XRD. The XRD pattern of the $BiFeO_3$ thin film is shown in figure 1(a). The XRD peaks of $BiFeO_3$ film with a rhombohedrally distorted $BiFeO_3$ perovskite structure, belonging to the R3c space group have been indexed. No peaks originating from the secondary phase were observed. The absence of the impurity phase signal from XRD measurement does not imply that the sample itself is ultra pure. However, it does imply that there are no regions of impurity phase of appreciable size. From the Williamson–Hall plot [19], we have estimated the grain size in our film to ∼38 nm and the microstrain to ∼0.3%, as shown in figure 1(b). The diffraction peaks corresponding to the perovskite structure have been clearly observed. Figure 1(c) shows the histogram of the grain size distribution from the AFM measurement of the $BiFeO_3$ film. Raman spectrum of $BiFeO_3$ film has confirmed the rhombohedrally distorted structure without the presence

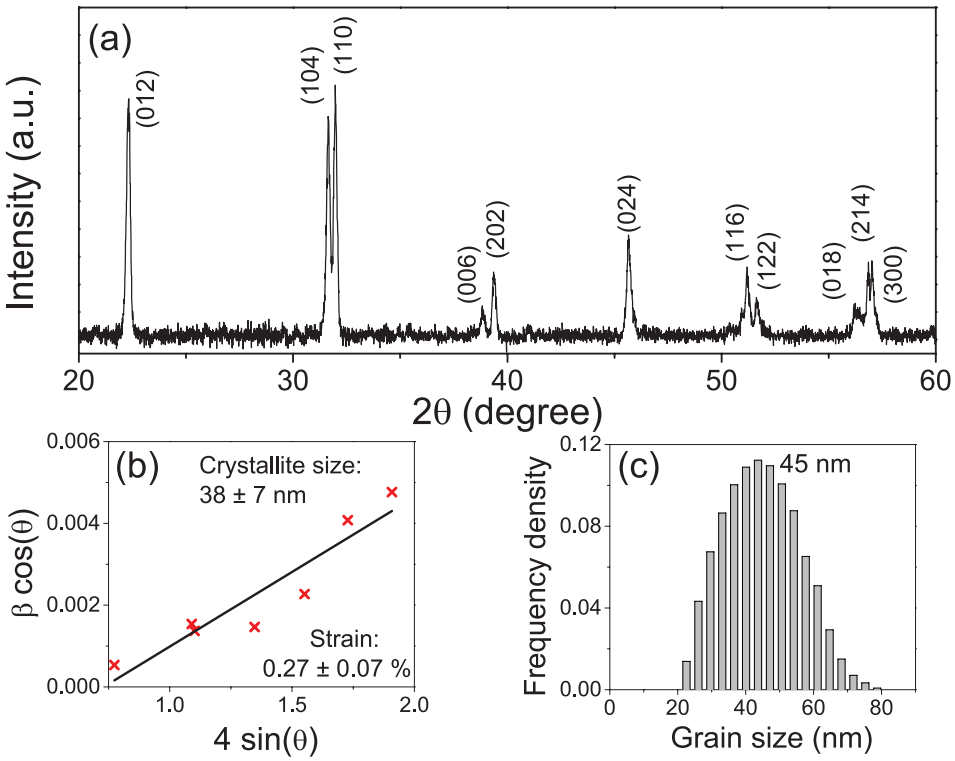

Figure 1. (a) X-ray diffraction pattern of the $BiFeO_3$ film fabricated by the sol–gel method, (b) Williamson–Hall plot for $BiFeO_3$ film with calculated crystallite size and strain, and (c) histogram of grain size distribution of $BiFeO_3$ film obtained from AFM image (see supplementary material (stacks.iop.org/JPhysD/49/045309/mmedia)).

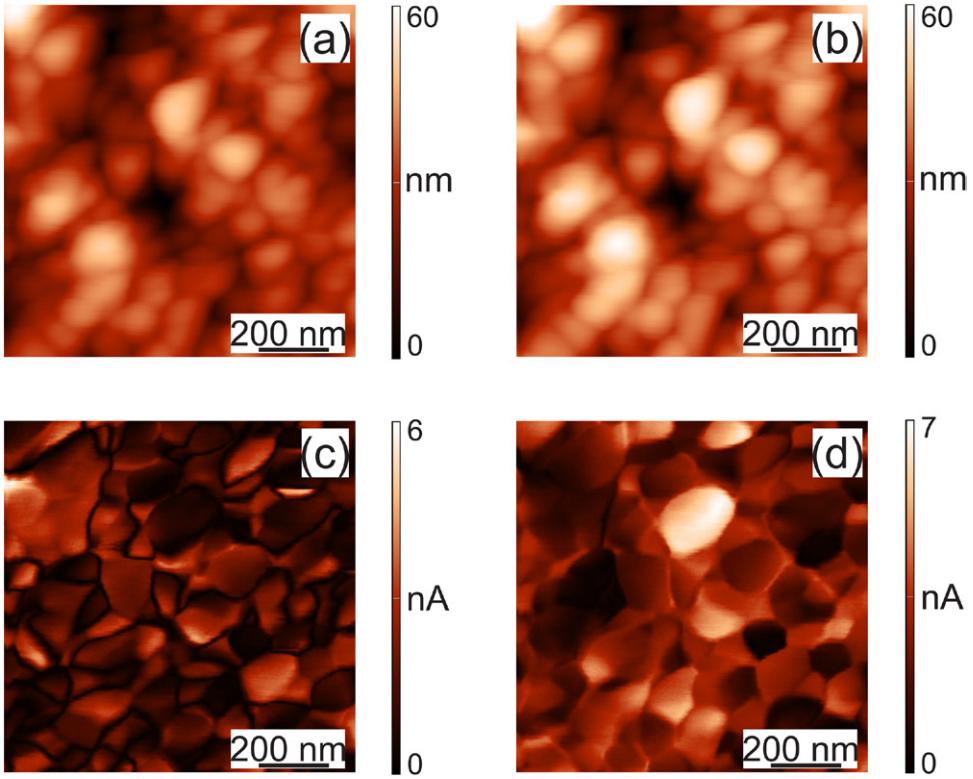

Figure 2. Topography (a) and out-of-plane PFM magnitude (c), topography (b) and in-plane PFM magnitude (d), showing the polarization components of $BiFeO_3$ film. The grains, visible on the topography images (a) and (b), correspond to the ferroelectric domain captured by the PFM magnitudes in (c) and (d).

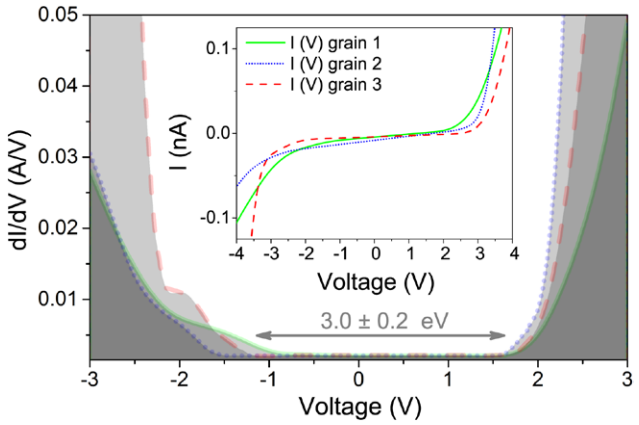

Figure 3. Representative differential conductance spectra measured on interior points of three different grains on $BiFeO_3$ film. Arrow shows the averaged band gap value. The corresponding I–V curves are shown in the inset in a wider voltage range, from −4 to 4 V.

of secondary phase. Raman scattering spectrum of the $BiFeO_3$ film is presented in supplementary material (stacks.iop.org/JPhysD/49/045309/mmedia).

Ferroelectric domains occur when the minimization of the electrostatic and elastic energy favors an inhomogeneous distribution in a material with unsaturated bulk electric polarization. The domain shapes and sizes are governed by various stresses that appear in the process of thin film growth [23, 24]. The granular structure of the $BiFeO_3$ film is dictated by lattice, morphology and thermal expansion coefficient mismatch between the $BiFeO_3$ film and the substrate [25, 26], the film thickness, and the temperature [27]. We have measured the polarization domains in the film, and found that they change on the characteristic length scale of ∼40 nm. We have measured both the out-of-plane and the in-plane polarization, based on normal and lateral deflection of the AFM cantilevers during PFM measurements (figures 2(c) and (d)). Therefore, we have identified both the in-plane and out-of-plane polarization components. Comparison with the sample topography, figures 2(a) and (b), has shown that the domain boundaries coincide with the grain boundaries. Therefore, each grain in the film has been a single-domain particle. This kind of the domain distribution is characteristic for the small grains, while larger grains generically show a multi-domain structure [24]. In our film, we could not identify any multi-domain grains.

Knowledge of the charge transport mechanism is essential in the design of memory devices based on $BiFeO_3$ film. The granular film contains rough surfaces that cause an inhomogeneous behavior of conductivity [28]. We have investigated the spatial distribution of the density of states and of the band gap. We have achieved high resolution by measuring the I–V characteristics locally using C-AFM, and by extracting the corresponding differential conductances.

Figure 3 shows the characteristic spectra of local differential conductance as a function of voltage. The measurements have been performed on interior points of different grains, far away from any boundaries with the neighboring grains. The density of states has varied slightly between the grains. The estimated band gap is $E_g = 3.0 \pm 0.2$ eV, in agreement with the optical measurements [29–31]. Conduction at negative bias

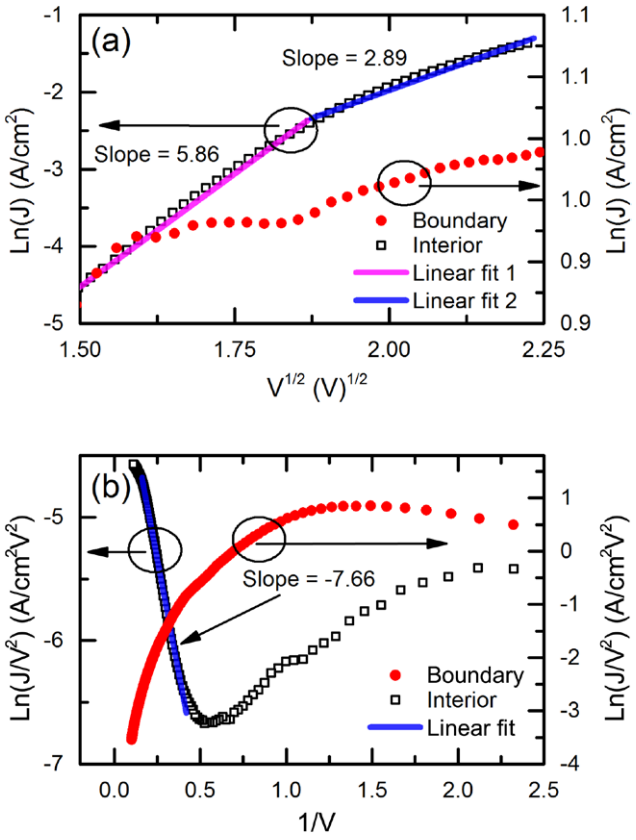

Figure 4. (a) Schottky thermionic emission plot, $\ln(J)$ versus $V^{1/2}$ and (b) Fowler–Nordheim plot, $\ln(J/V^2)$ versus $1/V$ at positive bias curves of the grain interior (left scale) and grain boundary (right scale) of the $BiFeO_3$ film.

voltages corresponds to the states in the valence band, while the conduction at the positive bias corresponds to the states in the conduction band. The flat plateau around zero voltage represents the band gap. These results show that the grain interiors are very similar, even though the grain's immediate surroundings vary. Therefore, we claim that the properties at the length scale of the grain size are not influenced by the distant regions of the film, and therefore should not depend on the film thickness, as long as it is larger than the grain dimension.

We have observed a difference between the grain boundary and the grain interior in the local measurements of the current as a function of bias voltage. In the resulting I–V curves the conduction has been higher at the boundary. Conduction through semiconductor heterostructures is well researched, and various transport mechanisms have been proposed and observed [32, 33]. In our case, the distribution of electric polarization (see figure 2), and the typical gap sizes (see figure 3), suggest that the interior of the grain behaves as a semiconductor of fairly large band gap, ∼ 3 eV. In the grain interior, the transport has been consistent with the tunneling through a barrier, either via Schottky or Fowler–Nordheim mechanism [32–34]. We have fitted the I–V curves in the spatial region of the grain interior, and in the voltage region $V > 2$ V, to the predictions of the tunneling transport theory. Up to $V \approx 5$ V, the Schottky mechanism of thermal excitations across the barrier explains the observed behavior. At larger voltages,

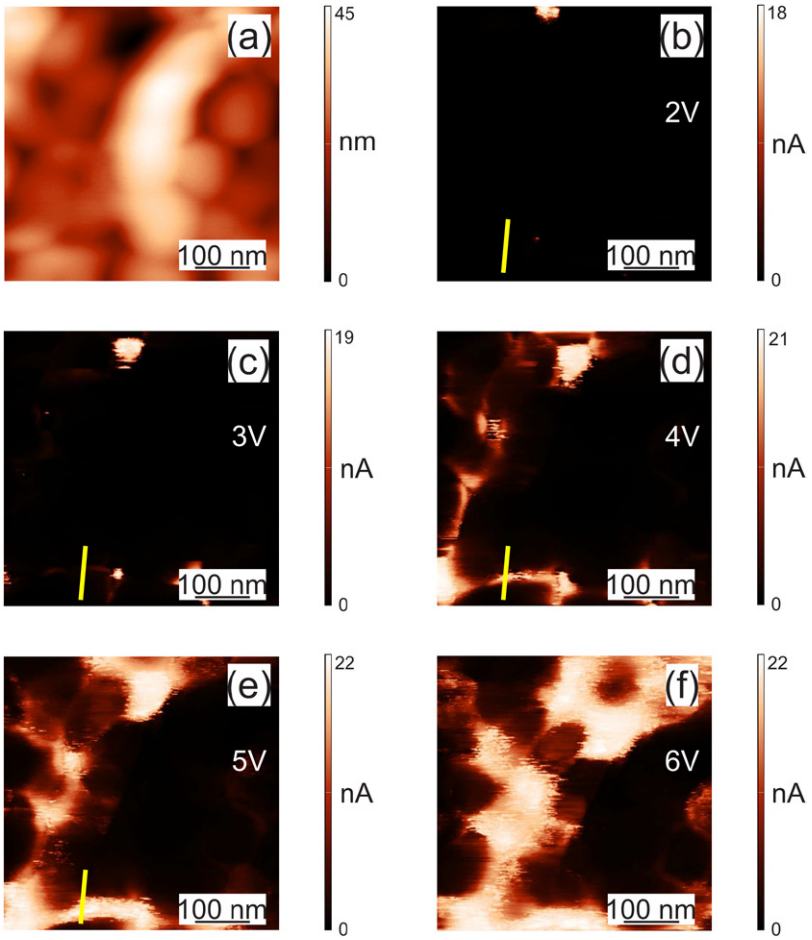

Figure 5. (a) Topography and ((b)–(f)) current maps (C-AFM images) according to bias voltages $V = 2$, 3, 4, 5, 6 V respectively. Bright regions means higher current. Notice the enhanced conductivity at grain boundaries and no conductivity regions in the grains interior. Bright line indicates the places between two grains where we have measured the current as a function of the position (shown in figure 6).

the results are consistent with the Fowler–Nordheim mechanism. Figure 4(a) shows the plot of $\ln(J)$ versus $V^{1/2}$ measured at various points in the $BiFeO_3$ film in the voltage range from 2 to 5 V. For the leakage current governed by the tunneling, $\ln(J/V^2)$ versus $1/V$ plot shows linearity for bias voltage well bellow the gap, i.e. $V < 2$ V (figure 4(b)), as we have observed in our film. At low fields, $V < 1.5$ V the grain interior has shown a plain Ohmic behavior (see supplementary material (stacks.iop.org/JPhysD/49/045309/mmedia)). As opposed to the grain interior, I–V curves of the grain boundary have not followed any standard transport model.

The local current distributions and the I–V characteristic of the $BiFeO_3$ film have been studied by the C-AFM. Current maps (C-AFM images) and topography images have been probed in the same spatial region of the sample. In C-AFM images, figure 5, the bright parts are conducting regions, while the dark regions are non-conducting. From the morphological and PFM measurements we have found that the $BiFeO_3$ film is inhomogeneous. A difference in electric transport properties between the grain interior and its boundary can appear for several reasons. Due to the different crystal orientation of the grains and the possible strain between the grains, the polarizations of neighboring grains are not equal and generically point in different directions. Furthermore, different polarizations

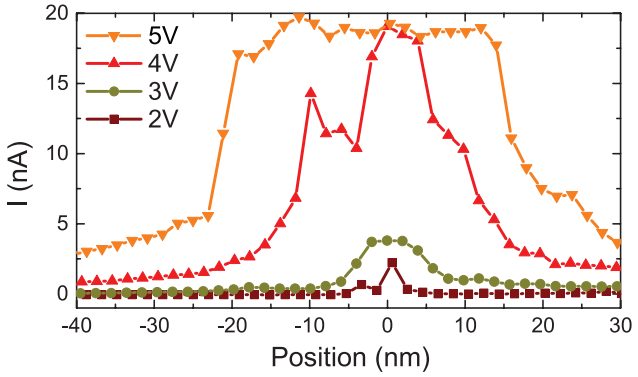

Figure 6. The current profiles of cross-sectional analysis along the bright solid line in figure 5.

of the neighboring grains cause strong electric fields in the region of the boundary between the grains. A similar phenomenon was observed in $HoMnO_3$ [35].

Our measurements have demonstrated that the local conduction pathways of the $BiFeO_3$ film coincide with the grain boundaries, while the interior of the grains remain insulating [36], as indicated in figure 5, and consistent with the measurements on the interior points of various grains, presented in figure 3. The charge transport of $BiFeO_3$ film has been

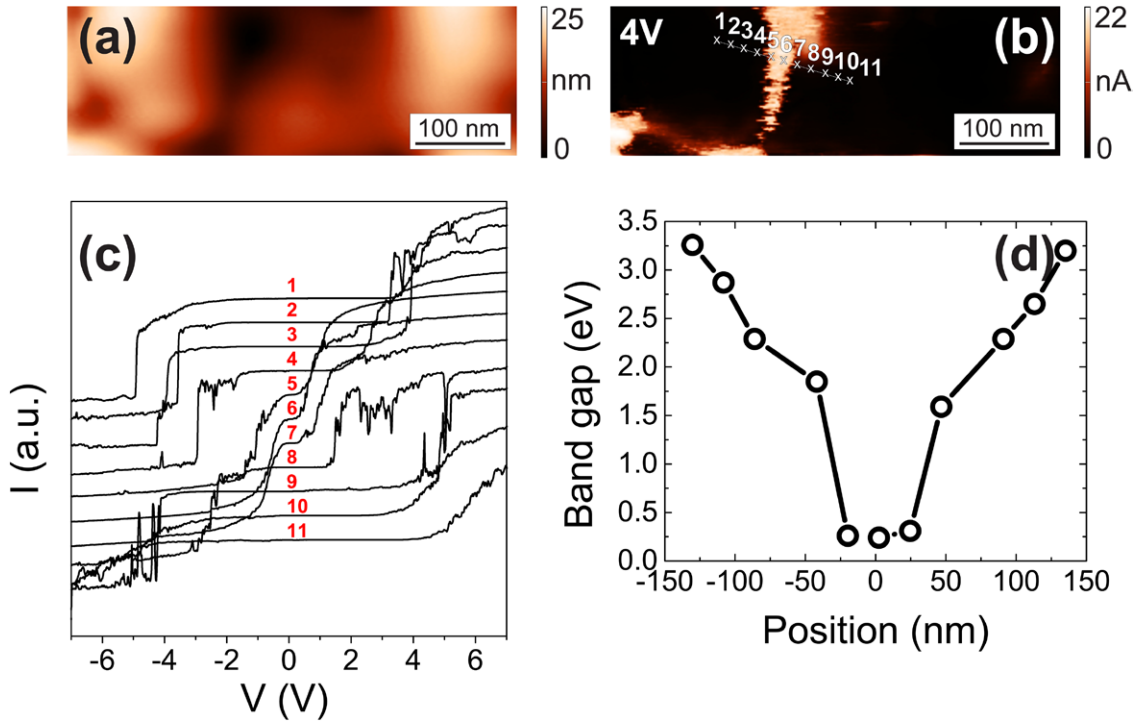

Figure 7. (a) Topography, (b) C-AFM image with line across the grain boundary, (c) I–V characteristics for 11-points across grain boundary and (d) behavior of the band gap as a function of the position of the grain boundary.

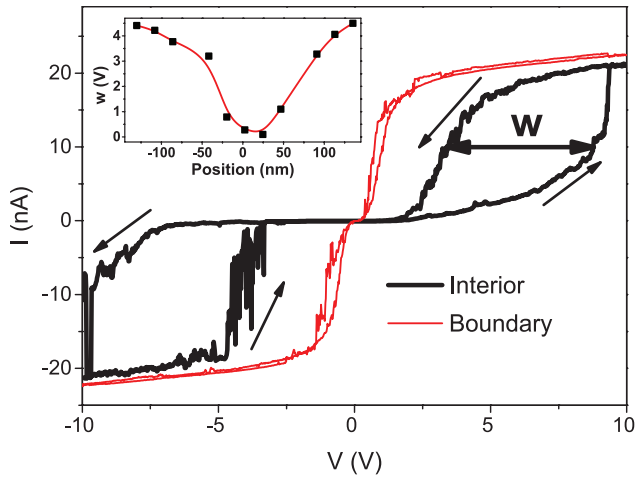

Figure 8. Dramatic I–V hysteresis in the grain interior (heavy line) and the absence of the hysteresis in the grain boundaries (thin line) of the $BiFeO_3$ film. In the inset, the width of the hysteresis curve (w) is shown as a function of the position across the grain boundary. Solid line in the inset is a guide to the eye.

investigated at different applied bias voltages, both slightly smaller and larger than the band gap. Topography image (figure 5(a)) and the corresponding C-AFM images at bias voltage ranged from 2 to 6 V (figures 5(b)–(f)) have confirmed high correlation between the granular structure of the film and the shape of the conduction pathways. Under low bias voltages, narrow charge transport pathways form (figures 5(b) and (c)) at the places that are low in the topographic image of the film, and are barely visible. As the bias voltage increases, both the width of the conduction pathways and the intensity of the current that flows through them increases.

The evolution of the conduction pathways with the increasing bias voltage is shown in figure 6. The current through the film has been measured at the points that lie both near the grain boundaries and deep within the grain, along line that crosses the grain boundary at the right angle. The measurements were repeated for various bias voltages. The geometry is indicated by the bright solid line in figures 5(b)–(e). With the increase of the bias voltage, the conduction path broadens. Initial broadening is slow, the currents are weak, and the path is narrow as long as the bias voltage is below the band gap. At the bias voltage of about 4 V, which is larger than the band gap, the path suddenly broadens dramatically, and the local currents increase. At such high biases, the interior of the grain also begins to conduct. Similar behavior was previously observed in doped $BiFeO_3$ film [28].

In order to better understand the microscopic charge transport process in the grain boundaries, we have measured the I–V characteristics across the grain boundary and observed the changes in the conduction. A pair of particularly large grains and the boundary between them have been chosen, so that we can reach a relatively high spatial resolution when compared to the dimensions of the grains. Figure 7 shows topography (a) and C-AFM image (b) under the 4 V bias with a line across the grain boundary and 11 points on it. The I–V characteristics taken at these points are shown in figure 7(c). As a general trend, the grain boundaries have almost Ohmic behavior, but at the point in the grain interior, the I–V characteristics are typical of semiconductors. Figure 7(d) shows the evolution of the band gap across the grain boundary. We have found the band gap of about 3.2 eV on the grain interior, consistent with the measurements on other grains, see figure 3. As the probe approaches the boundary, the band gap narrows down. At the

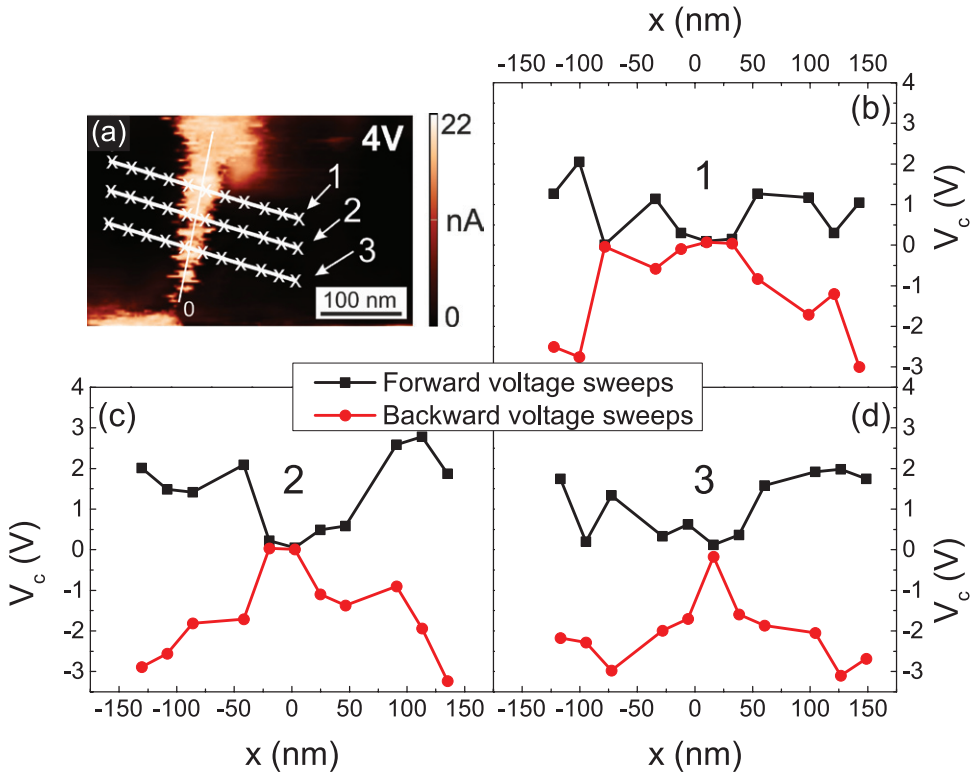

Figure 9. (a) C-AFM image with 3 lines across grain boundary and ((b)–(d)) center of band gap across lines 1, 2, and 3 in the C-AFM image. Solid lines are a guide to the eye.

three points located at the grain boundary (5, 6, and 7) the band gap is very narrow, and the material behaves similarly to a conductor. The fact that we do not find the band gap to be constant across the sample suggests that, at the level of single grains, the film is not homogeneous with well-defined and constant band structure throughout the sample.

The hysteretic dependence of polarization on the external electric field is well known in bulk ferroelectric $BiFeO_3$. The hysteretic phenomena are necessary for the applications of $BiFeO_3$ films in memory devices. Reorganization of charge associated with the variation of electric polarization causes strong internal fields in the sample, and we may expect similar hysteretic behavior in the quantities related to the charge transport. The I–V characteristics and the phenomenon of resistive switching in polycrystalline thin films shows some signatures of the hysteresis [37–39]. However, the hysteresis of electric polarization in the electric field exists only in insulators, whereas the conductors cannot support the electric fields in the interior. We have studied the local hysteresis in the I–V curves, and have probed both the region where the grain is insulating, i.e. the grain interior, and the region where the grain is conductive, i.e. the grain boundary. We have defined the hysteresis width, w, as the difference of voltage that produces a 10 nA current in forward- and backward voltage sweep, see figure 8. The hysteresis width vanishes at the grain boundary, and turns on in the interior with the characteristic length scale of 50 nm, see inset of figure 8. The measured points are presented in figure 7(b). Figure 8 shows the I–V curves in the forward and backward sweep at the grain interior (thick line) and at the grain boundary (thin line). Note that the typical grain diameter is 40 nm.

The bulk $BiFeO_3$ shows both the ferroelectric and the antiferromagnetic order. Both orders are characterized by hysteretic response to external fields. We have found the hysteresis in conductivity in the interior of the grain, but not at the grain boundary (see figure 8). Another property of the grain that can be studied locally is the density of states. We have measured the local density of states across the grain boundary and have found, again, the hysteretic behavior within the grain interior, but not on the boundary. We have chosen the center of the band gap as a representative quantity that describes the band structure. The definition of the center of band gap is illustrated graphically in the supplementary material (stacks.iop.org/JPhysD/49/045309/mmedia). In a series of C-AFM measurements, we have measured the density of states in a forward- and backward voltage sweeps at a set of points that extends across the grain boundary.

Figure 9(a) shows a C-AFM image of grain boundary. Within this region, we have recorded 11 I–V curves through three different lines (see picture). Three representative lines (1–3) across the leakage current pathways of different widths are selected for detailed study of the local density of states. The center of flat plateau in the I–V characteristics is defined as the center of the band gap. Figures 9(b)–(d) show the potential at the band gap centers, V_c, across marked lines 1–3 in figure 9(a).

The density of states is hysteretic, and the center of the band gap is hysteretic within the grain, but not within the boundary layer, see figure 9. The motion of the center of the band gap, V_c, as the probe position x moves in real space across the grain boundary is more pronounced in the backward voltage sweeps,

and less in the forward ones. The local hysteresis is manifested by the difference in the positions of the band gap centers as measured in the forward- and backward voltage sweeps while the position of the probe within the sample is kept fixed. Comparison of the $V_c(x)$ curves from the figures 9(b)–(d) with the image of conductivity obtained by C-AFM shows that the narrower boundary region as defined by conductivity (figure 9(a)) also implies a narrower region with the absent hysteresis in $V_c(x)$ (figures 9(b)–(d)). Note, however that the boundary region as would naively be defined from $I(V)$ is much narrower than the absence of hysteresis would imply.

In thin $BiFeO_3$ films, a similar shift of the band gap was observed at the ferroelectric domain boundaries [40]. Discontinuity in polarization and the consequent charge accumulation on the surface causes potential discontinuity and moves the band gap. Such a potential difference should enhance the electrical conductivity by causing carriers in the material to accumulate at the domain wall to screen the polarization discontinuity [41, 42]. In our sample, the grains are single domains, see above, and a similar charge accumulation appears at the boundaries between the grains.

4. Conclusions

We have observed a difference in electrical properties between the grain interior and the grain boundary in $BiFeO_3$ thin film obtained by sol–gel spin coating process. Leakage current was more pronounced at the grain boundaries. The onset of large leakage current with the increasing bias voltage happens as the region of large conductivity expands from the grain boundaries towards the grain interiors. The leakage mechanism in grain interior have been identified with Schottky and Fowler–Nordheim processes, while the leakage current through the grain boundaries does not appear to be dominated by any standard mechanism of conduction. In the measurement with the local probes, we have also found that the band gap varies slightly among the different grains, but varies strongly between the grain boundary and the grain interior. In the grain interior, we have observed hysteresis in various properties of the material connected to the charge transport. The shape of the density of states is itself hysteretic. As a consequence, the conductivity as a function of slowly varying voltage is also hysteretic. As opposed to the grain interior, no hysteresis was observed with the local probe at the grain boundary.

Acknowledgments

This work was financially supported by the Ministry of Education, Science and Technological Development of the Republic of Serbia under the projects OI171032, OI171005, III45018 and SNF through SCOPES IZ73Z0152500.

References

[1] Sergienko I A and Dagotto E 2006 Role of the Dzyaloshinskii-Moriya interaction in multiferroic perovskites *Phys. Rev.* B **73** 094434

[2] Cheong S W and Mostovoy M 2007 Multiferroics: a magnetic twist for ferroelectricity *Nat. Mater.* **6** 13

[3] Picozzi S, Yamauchi K, Sergienko I A, Sen C, Sanyal B and Dagotto E 2008 Microscopic mechanisms for improper ferroelectricity in multiferroic perovskites: a theoretical review *J. Phys.: Condens. Matter* **20** 434208

[4] Catalan G and Scott J F 2009 Physics and applications of bismuth ferrite *Adv. Mater.* **21** 2463

[5] Ramesh R and Spaldin N A 2007 Multiferroics: progress and prospects in thin films *Nat. Mater.* **6** 21

[6] Ren X R, Tan G Q, Miao H Y and Li Z Y 2012 Controllability study on the preparation of pure phase $BiFeO_3$ thin films by liquid phase self-assembled method *Appl. Surf. Sci.* **258** 8040

[7] Schwartz R W 1997 Chemical solution deposition of perovskite thin films *Chem. Mater.* **9** 2325

[8] Roginskaya Y E, Tomashpol'Skiĭ Y Y, Venevtsev Y N, Petrov V M and Zhdanov G S 1966 Nature of dielectric and magnetic properties of $BiFeO_3$ *Sov. Phys.—JETP* **23** 47

[9] Kiselev S V, Ozerov R P and Zhdanov G S 1963 Detection of magnetic order in ferroelectric $BiFeO_3$ by neutron diffraction *Sov. Phys.—Dokl.* **7** 742

[10] Wang Y and Nan C W 2006 Enhanced ferroelectricity in Ti-doped multiferroic $BiFeO_3$ thin films *Appl. Phys. Lett.* **89** 052903

[11] Mao W *et al* 2014 Effect of Ln (Ln = La, Pr) and Co co-doped on the magnetic and ferroelectric properties of $BiFeO_3$ nanoparticles *J. Alloys Compd.* **584** 520

[12] Pradhan S K and Roul B K 2011 Effect of Gd doping on structural, electrical and magnetic properties of $BiFeO_3$ electroceramic *J. Phys. Chem. Solids* **72** 1180

[13] Liu J, Li M, Pei L, Wang J, Yu B, Wang X and Zhao X 2010 Structural and multiferroic properties of the Ce-doped $BiFeO_3$ thin films *J. Alloys Compd.* **493** 544

[14] Qi X, Dho J, Tomov R, Blamire M G and MacManus-Driscoll J L 2005 Greatly reduced leakage current and conduction mechanism in aliovalent-ion-doped $BiFeO_3$ *Appl. Phys. Lett.* **86** 062903

[15] Jang H W *et al* 2009 Domain engineering for enhanced ferroelectric properties of epitaxial (0 0 1) $BiFeO_3$ thin films *Adv. Mater.* **21** 817

[16] Lu H X, Zhao J L, Sun J R, Wang J and Shen B G 2011 Ferroelectric domain structure of the $BiFeO_3$ film grown on different substrates *Physics* B **406** 305

[17] Selbach S M, Tybell T, Einarsrud M A and Grande T 2007 Size-dependent properties of multiferroic $BiFeO_3$ nanoparticles *Chem. Mater.* **19** 6478

[18] Armstrong R W 1970 The influence of polycrystal grain size on several mechanical properties of materials *Metall. Mater. Trans.* B **1** 1169

[19] Williamson G K and Hall W H 1953 X-ray line broadening from filed aluminium and wolfram *Acta Metall. Mater.* **1** 22

[20] Alperson B, Cohen S, Rubinstein I and Hodes G 1995 Room-temperature conductance spectroscopy of CdSe quantum dots using a modified scanning force microscope *Phys. Rev.* B **52** R17017

[21] Alperson B, Rubinstein I and Hodes G 2001 Identification of surface states on individual CdSe quantum dots by room-temperature conductance spectroscopy *Phys. Rev.* B **63** 081303

[22] Kwon S, Lee S J, Kim S M, Lee Y, Song H and Park J Y 2015 Probing the nanoscale Schottky barrier of metal/semiconductor interfaces of Pt/CdSe/Pt nanodumbbells by conductive-probe atomic force microscopy *Nanoscale* **7** 12297

[23] Johann F, Morelli A, Biggemann D, Arredondo M and Vrejoiu I 2011 Epitaxial strain and electric boundary condition effects on the structural and ferroelectric properties of $BiFeO_3$ films *Phys. Rev.* B **84** 094105

[24] Castillo M E, Shvartsman V V, Gobeljic D, Gao Y, Landers J, Wende H and Lupascu D C 2013 Effect of particle size on ferroelectric and magnetic properties of $BiFeO_3$ nanopowders *Nanotechnology* **24** 355701
[25] Speck J S and Pompe W 1994 Domain configurations due to multiple misfit relaxation mechanisms in epitaxial ferroelectric thin films. I. Theory *J. Appl. Phys.* **76** 466
[26] Speck J S, Seifert A, Pompe W and Ramesh R 1994 Domain configurations due to multiple misfit relaxation mechanisms in epitaxial ferroelectric thin films. II. Experimental verification and implications *J. Appl. Phys.* **76** 477
[27] Kwak B S, Erbil A, Budai J D, Chisholm M F, Boatner L A and Wilkens B J 1994 Domain formation and strain relaxation in epitaxial ferroelectric heterostructures *Phys. Rev.* B **49** 14865
[28] Zhou M X, Chen B, Sun H B, Wan J G, Li Z W, Liu J M, Song F Q and Wang G H 2013 Local electrical conduction in polycrystalline La-doped $BiFeO_3$ thin films *Nanotechnology* **24** 225702
[29] Allibe J *et al* 2010 Optical properties of integrated multiferroic $BiFeO_3$ thin films for microwave applications *Appl. Phys. Lett.* **96** 182902
[30] Kumar A *et al* 2008 Linear and nonlinear optical properties of $BiFeO_3$ *Appl. Phys. Lett.* **92** 121915
[31] Chen X, Zhang H, Wang T, Wang F and Shi W 2012 Optical and photoluminescence properties of $BiFeO_3$ thin films grown on ITO-coated glass substrates by chemical solution deposition *Phys. Status Solidi* A **209** 1456
[32] Yan F, Lai M O, Lu L and Zhu T J 2011 Variation of leakage mechanism and potential barrier in La and Ru co-doped $BiFeO_3$ thin films *J. Phys. D: Appl. Phys.* **44** 435302
[33] Chen Z, He L, Zhang F, Jiang J, Meng J, Zhao B and Jiang A 2013 The conduction mechanism of large on/off ferroelectric diode currents in epitaxial (1 1 1) $BiFeO_3$ thin film *J. Appl. Phys.* **113** 184106
[34] Chiu F C 2014 A review on conduction mechanisms in dielectric films *Adv. Mater. Sci. Eng.* **2014** 578168
[35] Wu W, Horibe Y, Lee N, Cheong S W and Guest J R 2012 Conduction of topologically protected charged ferroelectric domain walls *Phys. Rev. Lett.* **108** 077203
[36] Cheng Z, Bin C, Xiao-Jian Z, Zheng-Hu Z, Yi-Wei L, Yuan-Fu C, Qing-Feng Z and Run-Wei L 2011 Local leakage current behaviours of $BiFeO_3$ films *Chin. Phys.* B **20** 117701
[37] Yang C H *et al* 2009 Electric modulation of conduction in multiferroic Ca-doped $BiFeO_3$ films *Nat. Mater.* **8** 485
[38] Yin K, Li M, Liu Y, He C, Zhuge F, Chen B, Lu W, Pan X and Li R W 2010 Resistance switching in polycrystalline $BiFeO_3$ thin films *Appl. Phys. Lett.* **97** 042101
[39] Wang C, Jin K J, Xu Z T, Wang L, Ge C, Lu H B, Guo H Z, He M and Yang G Z 2011 Switchable diode effect and ferroelectric resistive switching in epitaxial $BiFeO_3$ thin films *Appl. Phys. Lett.* **98** 192901
[40] Seidel J *et al* 2010 Domain wall conductivity in la-doped $BiFeO_3$ *Phys. Rev. Lett.* **105** 197603
[41] Seidel J *et al* 2009 Conduction at domain walls in oxide multiferroics *Nat. Mater.* **8** 229
[42] Maksymovych P, Seidel J, Chu Y H, Wu P, Baddorf A P, Chen L Q, Kalinin S V and Ramesh R 2011 Dynamic conductivity of ferroelectric domain walls in $BiFeO_3$ *Nano Lett.* **11** 1906

NanoScience and Technology

Juan Bartolomé
Fernando Luis
Julio F. Fernández *Editors*

Molecular Magnets

Physics and Applications

Springer

Editors
Juan Bartolomé
Institute of Material Science of Aragón and
Department of Condensed Matter Physics
CSIC–University of Zaragoza
Zaragoza, Spain

Julio F. Fernández
Institute of Material Science of Aragón and
Department of Condensed Matter Physics
CSIC–University of Zaragoza
Zaragoza, Spain

Fernando Luis
Institute of Material Science of Aragón and
Department of Condensed Matter Physics
CSIC–University of Zaragoza
Zaragoza, Spain

ISSN 1434-4904
NanoScience and Technology
ISBN 978-3-642-40608-9
DOI 10.1007/978-3-642-40609-6
Springer Heidelberg New York Dordrecht London

ISSN 2197-7127 (electronic)

ISBN 978-3-642-40609-6 (eBook)

Contents

Part II Beyond Single Molecules

Chapter 11
Molecular Magnets for Quantum Information Processing

Kevin van Hoogdalem, Dimitrije Stepanenko, and Daniel Loss

Abstract In this chapter we will examine the possibility of utilizing molecular magnets for quantum information processing purposes. We start by giving a brief introduction into quantum computing, and highlight the fundamental differences between classical- and quantum computing. We will introduce the five DiVincenzo criteria for successful physical implementation of a quantum computer, and will use these criteria as a guideline for the remainder of the chapter. We will discuss how one can utilize the spin degrees of freedom in molecular magnets for quantum computation, and introduce the associated ways of controlling the state of the qubit. In this part we will focus mainly on the spin-electric effect, which makes it possible to control the quantum states of spin in molecular magnets by electric means. We will discuss ways to couple the quantum state of two molecular magnets. Next, we will identify and discuss the different decoherence mechanisms that play a role in molecular magnets. We will show that one of the advantages of using molecular magnets as qubits is that it is possible to use degrees of freedom that are more robust against decoherence than those in more traditional qubits. We briefly discuss preparation and read-out of qubit states. Finally, we discuss a proposal to implement Grover's algorithm using molecular magnets.

11.1 Introduction

Conceptually, a computer is a device that takes an input and manipulates it using a predetermined set of deterministic rules to compute a certain output. Both input and output are defined in terms of bits, classical physical systems which can be in one of two different states. These states are typically denoted 0 and 1. The set of rules that a computer uses for a computation, also named the algorithm, can be described by a set of gates. A simple example of a gate is the one-bit NOT-gate, which gives a 1 as output when the input is 0, and vice versa. An example of a two-bit

K. van Hoogdalem · D. Stepanenko · D. Loss (✉)
Department of Physics, University of Basel, Klingelbergstrasse 82, 4056 Basel, Switzerland
e-mail: daniel.loss@unibas.ch

K. van Hoogdalem
e-mail: kevin.vanhoogdalem@unibas.ch

J. Bartolomé et al. (eds.), *Molecular Magnets*, NanoScience and Technology,
DOI 10.1007/978-3-642-40609-6_11,

gate is the NAND-gate, which gives a 0 as output only if both the input bits are 1, and yields a 1 otherwise. Interestingly, it can be shown that any classical algorithm can be implemented using a combination of NAND-gates only. However, this completeness theorem does not state anything about the time in which a certain problem can be solved. Instead, such questions belong to the field of computational complexity theory [1]. A large class of problems, called NP, contains all the problems for which a candidate solution can be checked in polynomial time. In contrast, the class of problems that can be solved in polynomial time is called P. Whether P is a strict subset of NP is one of the great open problems in mathematics. It is widely believed that there are problems in the difference between P and NP. Some of the candidates were shown to be solvable using a quantum computer, but an efficient solution on a classical computer is unknown. This inability of a classical computer to solve certain problems efficiently is one of the main driving forces behind the study of quantum computation. Heuristically one might argue that, since classical computers are governed by Newtonian mechanics—which is only valid in certain limits of the underlying quantum theory—a quantum computer must have computational power which is at least the same as, and hopefully greater than, that of a classical computer [2]. Different algorithms exist that support the claim that a quantum computer is inherently more powerful than a classical computer. Among these are Deutsch-Jozsa's [3, 4], Grover's [5], and Shor's algorithm [6].

Besides being interesting from this pragmatic point of view, quantum computing is also of fundamental importance in the fields of information theory and computer science. The fact that quantum mechanics plays a role in information theory becomes clear when one realizes that abstract information is always embedded in a physical system, and is therefore governed by physical laws. This was made explicit by Deutsch [7], when he proposed a stricter version of the Church-Turing hypothesis, emphasizing its 'underlying physical assertion'. The original Church-Turing hypothesis loosely states that every function which would naturally be regarded as computable can be computed by the universal Turing machine [8, 9], and this statement can be seen as the basis underlying computer science. In a sense, a universal Turing machine is a theoretical formalization of a computer (with an infinite memory) as we described it previously. Deutsch replaces this hypothesis by his more physical Church-Turing principle: 'Every finitely realizable physical system can be perfectly simulated by a universal model computing machine operating by finite means'. He then went on to show that the universal Turing machine does not fulfill the requirements for a universal model computing machine, while the universal quantum computer, proposed in the same work, is compatible with the principle. In this way, the universal quantum computer takes the role of the universal Turing machine.

The basic unit of information in a quantum computer is a qubit [10]. Like a classical bit, a qubit is a physical two-level system, with basis states denoted by $|0\rangle$ and $|1\rangle$. Unlike a classical bit, however, a qubit is a quantum system. This makes the information stored in a qubit ultimately analog, since a qubit can be in any state $|\psi\rangle = \alpha|0\rangle + \beta|1\rangle$, with α and β complex numbers such that $|\alpha|^2 + |\beta|^2 = 1$. In a quantum computer, a gate will act linearly on a state $|\psi\rangle$, and hence in a sense on

$|0\rangle$ and $|1\rangle$ simultaneously. This quantum parallelism is one of the advantages of a quantum computer. Of course, one must keep in mind that reading out the qubit (measuring the state) collapses the quantum state into one of the basis states $|0\rangle$ or $|1\rangle$, so this parallelism cannot be used trivially. The other key advantage of using quantum computing is the fact that two qubits can be entangled, i.e. there can exist non-classical correlations between two qubits. The final important property of qubits is captured by the no-cloning theorem [11], which states that it is impossible to copy an unknown quantum state. This theorem invalidates the use of classical error-correction methods -which are typically based on redundancy, and therefore require copying of bits- for quantum computation. Instead, one has to resort to quantum error-correction codes that rely upon entanglement and measurement, but do not require an ability to copy an unknown quantum state.

Quantum mechanics dictates that the time evolution of an isolated quantum state is described by a unitary operator. This means that the action of any valid quantum gate must also be described by a unitary operator. In fact, it turns out that this is the only requirement on a valid quantum gate. Consequently, there exists a rich variety of quantum gates: Where the only non-trivial classical one-bit gate is the NOT-gate, any rotation in the one-qubit Hilbert space is a quantum gate. As an important example of a one-qubit gate that has no classical analog we mention the Hademard-gate, which transforms $|0\rangle$ into $(|0\rangle + |1\rangle)/\sqrt{2}$ and $|1\rangle$ into $(|0\rangle - |1\rangle)/\sqrt{2}$. An example of a two-qubit gate is the CNOT-gate, which acts as a NOT-gate on the second qubit when the first qubit is in the state $|1\rangle$, and does nothing otherwise. It can be shown that arbitrary single qubit rotations together with the CNOT-gate are sufficient to implement any two-qubit unitary evolution exactly [12].

After all these theoretical considerations, one might wonder what is actually required to build a physical quantum computer. The requirements have been succinctly summarized by DiVincenzo, in terms of his five DiVincenzo criteria for successful implementation of a quantum computer [2]. In order to have a functional quantum computer we need

- a collection of well-defined physical quantum two-level systems (qubits), which should be well-isolated and scalable, i.e. it should be possible to add qubits at will.
- a procedure to initialize the system in an initial state, for instance $|00\ldots0\rangle$.
- the ability to perform logic operations on the qubits, i.e. one- and two-qubit gates.
- long enough decoherence times compared to the 'clock time' of the quantum computer for quantum error correction to be efficient.
- the ability to read out the final state of the qubit.

Satisfying these criteria in a single system simultaneously has turned out to be quite a tour de force. Although tremendous progress -both theoretical and experimental- towards completion of this goal has been made in a wide variety of different areas of solid state physics, it is at this point not clear which system will turn out to be most suitable. Of all the systems that have been proposed as a basis for qubit, we mention here quantum dots [13, 14], cold trapped ions [15], cavity quantum electrodynamics [14, 16], bulk nuclear magnetic resonance [17], low-capacitance

Josephson junctions [18], donor atoms [19, 20], linear optics [21], color centers in diamond [22–24], carbon nanotubes [25], nanowires [26], and lastly the topic of this chapter: Molecular magnets [27–32].

11.2 Encoding of Qubits in Molecular Magnets

We have seen that information in a quantum computer must be encoded in qubits, i.e. well-defined physical quantum two-level systems. Probably the first candidate for a qubit that comes to mind is a single spin in for example an atom. However, experimentally it would be very challenging to control this single spin, since the length scale on which this control would have to take place is prohibitively small. On the other side of the spectrum, solid state implementations of qubits such as Ref. [13] require fields on the scale of several tens to hundreds of nanometers only, making control of the state easier (though still very hard). However, with the increased size we pay the price of additional sources of decoherence, and a huge effort has been made in recent years to combat these sources. For molecular magnets, the requirements on the spatial scale on which control has to be possible are loosened with respect to those for a single spin, because the typical size of such systems is relatively large. However, molecular magnets are still small as compared to other solid states implementations of qubits. This fact, as well as the possibility of chemically engineering molecular magnets with a wide variety of properties, may make one hopeful that sources of decoherence in molecular magnets can be suppressed. Indeed, we will show later that such suppression is possible by choosing the degree of freedom that encodes the qubit wisely.

On the other hand, since molecular magnets have a complex chemical structure containing many interacting magnetic atoms, it is not a priori clear that it will be possible to identify a well-separated, stable, and easily controllable two-level subspace in the spectrum. As we will show next, the fact that this does in fact turn out to be possible is due to the high symmetry of the molecule and the existence of well-separated energy scales. We have seen in previous chapters that molecular magnets can—to a very good approximation—be described by a collection of coupled spins. The low-energy multiplet of the system is then described by a spin-multiplet with fixed total spin, separated from excited states on an energy scale set by the exchange interaction. This low-energy multiplet has either maximal total spin for ferromagnetically coupled individual spins, or minimal total spin for antiferromagnetically coupled spins. In the latter case, the details of the ground state are then determined by the symmetry of the molecule, and frustration can play an important role.

The first requirement which has to be fulfilled by any qubit-candidate is that the physical system has to show genuine quantum behavior. Quantum behavior of the spin state in molecular magnets has been shown in experiments on quantum tunneling of magnetization [33–40], and shows up in hysteresis curves of ferromagnetic (although similar effects are predicted to occur in anitferromagnetic systems [41, 42]) molecular magnets with large spin and high anisotropy barrier [36, 37, 43–45]. In the absence of external fields, the barrier due to the anisotropy lifts the de-

generacy between states with different magnetization, and leads to the existence of long-lived spin states. Transitions between different spin states can be driven in a coherent manner, and manifest themselves as stepwise changes in the magnetization. The fact that the transitions show interference between transition paths and Berry phase effects are a signature of their coherent nature [46–52].

Quantum computing in antiferromagnetically coupled spin clusters was studied in Ref. [29]. In the simplest cases of a spin chain or a bipartite lattice with an odd number of spins the degenerate ground state is a spin doublet with effective total spin $1/2$. The total spin can be controlled by an applied magnetic field just as a single spin can, and exchange interaction between two clusters can be introduced by coupling single spins in the two different clusters. A downside of using a collection of spins is that generally decoherence increases with number of spins, unless one manages to encode the qubit in a state which is protected due to symmetry, something we will come back to later. In Ref. [30], Cr-based AFM molecular rings, and specifically Cr_7Ni, were proposed as suitable qubit candidates.

An interesting way of encoding a qubit is offered by geometrically frustrated molecules [32, 53]. Exemplary molecules that display geometric frustration are antiferromagnetic spin rings with an odd number of spins. The simplest example of such a system is given by an equilateral triangular molecule with a spin-$1/2$ particle at each vertex, such as is for instance realized to a good approximation in Cu_3 (we will use Cu_3 as an abbreviation for the molecule $Na_9[Cu_3Na_3(H_2O)_9(\alpha\text{-}AsW_9O_{33})_2] \cdot 26H_2O$) (see Ref. [54]). Spin rings (of which the spin triangle is the simplest non-trivial example) in general are described by the Heisenberg Hamiltonian with Dzyaloshinskii-Moriya interaction

$$H_0 = \sum_{i=1}^{N} J_{i,i+1}\mathbf{S}_i \cdot \mathbf{S}_{i+1} + \mathbf{D}_{i,i+1} \cdot (\mathbf{S}_i \times \mathbf{S}_{i+1}). \tag{11.1}$$

Here, N is the number of spins in the ring, and $\mathbf{S}_{N+1} = \mathbf{S}_1$. For the triangular molecular magnet $N = 3$. Furthermore, the fact that the point group symmetry of the triangular molecule is D_{3h} imposes the constraints $J_{i,i+1} = J$ and $\mathbf{D}_{i,i+1} = D\hat{\mathbf{z}}$ on the parameters of the Hamiltonian of an planar molecule. Since we are considering antiferromagnetic systems, J is positive. In a Cu_3 molecule, $|J|/k_B \sim 5$ K and $|D|/k_B \sim 0.5$ K. Due to this separation of energy scales, and in the absence of strong magnetic- or electric fields, the Hilbert space containing the 8 eigenstates of the triangular molecule can be split up in a high-energy quadruplet with total spin $\mathbf{S} = 3/2$ and a low-energy quadruplet with total spin $\mathbf{S} = 1/2$. The splitting between the two subspaces is $3J/2$.

In the absence of Dzyaloshinskii-Moriya interaction the low-energy subspace is fourfold degenerate. The eigenstates are given by

$$|1/2, \pm 1\rangle = \frac{1}{\sqrt{3}} \sum_{j=0}^{2} e^{\pm i2\pi j/3} C_3^j |\uparrow\downarrow\downarrow\rangle, \tag{11.2}$$

and $|-1/2, \pm 1\rangle$. The latter states are also given by (11.2) but with all the spins flipped. These states are thusly labeled as $|m_S, m_C\rangle$, with m_S the quantum number

belonging to the z projection of the total spin of the triangle, and m_C the z projection of the chirality of the molecular magnet. The chirality operator $\mathbf{C}$ has components

$$\begin{aligned} C_x &= -\frac{2}{3}[\mathbf{S}_1 \cdot \mathbf{S}_2 - 2\mathbf{S}_2 \cdot \mathbf{S}_3 + \mathbf{S}_3 \cdot \mathbf{S}_1], \\ C_y &= \frac{2}{\sqrt{3}}[\mathbf{S}_1 \cdot \mathbf{S}_2 - \mathbf{S}_3 \cdot \mathbf{S}_1], \\ C_z &= \frac{4}{\sqrt{3}}\mathbf{S}_1 \cdot [\mathbf{S}_2 \times \mathbf{S}_3]. \end{aligned} \tag{11.3}$$

The chirality contains information about the relative orientation of the spins that make up the molecule. Like the components of the total spin operator, the components of the chirality operator obey angular momentum commutation relations. It is straightforward to show that the total spin and chirality commute. We will show later that states with opposite chirality are split by an energy gap which is determined by the magnitude of the Dzyaloshinskii-Moriya interaction. Furthermore, we can separate states with opposite total spin by applying a magnetic field. This allows us to choose which doublet makes up the ground state, chirality or total spin. In this way it is possible to either encode the qubit in the total spin of the molecule or in the chirality. Furthermore, even thought the commutation relations of the chirality components are the same as those of the spin components, the transformation properties of spin and chirality under rotations, reflections, and time-reversal do differ. Therefore, interactions of chirality with external fields can not be inferred from the analogy with spins. We will discuss later how using the chirality offers certain benefits with regards to the possibility to control the qubit and with regards to increasing the decoherence time of the qubit.

11.3 Single-Qubit Rotations and the Spin-Electric Effect

If one chooses to encode a qubit in a spin state -be it the spin of an electron in a quantum dot, or the total spin of a molecular magnet- the most intuitive way to implement a one-qubit gate is by utilizing the Zeeman coupling $\mu_B \mathbf{B} \cdot \bar{\bar{g}} \cdot \mathbf{S}$, where $\bar{\bar{g}}$ is the g-tensor. This coupling in principle allows one to perform rotations around an arbitrary axis by applying ESR (electron spin resonance) pulses. Indeed, it has been shown to be possible to implement single spin rotations on a sub-microsecond time scale using ESR techniques in quantum dots [55]. Furthermore, Rabi-oscillations of the magnetic cluster V_{15} have been shown to be possible, also on a sub-microsecond time scale [56]. At the moment, however, it appears experimentally very challenging to increase the temporal- and spatial resolution with which one can control magnetic fields to the point that is required for quantum computation in molecular magnets (i.e. nanosecond time scale and nanometer length scale).

For this reason, a large effort has been made to find alternative ways to control the spin state of molecular magnets. One natural candidate to replace magnetic manipulation is electric control. Strong, local electric fields can be created near a STM

tip, and these fields can be rapidly turned on and off by applying an electric voltage to electrodes that are placed close to the molecules that are to be controlled.

Electric manipulation requires a mechanism that gives a sizable spin-electric coupling. In quantum dots, the mechanism behind this coupling is the relativistic spin-orbit interaction (SOI), and experiments that show that it is possible to perform single spin rotations by means of electric dipole spin resonance (EDSR) have been proposed [57] and performed [58]. Unfortunately, the fact that this effect scale with the system size L as L^3 makes them unsuitable for molecular magnets, which are much smaller.

Instead, in Ref. [32], Trif et al. proposed a mechanism that leads to spin-electric coupling in triangular magnetic molecules with spin-orbit interaction and broken inversion symmetry. The mechanism relies on the fact that in such systems an electric field can alter the exchange interaction between a pair of spins within a molecule due to the field's coupling to the dipole moment of the connecting bond.

The lowest order coupling between electric field and the spin state of the triangular molecule is given by the electric-dipole coupling, through the Hamiltonian $H_{\text{e-d}} = -e\sum_i \mathbf{E}\cdot\mathbf{r}_i \equiv -e\mathbf{E}\cdot\mathbf{R}$. Here, e is the electron charge and $\mathbf{r}_i$ is the position of the i-th electron. The total dipole moment of the molecule is given by $-e\sum_i \mathbf{r}_i = -e\mathbf{R}$. Because of the D_{3h} symmetry of the molecule, the diagonal elements of total dipole moment operator must vanish in the proper symmetry-adapted basis. However, the electric-dipole coupling can mix states with different chirality. The nonzero matrix elements are the ones that are invariant under the symmetry-transformations of the triangular magnet. Since the $|m_S, \pm 1\rangle$ states and the operators $\pm X + iY$ both transform as the irreducible representation E' of the group D_{3h}, it follows that the only nonzero components in the low-energy subspace of the triangular molecules are

$$\langle m_S, \pm 1|-eX|m'_S, \mp 1\rangle = i\langle m_S, \pm 1|-eY|m'_S, \mp 1\rangle \equiv d\delta_{m_S,m'_S}. \tag{11.4}$$

Coupling to the $S = 3/2$ subspace is suppressed by the finite gap between the two subspaces. By its very nature, this symmetry analysis cannot yield any information on the magnitude of the effective electric dipole parameter d. This information will have to be extracted using other methods, such as ab initio modeling, Hubbard modeling, or experiments, something we will come back to later. We do note that a finite amount of asymmetry of the wave functions centered around each vertex of the triangle is required for the matrix elements in (11.4) to be nonzero. This asymmetry is caused by the small amount of delocalization of the electron states due to the exchange interaction with the states on the other vertices and creates the finite dipole moment of individual bonds. The dipole moment of the bonds, furthermore, must depend on the relative orientation of the two spins which are connected by that bond (i.e. whether they are parallel or anti-parallel) in order for the matrix elements in (11.4) to be nonzero.

Since the electric-dipole coupling connects states with different chirality, we can rewrite it in terms of the vector $\mathbf{C}_\parallel = (C_x, C_y, 0)$ as $H^{\text{eff}}_{\text{e-d}} = d\mathbf{E}'\cdot\mathbf{C}_\parallel$. The vector $\mathbf{E}'$ is given by $\mathbf{E}' = \mathcal{R}(7\pi/6 - 2\theta)\mathbf{E}$, where $\mathcal{R}(\phi)$ describes a rotation by an angle ϕ

around the z axis, and θ is the angle between $\mathbf{r}_1 - \mathbf{r}_2$ and $\mathbf{E}_\parallel = (E_x, E_y, 0)$. With the definition of the chirality operator as given in (11.4), we can rephrase the effective electric-dipole Hamiltonian in terms of exchange coupling between the individual spins

$$H_{\text{e-d}}^{\text{eff}} = \frac{4dE}{3} \sum_{i=1}^{3} \sin\left[\frac{2\pi}{3}(1-i) + \theta\right] \mathbf{S}_i \cdot \mathbf{S}_{i+1}, \tag{11.5}$$

where E is the magnitude of the in plane components of the electric field. Since the change in the exchange interaction $J_{i,i+1}$ is proportional to $|\mathbf{E}_\parallel \times (\mathbf{r}_{i+1} - \mathbf{r}_i)|$, only the component of the electric field that is perpendicular to the bond $\mathbf{r}_{i+1} - \mathbf{r}_i$ affects the exchange interaction $J_{i,i+1}$. This is consistent with the picture that the finite dipole moment of the bond between two vertices is caused by the deformation of the wave function due to exchange interaction. Otherwise, the strength of the coupling is completely determined by the parameter d. The fact that the change in $J_{i,i+1}$ is not uniform is crucial here, since therefore $[H_0, H_{\text{e-d}}^{\text{eff}}] \neq 0$ even in the absence of DM interaction, which allows the electric-dipole interaction to induce transitions between states with different chirality.

We have seen then that the electric-dipole coupling allows one to perform rotations of the chirality state about the x- and y axis, but not around the z axis (assuming a diagonal g-tensor). This is sufficient to perform arbitrary rotations in chirality space. However, so far the total spin does not couple to the electric field. This situation is remedied when we include spin-orbit interaction.

As with the electric-dipole coupling, one can deduct the form of the spin-orbit interaction from general symmetry considerations. Given the D_{3h} symmetry of the molecule, the most general form of the spin-orbit interaction is

$$H_{\text{SO}} = \lambda_{\text{SO}}^{\parallel} T_{A_2} S_z + \lambda_{\text{SO}}^{\parallel} (T_{E''_+} S_- + T_{E''_-} S_+). \tag{11.6}$$

Here, T_Γ denotes a tensor which acts on the orbital space and transforms according to the irreducible representation Γ. The nonzero elements in the low-energy subspace are then given by $\langle m_S, \pm 1 | H_{\text{SO}} | m'_S, \pm 1 \rangle = m_S \lambda_{\text{SO}}^{\perp} \delta_{m_S, m'_S}$, which leads to the spin-orbit Hamiltonian $H_{\text{SO}} = \Delta_{\text{SO}} C_z S_z$, where $\Delta_{\text{SO}} = \lambda_{\text{SO}}^{\parallel}$. Alternatively, one can use the fact that the spin-orbit interaction can be described by the Dzyaloshinskii-Moriya term in (11.1). Because of the symmetry of the molecule, the only nonzero component of the DM vector $\mathbf{D}_{i,i+1}$ is the out-of-plane component, so that it takes the form $\mathbf{D}_{i,i+1} = (0, 0, D_z)$. This gives the same form for H_{SO} as the previous considerations, provided one identifies $\lambda_{\text{SO}}^{\parallel} = D_z$.

Combining the results from this section, it follows that the Hamiltonian describing a triangular magnet in the presence of a magnetic- and electric field can be written in terms of the chirality and total spin of the molecule as

$$H = \Delta_{\text{SO}} C_z S_z + \mu_B \mathbf{B} \cdot \bar{\bar{g}} \cdot \mathbf{S} + d\mathbf{E} \cdot \mathbf{C}_\parallel. \tag{11.7}$$

Hence, for a magnetic field in the z direction, the eigenstates are $|\pm 1/2, \pm 1\rangle$, and an electric field causes rotations of the chirality state, but does not couple states

with opposite total spin. When $\mathbf{B}$ is not parallel to $\hat{\mathbf{z}}$, S_z is no longer a good quantum number, and hence an applied electric field can cause rotations in the total spin subspace through the electric-dipole and spin-orbit coupling. In this way it becomes possible to perform arbitrary rotations of the total spin state.

In Ref. [53], the authors were able to identify the parameters of the effective spin Hamiltonian with the parameters of the underlying Hubbard model. On the one hand, this has opened up the possibility to determine the parameters of the effective spin Hamiltonian by means of ab initio calculations [59, 60]. On the other hand, the description of the spin-electric effect in the language of the Hubbard model is useful because it gives an intuitive interpretation of the phenomena that we discussed so far. The Hubbard model description of a molecular magnet including spin-orbit interaction is given by

$$H_{\mathrm{H}} = \sum_{i,j} \sum_{\alpha,\beta} \left[c_{i\alpha}^{\dagger} \left(t\delta_{\alpha\beta} + \frac{i\mathbf{P}_{ij}}{2} \cdot \sigma_{\alpha\beta} \right) c_{j\beta} + \mathrm{H.c.} \right] + \sum_{j} U_j(n_{j\uparrow}, n_{j\downarrow}). \quad (11.8)$$

Here, $c_{i\alpha}^{\dagger}$ creates an electron with spin α whose wave function $|\phi_{i\sigma}\rangle$ is given by a Wannier function located around atom i. Furthermore, t describes spin-independent hopping. The vector $\mathbf{P}_{ij}$ describes spin-dependent hopping due to spin-orbit interaction and hence is proportional to the matrix element $\nabla V \times \mathbf{p}$ between Wannier states centered around atom i and j. The vector σ contains the Pauli matrices. Lastly, U describes the on-site repulsion. Typically, one considers a single-orbital model, and assumes that U is the largest energy scale. A perturbative expansion of (11.8) in $(|t|, |\mathbf{P}_{ij}|)/U$ allows one then to map the Hubbard model on a Heisenberg Hamiltonian with DM interaction [61, 62].

Equation (11.8) describes two scenarios. First, if the index i runs over the three magnetic atoms of the triangle only, it describes coupling between the magnetic atoms through direct exchange. Alternatively, (11.8) can describe the situation in which the coupling between two magnetic atoms is mediated by a non-magnetic bridge by adding a doubly-occupied non-magnetic atom on every line connecting two vertices. The former choice allows for a simpler description, whereas the latter choice is anticipated to be the more realistic one for molecular magnets. We will shortly discuss how either can be used to obtain more insight into the spin-electric effect.

The first thing one can show is that in the case of direct-exchange interaction the basis functions of the Hubbard model to first order in t and $\lambda_{\mathrm{SO}} \equiv \mathbf{P}_{ij} \cdot \mathbf{e}_z$ (due to symmetry $\mathbf{P}_{ij} = \lambda_{\mathrm{SO}}\mathbf{e}_z$) are

$$\left|\Phi_{A_2'}^{1\sigma}\right\rangle = \left|\psi_{A_2'}^{1\sigma}\right\rangle \quad (11.9)$$

$$\left|\Phi_{E_{\pm}'}^{1\sigma}\right\rangle = \left|\psi_{E_{\pm}'}^{1\sigma}\right\rangle + \frac{(e^{-2\pi i/3} - 1)(t \pm \sigma\lambda_{\mathrm{SO}})}{\sqrt{2}U} \left|\psi_{E_{\pm}'^{1}}^{2\sigma}\right\rangle + \frac{3e^{2\pi i/3}(t \pm \sigma\lambda_{\mathrm{SO}})}{\sqrt{2}U} \left|\psi_{E_{\pm}'^{2}}^{2\sigma}\right\rangle, \quad (11.10)$$

where $|\psi_{\Gamma}^{n\sigma}\rangle$ denotes the symmetry-adapted eigenstate of the Hubbard model with three electrons, total spin σ, and either single- ($n=1$) or double ($n=2$) occupancy that transforms according to the irreducible representation Γ. Specifically, the spin part of $|\psi_{E'_{\pm}}^{1\sigma}\rangle$ is given by the states $|\sigma,\pm 1\rangle$ in (11.2). It follows that in the limit of $t,\lambda_{\mathrm{SO}} \ll U$ (the limit in which the spin model gives an accurate description) the eigenstates of the Hubbard model are indeed the chirality states. At finite t,λ_{SO}, the eigenstates contain small contributions from doubly-occupied states.

Within the direct-exchange model, the electric field couples to the state of the molecule via two different mechanisms. The first term that has to be added to the Hubbard Hamiltonian comes from the fact that the electric potential takes different values at the positions of the magnetic centers in a molecule, which affects the on-site energy of the electrons as

$$H^0_{\text{e-d}} = -e\sum_{\sigma}\frac{E_y a}{\sqrt{3}}c^{\dagger}_{1\sigma}c_{1\sigma} - \frac{a}{2}\left(\frac{E_y}{\sqrt{3}}+E_x\right)c^{\dagger}_{2\sigma}c_{2\sigma} + \frac{a}{2}\left(\frac{E_x}{\sqrt{3}}-E_y\right)c^{\dagger}_{3\sigma}c_{3\sigma}. \tag{11.11}$$

Here, a is the distance between two magnetic atoms. The second contribution is given by

$$H^1_{\text{e-d}} = \sum_{i,\sigma} t^{\mathbf{E}}_{ii+1}c^{\dagger}_{i\sigma}c_{i+1\sigma} + \text{H.c.}, \tag{11.12}$$

which describes the modification of the hopping strength due to the electric field. The electric field-dependent hopping is given by $t^{\mathbf{E}}_{ii+1} = -\langle\phi_{i\sigma}|e\mathbf{r}\cdot\mathbf{E}|\phi_{i+1\sigma}\rangle$, and is hence related to the matrix elements of the electric dipole moment which mix the different Wannier functions. As before, a symmetry analysis tells us that the only nonzero matrix elements within the total spin-1/2 subspace are those proportional to

$$\langle\phi^{\sigma}_{E'_+}|ex|\phi^{\sigma}_{E'_-}\rangle = -i\langle\phi^{\sigma}_{E'_+}|ey|\phi^{\sigma}_{E'_-}\rangle \equiv d_{EE}. \tag{11.13}$$

Here, $|\phi^{\sigma}_{\Gamma}\rangle$ describes the linear combination of Wannier states with total spin σ which transforms according to the irreducible representation Γ. One can then calculate the matrix elements of both the electric-dipole coupling as well as the spin-orbit Hamiltonian perturbatively in $(t, eaE, d_{EE}E)/U$. Furthermore, since the electrons are localized, the off-diagonal elements of the dipole moment, d_{EE}, satisfy $d_{EE} \ll ea$. To lowest order the results are

$$|\langle\Phi^{1\sigma}_{E'_-}|H^0_{\text{e-d}}|\Phi^{1\sigma}_{E'_+}\rangle| \propto \left|\frac{t^3}{U^3}eEa\right|, \tag{11.14}$$

$$|\langle\Phi^{1\sigma}_{E'_-}|H^1_{\text{e-d}}|\Phi^{1\sigma}_{E'_+}\rangle| \approx \left|\frac{4t}{U}Ed_{EE}\right|, \tag{11.15}$$

$$|\langle\Phi^{1\sigma}_{E'_-}|H_{\mathrm{SO}}|\Phi^{1\sigma}_{E'_+}\rangle| = \pm\frac{5\sqrt{3}\lambda_{\mathrm{SO}}t}{2U}\mathrm{sgn}(\sigma). \tag{11.16}$$

These first two matrix elements can be identified with the matrix elements in (11.7) that mix the states with different chirality, and hence determine the parameter d. The last matrix element determines D_z. Therefore, all parameters of the effective spin model in (11.7) can be determined from the underlying microscopic model. In Ref. [60], Nossa et al. utilized the presented analysis to determine the value of D_z and J in the molecular magnet Cu_3 using spin-density functional theory.

It is known that in molecular magnets the direct exchange mechanism is often suppressed due to the localized nature of the electrons that determine the magnetic properties (which are typically of a d-wave nature) combined with the fact that the magnetic atoms are typically separated by non-magnetic bridge atoms. In Cu_3, for instance, exchange interaction between two Cu atoms follows a superexchange path along a Cu-O-W-O-W-O-Cu bond, which makes the Cu atoms third nearest neighbors [54]. A more accurate description on a microscopic basis of the spin-electric effect in a triangular magnet is therefore given by a model which includes a doubly-occupied non-magnetic atom on every line connecting two vertices, so that the mechanism behind the exchange interaction is superexchange. This is further strengthened by the expectation that the orbitals of the magnetic atoms do not deform easily in an electric field, whereas the bridge orbitals are expected to change their shape more easily.

In Ref. [53], the authors analyzed the behavior of a single Cu-Cu bond, including the non-magnetic bridge atom that connects the two Cu atoms, under the application of an electric field. By performing a fourth-order Schrieffer-Wolf transformation [63] on the Hamiltonian (11.8) for such a bond (using $(|t|, |\mathbf{P}_{ij}|)/U$ as small parameter) one can map the Hubbard model on the spin model

$$H_{12} = J\mathbf{S}_1 \cdot \mathbf{S}_2 + \mathbf{D} \cdot (\mathbf{S}_1 \times \mathbf{S}_2) + \mathbf{S}_1 \cdot \boldsymbol{\Gamma} \cdot \mathbf{S}_2. \tag{11.17}$$

Here, $\boldsymbol{\Gamma}$ is a traceless- and symmetric matrix. Equation (11.17) describes the most general quadratic spin Hamiltonian possible. The parameters $J, \mathbf{D}, \boldsymbol{\Gamma}$ can be determined from the parameters of the Hubbard model. Assuming that the bond angle between the Cu atom and the bridge atom is finite, the largest possible symmetry of a single bond with bridge atom is C_{2v}. This determines which spin parameters can be nonzero. If the electric field breaks the C_{2v} symmetry, extra terms can be generated. However, from the C_{2v} symmetry it follows that the strongest spin-electric coupling will be in the plane spanned by the Cu atoms and the bridge atom, and perpendicular to the Cu-Cu bond. This is due to the fact that this is the only direction in which the bond can have a finite dipole moment in the absence of an electric field (due to the molecular field), which gives rise to linear electric-dipole coupling. Indeed, it is this coupling that causes the effective Hamiltonian in (11.5), with effective electric-dipole moment given by

$$d = \frac{4}{U^3}\left[\left(48t^3 - 20tp_z^2\right)\kappa_t + \left(-20t^2 p_z + 3p_z^3\right)\kappa_{pz}\right]. \tag{11.18}$$

Here, t is the hopping parameter, p_z is the z component of the spin-orbit hopping, and $\kappa_t = \delta t/E$ and $\kappa_{pz} = \delta p_z/E$ relate the changes in t and p_z to the electric field E.

Using ab initio methods, the authors in Ref. [59] calculated the effective electric-dipole moment d in Cu_3. They found the value $d = 3.38 \times 10^{-33}$ C m. This corresponds to $d \approx 10^{-4} ea$, where a is the length of the Cu-Cu bond, and leads to Rabi oscillation times $\tau \approx 1$ ns for electric field $E \approx 10^8$ Vm^{-1}.

So far, we have only discussed single-qubit rotations. However, for a complete set of quantum gates, we also need a two-qubit gate. In the next section, we will discuss different proposals that have been made on how to implement such a two-qubit gate.

11.4 Two-Qubit Gates

Suppose we chose to encode our qubit states in the spin degrees of freedom of a system. Two-qubit gates such as the CNOT- or the $\sqrt{\text{SWAP}}$-gate can then be implemented by turning on the Heisenberg exchange interaction between two spins for a certain time [64]. For spins in quantum dots, this is relatively simply done by applying appropriate voltage pulses to the gate that controls the tunneling between two quantum dots. In contrast, in molecular magnets the exchange interaction between two molecules is typically determined by the chemistry of the molecule, and one has to search for more sophisticated ways to implement two-qubit gates.

The first method to couple the state of two qubits that we will discuss is based on coupling of two triangular molecular magnets through a quantum mechanical electric field in a cavity or stripline [32]. Such electric fields offer long-range and switchable coherent interaction between two qubits. The electric field of a phonon with frequency ω in a cavity of volume V is given by $\mathbf{E}_0(b_\omega^\dagger + b_\omega)$, where $b_\omega^\dagger$ creates a photon with frequency ω and the amplitude of the field is $|\mathbf{E}_0| \propto \sqrt{\hbar\omega/V}$. The coupling of such a photon to the in plane component of the chirality $\mathbf{C}_\parallel$ of a triangular molecule is then given by $\delta H_\text{E} = d\mathbf{E}_0' \cdot \mathbf{C}_\parallel (b_\omega^\dagger + b_\omega)$. In the rotating wave approximation, the Hamiltonian that describes the low-energy subspace of N triangular molecular magnets which interact with the photon field is given by $H_\text{s-ph} = \sum_j H^{(j)} + \hbar\omega b_\omega^\dagger b_\omega$, with

$$H^{(j)} = \Delta_\text{SO} C_z^{(j)} S_z^{(j)} + \mathbf{B} \cdot \bar{\bar{g}} \cdot \mathbf{S}^{(j)} + d|\mathbf{E}_0|\left[e^{i\phi_j} b_\omega^\dagger C_-^{(j)} + \text{H.c.}\right]. \tag{11.19}$$

Here, $\phi_j = 7\pi/6 + \theta_j$. Application of a magnetic field $\mathbf{B}$ with an in plane component allows one to couple both the chirality as well as the total spin degrees of freedom of spatially separated molecules. This coupling can be turned on and off by bringing the molecules in resonance with the photon mode, by applying an additional local electric field. One difficulty in using cavities is that the electric fields are weaker than those at an STM tip. A typical value is $|\mathbf{E}_0| \approx 10^3$ V m^{-1}, which leads to Rabi times $\tau \approx 0.01$–100 μs.

For the discussion of another proposed implementation of an electrically controlled two-qubit gate (in this case the $\sqrt{\text{SWAP}}$-gate), we turn our attention to the polyoxometalate $[PMo_{12}O_{40}(VO)_2]^{q^-}$. This molecule consists of a central mixed-valence core based on the $[PMo_{12}O_{40}]$ Keggin unit, capped by two vanadyl groups

containing one localized spin each [31]. In such a molecule, one can encode a two-qubit state in the spins of the vanadyl groups. The spins of the two vanadyl groups are weakly exchange coupled via indirect exchange interaction mediated by the core. The crucial property of the core is that one can tune the number of electrons it contains, since the exchange interaction between the vanadyl spins depends on the number of electrons on the core. Namely, if the core contains an odd number of electrons, the spin of the unpaired electron on the core couples to those of the vanadyl groups, and the effective interaction between the two qubits is relatively strong. In contrast, for an even number of spins on the core, the spins on the core pair up to yield a ground state with total spin 0. In this case, the exchange interaction between the pair of vanadyl spins is strongly reduced as compared to the situation with an odd number of electrons on the core. Since the redox flexibility of such polyoxometalates is typically rather high, the number of electrons n_C on the core can be tuned by electric means, by bringing the molecule near the tip of an STM. The system is then described by the Hamiltonian

$$\begin{aligned} H = & -J(n_C)\mathbf{S}_L \cdot \mathbf{S}_R - J_C(\mathbf{S}_L + \mathbf{S}_R) \cdot \mathbf{S}_C \\ & + (\epsilon_0 - eV)n_C + Un_C(n_C - 1)/2. \end{aligned} \tag{11.20}$$

Here, $\mathbf{S}_{L/R}$ are the spin operators of the two vanadyl groups, and $\mathbf{S}_C$ is the spin of the core. $J(n_C)$ denotes the exchange interaction between the two vanadyl spins. Given the previous discussion, $J(0) \approx 0$. The orbital energy of the electron on the core is given by ϵ_0, and V is the electric potential at the core. Lastly, U is the charging energy of the molecule, which defines the largest energy scale in the problem. We consider the subspace of only $n_C = 0$ or $n_C = 1$ electrons on the core.

The two-qubit $\sqrt{\text{SWAP}}$ is now implemented as follows: One starts out with an electric potential such that the stable configuration has $n_C = 0$ electrons on the core. That way, the two qubits are decoupled. By applying a voltage pulse V_g to the STM tip, one can switch to the state with $n_C = 1$ electrons. The Hamiltonian that describes the spin-state of the molecule is then given by [31]

$$H_1 = -\big[J(1) - J_C\big]\mathbf{S}_L \cdot \mathbf{S}_R - \frac{J_C}{2}\mathbf{S}^2. \tag{11.21}$$

Here, $\mathbf{S} = \mathbf{S}_L + \mathbf{S}_R + \mathbf{S}_C$ is the total spin of the molecule. The time-evolution of the system is determined by (11.21) for the duration τ_g of the pulse, afterwards the two vanadyl spins will be decoupled again. The first part of this Hamiltonian contains the wanted exchange coupling, and one can implement different two-qubit gates depending on the pulse length τ_g. For the $\sqrt{\text{SWAP}}$-gate, this time is given by the condition

$$\big[J(1) - J_C\big]\frac{\tau_g}{\hbar} = \frac{\pi}{2} + 2\pi n, \tag{11.22}$$

where n is an integer. The second term in (11.21) depends on the spin-state of the core, and is unwanted. However, we can get rid of it by choosing the pulse-length

such that the unitary evolution associated with the second term is equal to the unit operator. This condition turns out to be satisfied for times

$$\tau_g = \frac{4\pi}{3}\frac{\hbar}{|J_C|}m, \tag{11.23}$$

where m is an integer. Together, these last two equations give a requirement on $J(1)$ and J_C, namely

$$\frac{J(1)}{|J_C|} = \mathrm{sgn}(J_C) + \frac{3}{8}\frac{1-4n}{m}. \tag{11.24}$$

So far, we have assumed that switching between states with $n_C = 0$ and $n_C = 1$ can be perfectly controlled and is instantaneous. In reality, however, this transition is governed by quantum processes, and is a probabilistic process governed by the tunneling rate Γ between STM tip and molecule. Therefore, τ_g is inherently a stochastic quantity. To analyze these quantum effects, the authors in Ref. [31] numerically calculated the averaged fidelity $\mathcal{F} = \overline{\sqrt{\rho_{\mathrm{real}}\rho_{\mathrm{ideal}}}}$ between the idealized $\sqrt{\mathrm{SWAP}}$-gate with instantaneous switching and the real $\sqrt{\mathrm{SWAP}}$-gate with the stochastic tunneling ($\rho_{\mathrm{real}}/\rho_{\mathrm{ideal}}$ denote the obvious density matrices at the end of the $\sqrt{\mathrm{SWAP}}$-gate operation here). They found that the fidelity can be as high as $\mathcal{F} = 0.99$.

11.5 Decoherence in Molecular Magnets

Up to this point, we have assumed that the evolution of the quantum state of any qubit is unitary, and hence the information content of the qubit is infinitely long-lived. This assumption is only valid for a perfectly isolated system. In reality, however, any qubit will be coupled to its environment. Fluctuations in the environment can then lead to decoherence: The process whereby information about a quantum state is lost due to interaction with an environment. Decoherence of a single qubit typically takes place on two different time scales. The longitudinal decoherence time, or T_1-time, describes the average time it takes the environment to induce random transitions from $|0\rangle$ to $|1\rangle$, and vice versa. The transverse decoherence time, the T_2-time, describes the time it takes a systems to lose its information about the coherence between the $|0\rangle$ and $|1\rangle$ state. In other words, the T_2-time is the time it takes for a system initially in the pure quantum state described by the density matrix $\hat{\rho}_0 = |\psi_0\rangle\langle\psi_0|$, where $|\psi_0\rangle = \alpha|0\rangle + \beta|1\rangle$, to transform into the classical state $\hat{\rho}(t) = |\alpha|^2|0\rangle\langle 0| + |\beta|^2|1\rangle\langle 1|$. In this sense, decoherence is the cause of the transition from the quantum- into the classical regime. The T_1-time sets on upper limit on the time a system can be used as a classical bit, whereas a system can only be used as a qubit for times $T \ll T_1, T_2$. The T_1- and T_2-time of a system are not unrelated, and can indeed become of comparable magnitude in certain systems. For molecular magnets at low temperatures, however, typically $T_2 \ll T_1$.

The first measurement of the T_2-time of a system consisting of molecular magnets was performed by Ardavan et al. in 2007 (Ref. [65]). The measurements were performed on Cr_7M heterometallic wheels (M denotes Ni or Mn), and the authors found T_2-times of 3.8 μs for perdeuterated diluted Cr_7Ni solutions. The typical way to measure relaxation times is to use standard spin-echo techniques [66]. The T_2-time can be obtained from the decay with τ of a 2-pulse Hahn-echo measurement, consisting of the sequence: $\pi/2 - \tau - \pi - \tau -$ echo. In a similar manner, the T_1-time can be determined using the sequence $\pi - T - \pi/2 - \tau - \pi - \tau -$ echo. Here, T is varied, and τ is constant and short. One of the difficulties in measuring the T_2-times in magnetic clusters is the fact that, in a crystal, the different molecules are coupled by dipole-dipole interactions. This limits the T_2-time. The natural approach to avoid this problem is to consider molecules in solution. However, here the problem is that many magnetic clusters with high spin display strong axial anisotropy, with relatively large zero-field splitting. In a solution, these clusters will orient in a random matter. This problem is circumvented by using Cr_7Ni-clusters, which have a $S = 1/2$ ground state (and hence no zero-field splitting), and small anisotropy of the g-factor.

It was found that the main mechanism limiting the T_2 -time of the Cr_7Ni-clusters was coupling to protons. To increase the decoherence time, the authors therefore considered the perdeutered analogue compound. Indeed, according to expectations (^{2}D has a gyromagnetic ratio which is about $1/6$ of that of ^{1}H), this increased the coherence time roughly by a factor of 6, leading to a T_2-time of 3.8 μs at 1.8 K.

Our remaining discussion of decoherence in molecular magnets follows that of Ref. [67]. In spin systems, the two most common sources of decoherence are fluctuations in the electric environment (which couple to the spin state via spin-orbit interaction) and fluctuations of the spin state of the N nuclear spins $\mathbf{I}_p$ in the host material of the qubit, which are coupled to the system spins $\mathbf{S}_i$ due to hyperfine interaction. We will mainly focus on the latter mechanism, since it typically limits the decoherence time [56, 65]. The hyperfine interaction between nuclear spins and system spins is due to dipole-dipole interaction as well as contact interaction

$$H_{\mathrm{HF}} = D_{\mathrm{HF}} \sum_i \sum_p \frac{\mathbf{S}_i \cdot \mathbf{I}_p - 3(\mathbf{S}_i \cdot \hat{\mathbf{r}}_{ip})(\mathbf{I}_p \cdot \hat{\mathbf{r}}_{ip})}{r_{ip}^3} + \sum_i a_i \mathbf{S}_i \cdot \mathbf{I}_{q(i)}. \qquad (11.25)$$

Here, $D_{\mathrm{HF}} = (\mu_0/4\pi) g_I \mu_I g_S \mu_S$, and $\mathbf{r}_{ip} = \mathbf{r}_i - \mathbf{r}_p$. The contact interaction strength a_i is due to the finite overlap of the wave functions of the system spin and nuclear spins located at the same magnetic center. For small clusters, the latter term only leads to oscillations of the coherence, and hence we can neglect it [67]. To see how the hyperfine interaction leads to decoherence, let us consider a system in which the state of the qubit and that of the bath are initially uncorrelated. Furthermore, let the initial state of the qubit be given by $|\psi(0)\rangle = \frac{1}{\sqrt{2}}(|0\rangle + |1\rangle)$, and let the bath be prepared in the (mixed or pure) state described by the density operator $\hat{\rho}_n(0) = \sum_{\mathcal{I}} p_{\mathcal{I}} |\mathcal{I}\rangle\langle\mathcal{I}|$. Here, $|\mathcal{I}\rangle = |m_1^{\mathcal{I}}, \ldots, m_N^{\mathcal{I}}\rangle$ with $m_i^{\mathcal{I}}$ the projection of the nuclear spin operator $\mathbf{I}_i$ along the magnetic field. Two examples of possible

states the bath may be prepared in are the spin-polarized (pure) state with polarization P, and the equal superposition (mixed) state. In the first case, $p_{\mathcal{I}} = \delta_{\mathcal{I},n}$, where $|n\rangle$ is the state such that $\sum_p I_p^z |n\rangle = \frac{P}{2}|n\rangle$. In the latter case, $p_{\mathcal{I}} = 1/2^N$. This is the initial state of the bath in the absence of an external magnetic field, ignoring interactions between the nuclear spins. Over time, interactions between the bath and the qubit will introduce correlations between the two subsystems, evolving the state $|\Psi_{\mathcal{I}}(0)\rangle = |\psi(0)\rangle \otimes |\mathcal{I}\rangle$ into the state $|\Psi_{\mathcal{I}}(t)\rangle = \frac{1}{\sqrt{2}}(|0, \mathcal{I}_0\rangle + |1, \mathcal{I}_1\rangle)$ (if we consider only loss of phase coherence). In general, the states $|\mathcal{I}_0\rangle$ and $|\mathcal{I}_1\rangle$ will not be the same. Therefore, the reduced density matrix of the qubit, given by $\hat{\rho}_S(t) = \mathrm{Tr}_n[\sum_{\mathcal{I}} p_{\mathcal{I}} |\Psi_{\mathcal{I}}(t)\rangle\langle\Psi_{\mathcal{I}}(t)|]$, may have a decreased degree of coherence (i.e. smaller off-diagonal elements), since the nuclear spins are correlated with the spins of magnetic centers that encode the qubit. The degree of coherence can be quantified by $r(t) = \sum_{\mathcal{I}} P_{\mathcal{I}} r_{\mathcal{I}}(t)$, where $r_{\mathcal{I}}(t) = \langle\mathcal{I}_1(t)|\mathcal{I}_0(t)\rangle$, and $\langle 0|\hat{\rho}_S(0)|1\rangle = r_{\mathcal{I}}/2$. It is known that the decoherence rate depends on the initial state of the nuclear spin bath. For example, it has been shown that techniques such as narrowing of the nuclear state can drastically increase the decoherence times in quantum dot systems [68].

Next, we want to show in what way (11.25) leads to decoherence in a spin-cluster qubit (such as is realized in the triangular magnet in Sect. 11.2) in more detail. We have shown before that in spin clusters the qubit state is typically not encoded in the $\mathbf{S}_i$'s themselves, but instead in quantities like the total spin $\mathbf{S}$ or the chirality $\mathbf{C}$. However, we can always denote the basis states of the qubit by $|0\rangle$ and $|1\rangle$. Quite generally then, by projecting the spin operators $\mathbf{S}_i$ on the space spanned by $|0\rangle, |1\rangle$, and performing a second order Schrieffer-Wolff transformation on the resulting Hamiltonian, one can transform (11.25) into the Hamiltonian $H = \sum_{k=0,1} |k\rangle\langle k| \otimes H_k$, with

$$H_k = \sum_{p=1}^{N} \omega_p^k I_p^{z'} + \sum_{p \neq q} \left(A_{pq}^k I_p^{z'} I_q^{z'} + B_{pq}^k I_p^+ I_q^- \right), \tag{11.26}$$

where $\hat{\mathbf{z}}' = \mathbf{B}/|B|$. In the derivation of (11.26), we ignored terms that do not conserve energy. $\omega_p^0 - \omega_p^1$ is linear in H_{HF}, and the quantities $A_{pq}^0 - A_{pq}^1$ and $B_{pq}^0 - B_{pq}^1$ are quadratic in H_{HF}. The fastest contribution to decoherence is due to inhomogeneous broadening due to the terms $\propto I_p^{z'}$ in (11.26). These terms describes the magnetic field due to the nuclear spins, which is called the Overhauser field. The Overhauser field depends on the specific realization of the nuclear spin state (for times $t \ll \tau_n$, where τ_n is the typical evolution time of the nuclear spin state, the magnetic field is static). Therefore, if the nuclear spins are in a mixture of states, the coherence of the state $|\psi(0)\rangle$ is washed out due interference of the states that undergo time-evolution under different effective magnetic fields. This can be seen from the decoherence factor $r(t)$, which for $t \ll \tau_n$ evolves as $r(t) \approx e^{i(E_0 - E_1)t} \sum_{\mathcal{I}} P_{\mathcal{I}} e^{i\delta_{\mathcal{I}} t}$, where

$$\delta_{\mathcal{I}} \approx g_S \mu_S \sum_i \mathbf{B}_{\mathrm{HF}}^{\mathcal{I}}(\mathbf{r}_i) \cdot \left[\langle 0|\mathbf{S}_i|0\rangle - \langle 1|\mathbf{S}_i|1\rangle \right]. \tag{11.27}$$

The sum is over the spins in the spin cluster. Furthermore, $\mathbf{B}_{\mathrm{HF}}^{\mathcal{I}}(\mathbf{r}_i) = D_{\mathrm{HF}} \sum_p m_p^{\mathcal{I}} [\hat{\mathbf{z}}' - 3(\hat{\mathbf{z}}' \cdot \hat{\mathbf{r}}_{ip})\hat{\mathbf{r}}_{ip}]/r_{ip}^3$ is the Overhauser field. It has been shown, that decoherence of a qubit encoded in the total spin $\mathbf{S} = \sum_{i=1}^3 \mathbf{S}_i$ of a triangular cluster due to the distribution of the Overhauser field for the equal superposition mixed state typically takes place on time scales of 100 ns. The second order terms in (11.26) give contributions to the decoherence times that are several orders of magnitude smaller.

We have seen that due to hyperfine interaction, both the qubit state as well as the nuclear spin state evolve in time. Furthermore, even in the absence of hyperfine interaction the nuclear spin state itself evolves in time, according to the Hamiltonian $H_n = \hat{\mathbf{B}} \cdot \sum_p \omega_p \mathbf{I}_p + D_n \sum_{p<q} [\mathbf{I}_p \cdot \mathbf{I}_q = 3(\mathbf{I}_p \cdot \hat{\mathbf{e}}_{pq})(\mathbf{I}_q \cdot \hat{\mathbf{e}}_{pq})]/r_{pq}^3$. This dynamics of the nuclear bath can lead to additional broadening of the Overhauser field, and has been shown to lead to decoherence on the μs-time scale for a qubit state encoded in the total spin.

An interesting possibility to increase the decoherence time of a qubit is a triangular spin cluster was put forward in Ref. [67]. The idea is to use the chirality of cluster as qubit, instead of the total spin. In that case, the states $|0\rangle$ and $|1\rangle$ of this section become $|0\rangle_{C_z} = |-1/2, 1\rangle$, $|0\rangle_{C_z} = |-1/2, -1\rangle$. The crucial property of these state that causes the increased decoherence time is that since

$$\langle 1|S_{z,i}|1\rangle = \langle 0|S_{z,i}|0\rangle = -1/6, \tag{11.28}$$

the Overhauser field from (11.27) does not couple to the qubit. Therefore, decoherence processes in (11.26) are second order only. This can lead to decoherence times approaching milliseconds.

11.6 Initialization and Read-out

Initialization of a qubit in its ground state is arguably the DiVincenzo criterion that is most routinely realized. Therefore, we will not spend a lot of time discussing it here. The way to prepare a qubit in its ground state is by cooling it down to temperatures that are much smaller than the gap between the ground state in which one wants to prepare the system and the first excited state. This gap, which could for instance be due to magnetic anisotropy, is typically of the order of a few Kelvin, and may be controlled by external means, such as placing the molecular magnet in a magnetic field. This limits the temperature at which experiments can be done to several mK to K.

The read-out of the spin state is a topic on itself, and we refer the reader to the literature for an overview of the different techniques that are used [69].

11.7 Grover's Algorithm Using Molecular Magnets

One special topic that we wish to discuss in this chapter is the implementation of Grover's algorithm using molecular magnets [27]. Grover's algorithm can be used to find an entry in an unsorted database with N entries. A typical situation in which this would be required is if we were given a phone number, and wanted to find the associated name in a phone book. Classically, we would have to start with the first entry, and work our way down the list. Finding the name in this manner requires on average $N/2$ queries. If we had encoded the information in the phone book in a quantum state, we would have been able to find the correct entry with high probability in $O(N^{1/2})$ queries using Grover's algorithm. A crucial requirement for this algorithm is the possibility to generate arbitrary superpositions of eigenstates (and in particular the superposition where all eigenstates have approximately the same weight).

In large-spin magnetic molecules, the eigenstates are labeled by the quantum number m_S, the z projection of the total spin $S \gg 1/2$. The Hamiltonian describing a single spin S with easy-axis along the z direction is given by

$$H = -AS_z^2 - BS_z^4 + V, \tag{11.29}$$

where $V = g\mu_B \mathbf{H} \cdot \mathbf{S}$. This gives rise to the typical double-well spectrum with non-equidistant level spacing. Such level spacing is crucial for the proposal in Ref. [27], as will become clear shortly. Suppose one starts out by preparing the system in the ground state $|\psi_0\rangle = |s\rangle$, and wishes to create an equal superposition of all the states $|m_0\rangle, |m_0+1\rangle, \ldots, |s-1\rangle$, where $m_0 = 1, 2, \ldots, s-1$. This corresponds to using $n-1$ states for Grover's algorithm, where $n = s - m_0$. In principle, one can create superpositions by applying a weak transverse magnetic field $\mathbf{H}_\perp$ (whose effect can be described using perturbation theory) which drives multiphoton transitions via virtual states through its coupling to S^+, S^-. However, to create the equal superposition that is required for Grover's algorithm, the amplitudes of all k-photon processes (here $k = 1, 2, \ldots, s - m_0$) must be equal. Clearly, perturbation theory is not valid in this regime. Therefore, a more sophisticated scheme is required.

The scheme that is proposed in Ref. [27] to create an equal superposition uses a single coherent magnetic pulse of duration T with a discrete frequency spectrum $\{\omega_m\}$. It contains n high-frequency components and a single low-frequency component ω_0, chosen such that $\hbar\omega_0 \ll \epsilon_{m_0} - \epsilon_{m_0+1}$. Here, ϵ_m is the energy of the eigenstate $|m\rangle$. The frequencies of the n high-frequency components are given by $\hbar\omega_{s-1} = \epsilon_{s-1} - \epsilon_s - \hbar(n-1)\omega_0$ and $\omega_m = \epsilon_m - \epsilon_{m+1} + \hbar\omega_0$ for $m = m_0, \ldots, s-2$. For the molecular magnet Mn_{12}, the high-frequency components have frequencies between 20-120 GHz, and ω_0 is around 100 MHz. Because of the non-equidistant splitting of the energy levels, all frequencies are different. The low-frequency component is applied along the easy axis, the high frequency components are in plane, so that the coupling is given by

$$V_{\text{low}}(t) = g\mu_B H_0(t) \cos(\omega_0 t) S_z, \tag{11.30}$$

$$V_{\text{high}}(t) = \sum_{m=m_0}^{s-1} g\mu_B H_m(t)\big[\cos(\omega_m t + \Phi_m)S_x - \sin(\omega_m t + \Phi_m)S_y\big]$$

$$= \sum_{m=m_0}^{s-1} \frac{g\mu_B H_m(t)}{2}\big[e^{i(\omega_m t+\Phi_m)}S^+ + e^{-i(\omega_m t+\Phi_m)}S^-\big]. \qquad (11.31)$$

Hence, absorption (emission) of a high-frequency σ^--photon induces a transition with $\Delta m = -1$ (1); the low-frequency π-photons do not change m, instead they supply the energy required to fulfill the resonance condition for allowed transitions. The phases Φ_m can be chosen freely, we will come back to this point later. With this setup, the lowest order transition between the ground state $|s\rangle$ and all states $|m\rangle$ (for $m_0 \le m < s$) is n'th order in $V(t) = V_{\text{low}}(t) + V_{\text{high}}(t)$.

To see this, let us consider an explicit example where $s = 10$, $m_0 = 5$, and hence $n = 5$. The lowest order transition from $|s\rangle$ to $|s-1\rangle$ uses 4 π-photons of energy $\hbar\omega_0$ and 1 σ^--photon with energy $\hbar\omega_{s-1}$. The transition from $|s\rangle$ to $|s-2\rangle$ uses 3 π-photons of energy $\hbar\omega_0$, 1 σ^--photon with energy $\hbar\omega_{s-1}$, and 1 σ^--photon with energy $\hbar\omega_{s-2}$; and so on for the other transitions. ω_0 can be chosen such that lower order transitions are forbidden due to the requirement of energy conservation. The amplitude of higher order transitions is small in the perturbative regime.

Since all transition amplitudes are the same order in $V(t)$, they are all approximately equal. To make them exactly equal requires some fine-tuning. For rectangular pulses with $H_k(t) = H_k$ for $T/2 < t < T/2$, the n'th order contribution to the S-matrix for the transition between $|s\rangle$ and $|m\rangle$, denoted by $S^{(n)}_{m,s}$, is given by

$$S^{(n)}_{m,s} = \sum_F \Omega_m \frac{2\pi}{i}\left(\frac{g\mu_B}{2\hbar}\right)^n \frac{\Pi_{k=m}^{s-1} H_k e^{i\Phi_k} H_0^{m-m_0} p_{m,s}(F)}{(-1)^{q_F} q_F! r_s(F)! \omega_0^{n-1}}$$

$$\times \delta^{(T)}\left(\omega_{m,s} - \sum_{k=m}^{s-1}\omega_k - (m-m_0)\omega_0\right). \qquad (11.32)$$

The sum runs over all Feynman diagrams F. $\Omega_m = (m-m_0)!$, $q_F = m - m - r_s(F)$, $p_{m,s}(F) = \Pi_{k=m}^{s}\langle k|S_z|k\rangle^{r_k(F)}\Pi_{k=m}^{s-1}\langle k|S^-|k+1\rangle$, with $r_k(F) = 0, 1, 2, \ldots \le m - m_0$ the number of π-transitions in the transition belonging to the Feynman diagram F. $\delta^{(T)}(\omega) = 1/(2\pi)\int_{-T/2}^{T/2} \mathrm{d}t e^{i\omega T}$ is the delta-function of width T. It ensures energy conservation. For the example above, the requirement $|S^{(n)}_{m,s}| \approx |S^{(n)}_{-1,s}|$ for all $m \ge m_0$ (which corresponds to the equal superposition) is satisfied for parameters

$$H_8/H_0 = 0.04, \qquad H_7/H_0 = -0.25, \qquad H_6/H_0 = -0.61, \qquad H_5/H_0 = -1.12. \qquad (11.33)$$

H_9 can be chosen independently. For numerical estimates, we refer to the original paper, Ref. [27]. This concludes the discussion of generating the equal superposition required for Grover's algorithm.

With some adaptions, a single step in Grover's algorithm can be used to read-in and decode quantum information. This opens up the possibility to use molecular

magnets as dense and efficient memory devices. The phases Φ_m in (11.30)–(11.31) play a crucial role here. We denote $\Phi_m = \sum_{k=s-1}^{m+1} \Phi_k + \phi_m$. As we have seen before, we can irradiate the system with a coherent magnetic pulse of duration T such that all $S^{(n)}_{m,s} = \pm\eta$. In other words, the state after the pulse is $|\psi\rangle = \sum_{m=m_0}^{s} a_m |m\rangle$, where the amplitudes $a_1 = 1$ and $a_m = \pm\eta$. By identifying the amplitude $\pm\eta$ with the logical-1, respectively logical-0, we see that this state encodes a n-bit state. Because of the Φ_m dependence of the S-matrix (see (11.32)), we can switch between the $\pm\eta$ amplitude by choosing $\phi_m = 0, \pi$. This allows us to encode a general state between 0 and $2^n - 1$ in the quantum state of the molecular magnet. The set $\{\phi_m\}$ that one uses depends on the number that has to be encoded. For instance, encoding $12_{10} = 1101_2$ requires $\phi_9 = \phi_8 = \phi_7 = 0$ and $\phi_6 = \phi_5 = \pi$. Here, the states with $m = 9, 8, 7, 6, 5$ represent respectively the binary digits $2^0, 2^1, 2^2, 2^3, 2^4$.

To decode the state of the molecule, one applies a pulse for which $S^{(n)}_{m_0,s} = S^{(n)}_{m_0+1,s} = \cdots = S^{(n)}_{s-1,s} = -\eta$. This pulse amplifies the bits which have amplitude $-\eta$, and suppresses those with amplitude η. The accumulated error in this procedure is approximately $n\eta^2$. Read-out of this decoded state can be done by measuring the occupation of the different levels by standard spectroscopy, for instance using pulsed ESR. Irradiation with a pulse which contains the frequency $\hbar\omega_{m-1,m} = \epsilon_{m-1} - \epsilon_m$ drives transitions that are given by $S^{(1)}_{m-1,m}$. If the state $|m\rangle$ is occupied (meaning that its amplitude was $-\eta$), we would observe stimulated absorption when irradiating with frequency $\omega_{6,7}$ and stimulated emission when irradiating with frequency $\omega_{7,8}$. Since the energy levels are non-equidistant, this uniquely identifies the level.

Acknowledgements The authors would like to acknowledge financial support from the Swiss NSF, the NCCR Nanoscience Basel, and the FP7-ICT project "ELFOS".

References

1. C.M. Papadimitriou, *Computational Complexity* (Addison-Wesley, Reading, 1994)
2. D.P. DiVincenzo, Fortschr. Phys. **48**, 771 (2000)
3. D. Deutsch, R. Jozsa, Proc. R. Soc. Lond. Ser. A, Math. Phys. Sci. **439**, 553 (1992)
4. R. Cleve, A. Ekert, C. Macchiavello, M. Mosca, Proc. R. Soc. Lond. Ser. A, Math. Phys. Sci. **454**, 339 (1998)
5. L.K. Grover, in *Proceedings of the 28th Annual ACM Symposium on the Theory of Computing*, (1996), p. 212
6. P. Shor, SIAM J. Comput. **26**, 1484 (1997)
7. D. Deutsch, Proc. R. Soc. Lond. A **400**, 97–117 (1985)
8. J. Church, Am. J. Math. **58**, 435 (1936)
9. A.M. Turing, Proc. Lond. Math. Soc. **442**, 230 (1936)
10. M.A. Nielsen, I.L. Chuang, *Quantum Computation and Quantum Information* (Cambridge University Press, New York, 2000)
11. W.K. Wootters, W.H. Zurek, Nature **299**, 802 (1982)
12. A. Barenco, C.H. Bennett, R. Cleve, D.P. DiVincenzo, N. Margolus, P. Shor, T. Sleator, J.A. Smolin, H. Weinfurter, Phys. Rev. A **52**, 3457 (1995)
13. D. Loss, D.P. DiVincenzo, Phys. Rev. A **57**, 120 (1998)
14. A. Imamoglu, D.D. Awschalom, G. Burkard, D.P. DiVincenzo, D. Loss, M. Sherwin, A. Small, Phys. Rev. Lett. **83**, 4204 (1999)

15. J.I. Cirac, P. Zoller, Phys. Rev. Lett. **74**, 4091 (1995)
16. Q.A. Turchette, C.J. Hood, W. Lange, H. Mabuchi, H.J. Kimble, Phys. Rev. Lett. **75**, 4710 (1995)
17. N.A. Gershenfeld, I.L. Chuang, Science **275**, 350 (1997)
18. A. Shnirman, G. Schön, Z. Hermon, Phys. Rev. Lett. **79**, 2371 (1997)
19. B.E. Kane, Nature (London) **393**, 133 (1998)
20. R. Vrijen, E. Yablonovitch, K.L. Wang, H.W. Jiang, A.A. Balandin, V. Roychowdhury, T. Mor, D.P. DiVincenzo, Phys. Rev. A **62**, 012306 (2000)
21. E. Knill, R. Laflamme, G.J. Milburn, Nature (London) **409**, 46 (2001)
22. F. Jelezko, J. Wrachtrup, Phys. Status Solidi A **203**, 3207 (2006)
23. R. Hanson, D.D. Awschalom, Nature (London) **453**, 1043 (2008)
24. P. Maletinsky, S. Hong, M.S. Grinolds, B. Hausmann, M.D. Lukin, R.L. Walsworth, M. Loncar, A. Yacoby, Nat. Nanotechnol. (2012). doi:10.1038/nnano.2012.50
25. D.V. Bulaev, B. Trauzettel, D. Loss, Phys. Rev. B **77**, 235301 (2008)
26. M. Trif, V.N. Golovach, D. Loss, Phys. Rev. B **77**, 045434 (2008)
27. M.N. Leuenberger, D. Loss, Nature (London) **410**, 789 (2001)
28. J. Tejada, E. Chudnovsky, E. del Barco, J. Hernandez, T. Spiller, Nanotechnology **12**, 181 (2001)
29. F. Meier, J. Levy, D. Loss, Phys. Rev. Lett. **90**, 047901 (2003)
30. F. Troiani, A. Ghirri, M. Affronte, S. Carretta, P. Santini, G. Amoretti, S. Piligkos, G. Timco, R.E.P. Winpenny, Phys. Rev. Lett. **94**, 207208 (2005)
31. J. Lehmann, A. Gaita-Arino, E. Coronado, D. Loss, Nat. Nanotechnol. **2**, 312 (2007)
32. M. Trif, F. Troiani, D. Stepanenko, D. Loss, Phys. Rev. Lett. **101**, 217201 (2008)
33. E.M. Chudnovsky, L. Gunther, Phys. Rev. Lett. **60**, 661 (1988)
34. D.D. Awschalom, J.F. Smyth, G. Grinstein, D.P. DiVincenzo, D. Loss, Phys. Rev. Lett. **68**, 3092 (1992)
35. R. Sessoli, D. Gatteschi, A. Caneschi, M.A. Novak, Nature (London) **365**, 141 (1993)
36. L. Thomas, F. Lionti, R. Ballou, D. Gatteschi, R. Sessoli, B. Barbara, Nature (London) **383**, 145 (1996)
37. J.R. Friedman, M.P. Sarachik, J. Tejada, R. Ziolo, Phys. Rev. Lett. **76**, 3830 (1996)
38. W. Wernsdorfer, E. Bonet Orozco, K. Hasselbach, A. Benoit, D. Mailly, O. Kubo, H. Nakano, B. Barbara, Phys. Rev. Lett. **79**, 4014 (1997)
39. J. Tejada, X.X. Zhang, E. del Barco, J.M. Hernández, E.M. Chudnovsky, Phys. Rev. Lett. **79**, 1754 (1997)
40. E. del Barco, A.D. Kent, E.M. Rumberger, D.N. Hendrickson, G. Christou, Phys. Rev. Lett. **91**, 047203 (2003)
41. A. Chiolero, D. Loss, Phys. Rev. Lett. **80**, 169 (1998)
42. F. Meier, D. Loss, Phys. Rev. Lett. **86**, 5373 (2001)
43. D. Gatteschi, A. Caneschi, L. Pardi, R. Sessoli, Science **265**, 1054 (1994)
44. C. Sangregorio, T. Ohm, C. Paulsen, R. Sessoli, D. Gatteschi, Phys. Rev. Lett. **78**, 4645 (1997)
45. D. Gatteschi, R. Sessoli, A. Cornia, Chem. Commun. **725** (2000). doi:10.1039/A908254I
46. D. Loss, D.P. DiVincenzo, G. Grinstein, Phys. Rev. Lett. **69**, 3232 (1992)
47. M.N. Leuenberger, D. Loss, Phys. Rev. B **61**, 1286 (2000)
48. M.N. Leuenberger, F. Meier, D. Loss, Monatsh. Chem. **134**, 217 (2003)
49. W. Wernsdorfer, R. Sessoli, Science **284**, 133 (1999)
50. M.N. Leuenberger, D. Loss, Phys. Rev. B **63**, 054414 (2001)
51. G. González, M.N. Leuenberger, Phys. Rev. Lett. **98**, 256804 (2007)
52. G. González, M.N. Leuenberger, E.R. Mucciolo, Phys. Rev. B **78**, 054445 (2008)
53. M. Trif, F. Troiani, D. Stepanenko, D. Loss, Phys. Rev. B **82**, 045429 (2010)
54. K.-Y. Choi, Y.H. Matsuda, H. Nojiri, U. Kortz, F. Hussain, A.C. Stowe, C. Ramsey, N.S. Dalal, Phys. Rev. Lett. **96**, 107202 (2006)
55. F.H.L. Koppens, C. Buizert, K.J. Tielrooij, I.T. Vink, K.C. Nowack, T. Meunier, L.P. Kouwenhoven, L.M.K. Vandersypen, Nature (London) **442**, 766 (2006)

56. S. Bertaina, S. Gambarelli, T. Mitra, B. Tsukerblat, A. Müller, B. Barbara, Nature (London) **453**, 203 (2008)
57. M. Borhani, V.N. Golovach, D. Loss, Phys. Rev. B **73**, 155311 (2006)
58. K.C. Nowack, F.H.L. Koppens, Yu.V. Nazarov, L.M.K. Vandersypen, Science **318**, 1430 (2007)
59. M.F. Islam, J.F. Nossa, C.M. Canali, M.R. Pederson, Phys. Rev. B **82**, 155446 (2010)
60. J.F. Nossa, M.F. Islam, C.M. Canali, M.R. Pederson, Phys. Rev. B **85**, 085427 (2012)
61. P.W. Anderson, Phys. Rev. **115**, 2 (1959)
62. T. Moriya, Phys. Rev. **120**, 91 (1960)
63. R. Winkler, *Spin-Orbit Copuling Effects in Two-dimensional Electron and Hole Systems* (Springer, Berlin, 2003)
64. G. Burkard, D. Loss, D.P. DiVicenzo, Phys. Rev. B **59**, 2070 (1999)
65. A. Ardavan, O. Rival, J.J.L. Morton, S.J. Blundell, A.M. Tyryshkin, G.A. Timco, R.E.P. Winpenny, Phys. Rev. Lett. **98**, 057201 (2007)
66. A. Schweiger, G. Jeschke, *Principles of Pulse Electron Paramagnetic Resonance* (Oxford University Press, New York, 2001)
67. F. Troiani, D. Stepanenko, D. Loss, Phys. Rev. B **86**, 161409 (2012)
68. W.A. Coish, D. Loss, Phys. Rev. B **70**, 195340 (2004)
69. D. Gatteschi, R. Sessoli, J. Villain, *Molecular Nanomagnets* (Oxford University Press, New York, 2006)

XIX Symposium on Condensed Matter Physics SFKM 2015

Book of Abstracts

7 – 11 September 2015
Belgrade, Serbia

Spin-electric Coupling in Molecular Magnets

Dimitrije Stepanenko

Center for Condensed Mater Physics and New Materials, Institute of Physics Belgrade

Abstract. Molecular magnets behave as large spins at low energies. They show hysteresis controlled by quantum tunneling of magnetization, long spin coherence times, and spin texture in the ground state. Coupling of molecular spins to an external electric fields would provide a superior mechanism for their control and manipulation. In triangular low-spin antiferromagnets with broken inversion symmetry it is the chirality of spin texture that couples to electric fields. We show that the chirality has long coherence time, and that it allows for a controllable superradiant phase transition.

Hyperfine-induced decoherence in a triangular spin cluster varies across independent two-level subsystems that encode a qubit. Electrically controllable eigenstates of spin chirality show decoherence times that approach milliseconds, two orders of magnitude longer than those estimated for the eigenstates of the total spin projection and of the partial spin sums. The robustness of chirality is due to its decoupling from components of both the total spin and individual spins in the cluster.

A crystal of triangular molecular antiferromagnets coupled to a resonant cavity shows superradiant phase transition. The critical coupling strength for transition depends on the external magnetic field, in sharp contrast to the standard case of two-level emitters, where the critical coupling was set by the structure of emitter alone. The source of modification is traced to the entanglement of spin and chirality in the low-energy states of the cluster.

REFERENCES

1. Trif, M., Troiani, F., Stepanenko, D., and Loss, D., *Phys. Rev. B* **82**, 045429 (2010).
2. Troiani, F., Stepanenko, D., and Loss, D., *Phys. Rev. B* **86**, 161409(R) (2012).
3. Stepanenko, D., Trif, M, Tsyplyatyev, O., and Loss, D, arXiv:1502.04075

DANI FIZIKE KONDENZOVANOG STANJA MATERIJE

10 – 12 septembar 2013
Srpska akademija nauka i umetnosti
www.cond-mat.ipb.ac.rs

Utorak, 10 Septembar

10:00 – 10:40	Ivan Božović, Brookhaven National Laboratory (USA) ***Novi rezultati u fizici visoko-temperaturnih superprovodnika***
10:40 – 10:50	diskusija
10:50 – 11:00	pauza
11:00 – 11:40	Zoran Radović, Fizički fakultet ***Biharmonijska zavisnost Josephsonove struje od faze u superprovodnim spojevima sa nehomogenim feromagnetom***
11:40 – 11:50	diskusija
11:50 – 12:00	pauza
12:00 – 12:40	Antun Balaž, Institut za fiziku ***Proučavanje dipolnih Bose-Einstein kondenzata u anizotropnim slabim potencijalima sa neuređenošću***
12:40 – 12:50	diskusija
13:00 – 15:00	pauza za ručak
15:00 – 15:40	Darko Tanasković, Institut za fiziku ***Kvantni kritični transport u blizini Mottovog metal-izolator prelaza***
15:40 – 15:50	diskusija
15:50 – 16:00	pauza
16:00 – 16:40	Mihajlo Vanević, Fizički fakultet ***Kvantno proklizavanje faze u mezoskopskim superprovodnim žicama***
16:40 – 16:50	diskusija

Sreda, 11 Septembar

10:00 – 10:40	Milica Milovanović, Institut za fiziku ***Geometrijski opis frakcionih Chernovih izolatora***
10:40 – 10:50	diskusija
10:50 – 11:00	pauza
11:00 – 11:40	Ivanka Milošević, Fizički fakultet ***Termalne osobine helikalnih ugljeničnih nanotuba***
11:40 – 11:50	diskusija
11:50 – 12:00	pauza

– nastavak, Sreda 11 Septembar –	
12:00 – 12:40	Zoran Popović, Institut Vinča ***Dinamički Jahn-Tellerov efekat u grafenu sa šupljinskim defektom***
12:40 – 12:50	diskusija
13:00 – 15:00	pauza za ručak
15:00 – 15:40	Željko Šljivančanin, Institut Vinča ***Modelovanje atomske strukture djelimično oksidisanog grafena***
15:40 – 15:50	diskusija
15:50 – 16:00	pauza
16:00 – 16:40	Nenad Vukmirović, Institut za fiziku ***Priroda nosilaca naelektrisanja u organskim kristalima***
16:40 – 16:50	diskusija
16:50 – 17:00	pauza
17:00 – 17:40	Zoran Mišković, University of Waterloo (Canada) ***Interakcija grafena sa naelektrisanim česticama***
17:40 – 17:50	diskusija

Četvrtak, 12 Septembar

10:00 – 10:40	Velimir Radmilović, Tehnološko-metalurški fakultet ***Šta znamo o klizanju bez trenja na atomskom nivou?***
10:40 – 10:50	diskusija
10:50 – 11:00	pauza
11:00 – 11:40	Nataša Bibić, Institut Vinča ***Modifikacija tankih slojeva metala i keramika primenom jonskih snopova***
11:40 – 11:50	diskusija
11:50 – 12:00	pauza
12:00 – 12:40	Đorđe Spasojević, Fizički fakultet ***Analiza spening lavina u dvodimenzionalnom neravnotežnom Izingovom modelu na temperaturi T=0***
12:40 – 12:50	diskusija
13:00 – 15:00	pauza za ručak
15:00 – 15:40	Dimitrije Stepanenko, Institut za fiziku ***Kvantni računari bazirani na kvantnim tačkama i spin-orbit interakciji***
15:40 – 15:50	diskusija
15:50 – 16:00	pauza
16:00 – 16:40	Nenad Švrakić, Institut za fiziku ***Pokrivanje i pakovanje u ravni: egzaktni i numerički rezultati za mešavine superdiskova***
16:40 – 16:50	diskusija

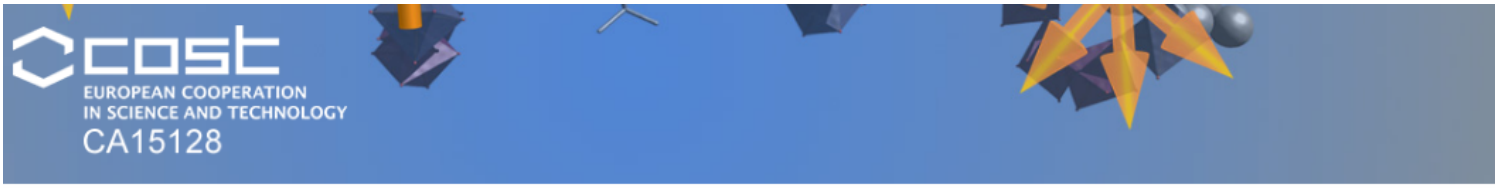

CORE GROUP

AC	Eugenio Coronado
VC	Roberta Sessoli
Training Schools and Workshops Coordinator	Mirko Cincheti
Short Training Scientific Missions Manager	Laura Pereira
Website and Dissemination Manager	Alejandro Gaita Ariño
WG1 Leader	Alek Dediu
WG2 Leader	Herre Van Der Zant
WG3 Leader	Fernando Luis
Website and Dissemination Assistant	Dawid Pinkowicz
WG1 Assistant	Luis Hueso
WG2 Assistant	Uta Schlickum
WG3 Assistant	Dimitrije Stepanenko

Republic of Serbia - Deutscher Akademischer Austauschdienst-DAAD

Листа одобрених пројеката за пројектни циклус 2014-2015. година

	Serbian applicant	***German applicant***	***Project title***
1.	Dr. Aleksandar MILOSAVLJEVIC Institute of Physics, Belgrade	Prof. Dr. Ilko BALD U Potsdam	The study of DNA radiation damage on the molecular level
2.	Dr. Magdalena STEVANOVIĆ Institute of Technical Sciences SANU	Prof. Dr. Aldo BOCCACCINI U Erlangen	Scaffolds with therapeutic functionality
3.	Dr. Dimitrije STEPANENKO Institute of Physics, Belgrade	Prof. Dr. Guido BURKARD U Konstanz	Spin-orbit interaction of confined electrons for quantum information processing
4.	Prof. Dr. Ivan LUKOVIC Faculty of Technical Sciences, U Novi Sad	Heiko KERN/ Dr. KÜHNE Institut für Angewandte Informatik Leipzig	Discovering Effective Methods and Architec-tures for Integration of Modeling Spaces
5.	Prof. Dr. Milorad KURAICA Institute of Physics, Belgrade	Prof. Dr. Jürgen MEICHSNER U Greifswald	Volume and Surface Processes in Barrier Discharges
6.	Prof. Dr. Jasmina MARKOVIĆ	Prof. Dr. Claudia	Characterization of Progenitor Cells for

	LIPKOVSKI School of Medecine, U Belgrade	MÜLLER U Tübingen	Kidney Regeneration (“ProKiReg”)
7.	Prof. Dr. Ljiljana SIMIC Institute of Physics, Belgrade	Prof. Dr. Ivan PERIĆ U Heidelberg	High-voltage pixel sensors for particle physics
8.	Prof. Dr. Goran RISTIC Faculty of Electronic Engineering, U Niš	Dr.-Ing. Zoran STAMENKOVIC IHP Frankfurt/Oder	Verification and Test of Fault-Tolerant Integrated Circuits
9.	Dr. Danijela MAKSIMOVIC-IVANIC Institute for Biological Research”Siniša Stanković”, Belgrade	Prof. Dr. Ludger WESSJOHANN Leibniz-Institut für Pflanzenbiochemie Halle	Interplay of novel and established natural products in cancer treatment
10.	Prof. Dr. Nenad T. PAVLOVIC Mechanical Engineering Faculty U Niš	Prof. Dr. Lena ZENTNER TU Ilmenau	Adaptive compliant mechanisms with inherent actuating elements

Evidencioni broj projekta	Naslov projekta	Srpski predlagač	Srpska institucija	Francuski predlagač	Francuska institucija	Finansiranje projekata u Srbiji za 2016 u evrima	Finansiranje projekata u Francuskoj za 2016 u evrima	Finansiranje projekata u Srbiji za 2017 u evrima	Finansiranje projekata u Francuskoj za 2017 u evrima
451-03-39/2016/09/01	Softer zasnovan na izvršnim modelima za pametne Sajber fizičke sisteme	Miroslav Trajanović	Mašinki fakultet, Univerzitet u Nišu	Alexis Aubry	CRAN UMR 7039, Universute de Lorraine, CNRS	2100,00	2100,00	2100,00	2100,00
451-03-39/2016/09/02	Razvoj „zelenih tehnologija“ za prečišćavanje otpadnih voda zasnovanih na nanoferitima	Biljana Dojčinović	Institut za hemiju, tehnologiju i matalurgiju, Beograd	Lotfi Bessais	Institut de Chimie et Matériaux Paris Est (ICMPE)	2100,00	2100,00	2100,00	2100,00
451-03-39/2016/09/03	Nanostrukturne transparantne keramike dobijene kombinovanjem slip kastinga i mikrotalasnog sinterovanja	Radenka Krsmanović Whiffen	Institut za nuklearne nauke Vinča, Beograd	Damien Bregiroux	Université Pierre et Marie Curie - LCMCP	2100,00	2100,00	2100,00	2100,00
451-03-39/2016/09/04	Funkcionalna ispitivanja ivermektina na parazitu konja Parascaris equorum	Saša Trailović	Fakultet veterinarske medicine, Univerzitet u Beogradu	Claude Charvet	Institut National de la Recherche Agronomique (INRA)	2100,00	2100,00	2100,00	2100,00
451-03-39/2016/09/05	Logika u računarstvu i viša algebra	Silvia Gilezan	Matematički institut SANU, Beograd	Pierre Louos Curien	Iniversity oaris Diderot, Paris	2100,00	2100,00	2100,00	2100,00
451-03-39/2016/09/06	Racionalni dizajn, sinteza i karakterizacija novih jednomolekulskih magnetnih	Maja Gruden Pavlović	Hemijski fakultet, Univerzitet u Beogradu	Carole Duboc	Universite Grenoble Alpe	2100,00	2100,00	2100,00	2100,00
451-03-39/2016/09/07	Evaluacija reakcije tkiva zgloba psa posle aplikacije autologih mezenhimalnih matičnih ćelija	Milica Kovačević	Fakultet veterinarske medicine, Univerzitet u Beogradu	Olivier Gauthier	Oniris Nantes Atlantic College of Veterinary Medicine,	2100,00	2100,00	2100,00	2100,00

Evidencioni broj projekta	Naslov projekta	Srpski predlagač	Srpska institucija	Francuski predlagač	Francuska institucija	Finansiranje projekata u Srbiji za 2016 u evrima	Finansiranje projekata u Franciskoj za 2016 u evrima	Finansiranje projekata u Srbiji za 2017 u evrima	Finansiranje projekata u Franciskoj za 2017 u evrima
451-03-39/2016/09/08	Unapredjenje industrijskih i tehnoloških procesa primenom bezbednih rastvarača	Slobodan Gadžurić	Prirodno-matematički fakultet, Univerzitet u Novom Sadu	Abdenacer Idrissi	University of Lille Sciences and technologies	2100,00	2100,00	2100,00	2100,00
451-03-39/2016/09/09	Razvoj kombinatorne optimizacije	Tatjana Davidovic	Matematički institut SANU, Beograd	Ivana Ljubić	ESSEC Busoness School of Paris	2100,00	2100,00	2100,00	2100,00
451-03-39/2016/09/10	Implementacija hrišćanstva u kasnoantičkoj dijecezi Mezija/Dakija Prospografija 2 faza /GIS1. faza	Vujadin Ivanišević	Arheološki instsitut , Univerzitet u Beogradu	Dominie Moreau	Universite de Lille	2100,00	2100,00	2100,00	2100,00
451-03-39/2016/09/11	Eksperimentalno odredjivanje mehanizama habanja na nano i na makro dimenzionom nivou premošćavanja razlika	Aleksandar Vencl	Mašinski fakultet, Univerzitet u Beogradu	Oliver Noel	Université du Maine – IMMM UMR CNRS 6283	2100,00	2100,00	2100,00	2100,00
451-03-39/2016/09/12	Nanostrukturni kompozitni materijali za skaldištenje vodonokau čvrstom stanju	Jasmina Grbović Novaković	Institut za nuklearne nauke Vinča, Beograd	Patricia de Rongo	CNRS, Neel Institute CRETA BP 166	2100,00	2100,00	2100,00	2100,00
451-03-39/2016/09/13	Inteligentni ekološki nanomaterijali i nanokompoziti	Vesna Rakić	Poljoprivredni fakultet, Univerzitet u Beogradu	Georgeta Pastelo	Institut de recherches sur la catalyse et 1	2100,00	2100,00	2100,00	2100,00
451-03-39/2016/09/14	Komplementarna, napredna dijagnostika jačine električnog polja u plazmenim mlazevima koji se koriste u biološke i	Milorad Kuraica	Fizički fakultet, Univerzitet u Beogradu	Eric Robert	GREMI, UMR7344, CNRS/	2100,00	2100,00	2100,00	2100,00

Evidencioni broj projekta	Naslov projekta	Srpski predlagač	Srpska institucija	Francuski predlagač	Francuska institucija	Finansiranje projekata u Srbiji za 2016 u evrima	Finansiranje projekata u Franciskoj za 2016 u evrima	Finansiranje projekata u Srbiji za 2017 u evrima	Finansiranje projekata u Franciskoj za 2017 u evrima
451-03-39/2016/09/15	Usavršavanje tačnosti spektroskopsko dijagnostičkih modela za astrofizičku i magnetno fuzionu plazmu	Zoran Simić	Astronomska opservatorija, Beograd	Joël Rosato	Laboratorija PIIM, UMR 7345 Aix-Marseille Université /CNRS	2100,00	2100,00	2100,00	2100,00
451-03-39/2016/09/16	Električna kontrola nspinova u molekularnim magnetima i nanokristalima (eLEcmOimAG)	Dimitrije Stapanenko	Institut za fiziku, Beograd	Simon Simon	Universite Paris Sud	2100,00	2100,00	2100,00	2100,00
451-03-39/2016/09/17	Luminiscentni „plivači“ za detekciju žive bazirani na primeni bipolarne elektrohemije	Dragan Manojlović	Hemijski fakultet, Univerzitet u Beogradu	Nešo Šojić	Institute of Molecular Science (ISM), Pessac FRANCE	2100,00	2100,00	2100,00	2100,00
451-03-39/2016/09/18	Paralelni korpusi i dvojezična leksikografija: opis i primena	Veran Stanojević	Fililoški fakultet, Univerzitet u Beogradu	Dejan Stošić	Univerzitet u Tuluzu	2100,00	2100,00	2100,00	2100,00
451-03-39/2016/09/19	Luminescentna termometrija za nanonivou	Miroslav Dramićanin	Institut za nuklearne nauke Vinča, Beograd	Bruno Viana	IRCPInstitut de Recherche de Chimie Paris	2100,00	2100,00	2100,00	2100,00

ФИЗИЧКИ ФАКУЛТЕТ
УНИВЕРЗИТЕТА У БЕОГРАДУ
www.ff.bg.ac.rs/
СТУДЕНТСКИ ТРГ 12
11001 Београд – Стари Град,
Република Србија

Тополошки кубити отпорни на декохеренцију

Мастер рад

Зорица Ристић
Број индекса: 2017/7007

Универзитет у Београду
Физички факултет

Руководилац рада: Димитрије Степаненко,
Институт за физику, Београд
dimitrije.stepanenko@ipb.ac.rs

From: Marco AFFRONTE <marco.affronte@unimore.it>
Date: Fri, 2 Dec 2016 19:36:35 +0100
Message-ID: <CAAznCCcDED=eg=WVY-69zPumgOUNLi-APuyYwjMn=m0aNKTbiw@mail.gmail.com>
Subject: request for review PhD Thesis
To: Dimitrije.Stepanenko@ipb.ac.rs

Dear Professor Stepanenko

I am the coordinator of the PhD Course in Physics and NanoSciences a=
t
Universit=C3=A0 di Modena e Reggio Emilia (
http://www.nano-phdschool.unimore.it/site/home.html). Our PhD students of
XXIX Course have now completed their thesis work and we are looking for
internationally recognized experts in different fields to review their
manuscripts. This review process consists in critically reading the
manuscript of the candidates and provide corrections and
suggestions to improve its quality. It is done remotely by reviewers who
are kindly asked to assess the whole thesis work of the candidate in a 1-2
pages report within 4 weeks form the delivery of the manuscript (early
December), in any case before January 8th, 2017.

Your name has been suggested in this context and I=E2=80=99d ask you if you=
 are
kindly available to review the thesis work of:

Mr Simone Ierin=C3=B2:

Thesis title: *Multiple spin ensembles in cavity in strong excitation
limits*

We believe that this review process is a fundamental step for the formation
of young researchers and we=E2=80=99ll be very grateful if you can accept d=
oing
this service. I=E2=80=99ll be happy if you can confirm/or not your acceptan=
ce
within the next few days.

Best regards.

Prof. Marco Affronte

Dipartimento di Scienze Fisiche, Informatiche e Matematiche, Universit=C3=
=A0 di
Modena e Reggio Emilia

via G. Campi 213/A, 41125 Modena, Italy

phone: ++39.059.205.8375 // lab: .5271; skype: marcoaffronte

fax: 0039.059.205.5651; 0039.059.205.5235.

Date: Thu, 17 Dec 2015 08:17:30 -0500
Message-Id: <9145035825034@ejpwww6.nature.com.nature.com>
To: dimitrije.stepanenko@ipb.ac.rs
Subject: NATURE: Decision on Nature manuscript XXXXXXXXX
From: k.ziemelis@nature.com
Reply-To: k.ziemelis@nature.com

Dear Colleague,

Thank you for your help with the manuscript entitled "XXXXXXXXXXXXXXXXXXX" by XXXXXXXXXX and colleagues. We have now received all of the referees' reports, which I have attached below for your information. In the light of these various comments, we have decided to offer publication of a suitably revised version of the manuscript. Please treat this information as strictly confidential.

Thank you again for your help and I hope that we can call upon your advice in the future.

Yours sincerely,

Karl Ziemelis
Physical Sciences Editor, Nature
Nature's author and policy information sites are at
www.nature.com/nature/submit/.

Date: Mon, 4 Jun 2018 07:44:28 -0400
Message-Id: <49152811266867@ejpwww1.nature.com.nature.com>
To: dimitrije.stepanenko@ipb.ac.rs
Subject: Decision made for XXXXXXXXXX
From: Maria.Maragkou@nature.com
Reply-To: Maria.Maragkou@nature.com
X-AV-Checked: ClamAV using ClamSMTP

Dear Dr. Stepanenko,

Thank you for reviewing the manuscript "XXXXXXXXXXXXXXXX" for Nature Materials. In the light of the various comments we received, we have decided to offer publication of a suitably revised version of the manuscript. Please treat this information as strictly confidential.

Thank you again for your help and I hope that we can call upon your advice in the future.

Best wishes,

--
Maria Maragkou
Senior Editor
Nature Materials

Date: Wed, 4 Jan 2017 10:41:45 -0500
Message-Id: <72148354450562@ejpwww16.nature.com.nature.com>
To: dimitrije.stepanenko@ipb.ac.rs
Subject: Final Decision made for XXXXXXXX
From: scientificreports@nature.com
Reply-To: scientificreports@nature.com

Dear Dr. Stepanenko:

Thank you for your help with manuscript XXXXXXXX, "XXXXXXXXXXXXXX", which you recently reviewed for Scientific Reports.

For your records, the decision for this manuscript, based partly on your input, was Accept. A full copy of the comments to authors is appended, below.

Your assistance and participation in the review process for Scientific Reports is greatly appreciated.

Best regards,

Manuscript Administration
Scientific Reports
4 Crinan Street
London N1 9XW
E-mail: scientificreports@nature.com

Date: Mon, 18 Jun 2018 18:00:47 -0400
Message-Id: <70152935924718@buildmts-www5.nature.com.nature.com>
To: Dimitrije.Stepanenko@ipb.ac.rs
Subject: Final Decision made for XXXXXXXXX
From: npjqi@nature.com
Reply-To: npjqi@nature.com
X-AV-Checked: ClamAV using ClamSMTP

Dear colleague,

Thank you very much for reviewing the paper entitled "XXXXXXXXXXXX" for npj Quantum Information. Having considered the collective advice that we have received, the editor has taken the Revise decision. Please treat this information as strictly confidential.

For your information, the full complement of reviewers' reports is appended below, which I hope will provide some insight into the views of the other referees.

We appreciate the time you have taken to review this manuscript and submit your report. I hope that we may call upon your advice in the future.

Best regards,

Manuscript Administration
npj Quantum Information
4 Crinan Street
London N1 9XW
E-mail: npjqi@nature.com

Date: Mon, 9 Jul 2018 18:40:03 -0400
Message-ID: <1067306010.1531176003841.JavaMail.tomcat@prism-jobs-4-245>
From: prl@aps.org
Reply-To: prl@aps.org
To: dimitrije.stepanenko@ipb.ac.rs
Subject: Review_request STEPANENKO XXXXXXXXX

Re: XXXXXXX
XXXXXXXXXXXXXXXXXXXXXXXXXXXXXXXX
XXXXXXXXXXXXXXXXXXXXXXXXXXXXXXXXX

Dear Dr. Stepanenko,

We would appreciate your review of this submission to Physical Review Letters.

Please let us know promptly if you will be able to send a report and, if so, by when.

Do the authors make a convincing case for their claims?

Please address the Physical Review Letters criteria of impact, innovation, and interest in your report.

Thank you for your help.

Yours sincerely,

Robert Garisto
Editor
Physical Review Letters
Email: prl@aps.org
https://journals.aps.org/prl/
twitter @RobertGaristo

"Every 80 seconds someone cites a PRL"

Celebrating 125 Years of the Physical Review
https://journals.aps.org/125years #PhysRev125

We ask that you download the manuscript and return your report via:

https://referees.aps.org/r/XXXXXXX

Alternatively, you may send your completed Referee Response Form by email to prl@aps.org. If you use email, either reply to this message or give as the subject "Report STEPANENKO XXXXXXXXX".

...

Date: Tue, 8 May 2018 09:43:17 -0400
Message-ID: <1714919704.1525786997025.JavaMail.tomcat@prism-jobs-4-245>
From: prb@aps.org
Reply-To: prb@aps.org
To: dimitrije.stepanenko@ipb.ac.rs
Subject: Resub_review_request STEPANENKO XXXXXXXXXX

Dear Dr. Stepanenko,

We would appreciate your review of this manuscript, which has
been submitted to Physical Review B.

Comments from the editor:

    XXXXXXXXXXXXXX

Thank you for your help.

Yours sincerely,

Manolis Antonoyiannakis
Associate Editor
Physical Review B
Email: prb@aps.org
http://journals.aps.org/prb/

Celebrating 125 Years of the Physical Review
https://journals.aps.org/125years   #PhysRev125

We ask that you download the manuscript and return your report via:

https://referees.aps.org/r/XXXXXXXXX

Alternatively, you may send your completed Referee Response Form
by email to prb@aps.org. If you use email, either reply to this
message or give as the subject "Report STEPANENKO XXXXXXXX".

Komisija

Od školske 2015/2016. godine predsednik Državne komisije za takmičenja učenika srednjih škola iz fizike je docent dr Božidar Nikolić sa Fizičkog fakulteta u Beogradu.

Komisija za takmičenja učenika srednjih škola u školskoj 2017/2018. godini ima sledeći sastav:

Predsednik komisije:
Božidar Nikolić boza@ff.bg.ac.rs

1. razred:
Autor: Petar Mali
Autor: David Knežević
Recenzent: Milutin Stepić

2.razred:
Autor: Mihailo Čubrović
Autor: Aleksandar Bukva
Recenzent: Nikola Petrović

3.razred:
Autor: Vladan Pavlović
Autor: Ilija Ivanišević
Autor: Marko Kuzmanović
Recenzent: Dimitrije Stepanenko

4.razred:
Autor: Veljko Janković
Autor: Ana Hudomal

Autori eksperimentalnog zadatka za Srpsku fizičku olimpijadu:
Marko Opačić
Danko Bošnjaković
Milan Jocić